Facoltà di Ingegneria

Dipartimento di Scienza e Tecnica dell'Informazione e Comunicazione

Doctoral program in Information and Communications Technologies

Curriculum in Radar and Remote Sensing

Doctorate cycle XXIX

Observations of Titan Liquid Bodies
by means of the Cassini RADAR Altimeter

by

Valerio Poggiali

A thesis submitted for the degree of

Doctor of Philosophy

2016

Coordinator for the curriculum: **Ch.mo Prof. Pierfrancesco Lombardo**

Tutor – Supervisor: **Dr. Roberto Seu**

Try and leave this world a little better than you found it.

Robert Baden-Powell

To my family

Table of Contents

List of Figures

List of Tables

CHAPTER I

INTRODUCTION

Twenty years after its great departure from Cape Canaveral the Cassini mission is going to have the "Grand Finale" it deserves. This spacecraft definitely marked a milestone in astronautical history as one of the best examples of collaboration among different space agencies (NASA-ESA-ASI) and a great model for any other future mission for planetary exploration. A discovery machine that unveiled the Titan's lively world and that doesn't stop giving surprises at every new observation. I'm Valerio Poggiali, phD candidate, and with my colleagues and professors of La Sapienza University of Rome I'm involved in the Cassini RADAR altimeter data processing, a task bequeathed to us by our Prof. Emeritus Giovanni Picardi who started believing in this project already at the beginning of nineties when he published a paper entitled "The Radar System for the Exploration of Titan". It is 1992, and he states: "the knowledge of the ocean depth is particularly important and its determination is one of the main requirements for the radar instrument". Actually he announced twenty-two years in advance our work on "The Bathymetry of a Titan Sea" in which we reported about an incredible observation made by the Cassini radar altimeter on May 23st, 2013. We were waiting for that fly-by by years as it was representing the only opportunity to test the instrument capability to plumb the bottom of a Titan sea and infer about its dielectric properties (besides proving once for all the liquid nature of those dark features). After Kraken and before Punga, the Ligeia Mare is the second greatest sea of Titan (roughly 260 x 217 miles). We have been able to track a deepest point of 180 yards and estimate its liquid to be composed by an extremely pure mixture of liquid hydrocarbons (laboratory experiments at JPL eventually confirmed components to be methane, ethane and nitrogen). The following period has been very busy for us, but also extremely rewarding. After the publication of Ligeia Mare bathymetry, the Cassini radar altimeter observed the Kraken Mare on August 21st, 2014 and the Punga Mare on January 11st, 2015. The measurements we had to perform were very

10

challenging. Main difficulties came from the necessity to track the subsurface also in the shallowest parts of seas where we have to push the radar capabilities to the limits of its vertical resolution (nominally 33 yards but with some super-resolution algorithms improvable of a factor of about two). Another great test that we faced was in the production of the bathymetry of the largest lake (43 x 124 miles) of the southern polar area of Titan, the Ontario Lacus. The severe saturation of the receiver united to the shallowness of this liquid body (preliminary results suggested a 50 yards maximum depth along the altimeter ground track, that of course could be not the deepest point) imposed the necessity of developing a different method for determine its bathymetry and dielectric properties. Also if the Cassini radar will not observe Titan seas anymore (we will have just a last look to northern polar small lakes during Cassini's last flyby of Titan on April 2017) we have still many analyses to perform on the already collected data, these will engage us for years to come. The more Cassini mission will come closer to its end on September 15, 2017, the more we will have to stay tuned to not miss anyone of the discoveries that will certainly follow as the spacecraft will finally approach Saturn, receiving, as if it was an engagement gift, the unique opportunity of a closer observation of its precious rings.

In this PhD dissertation I would like to resume the main steps we followed for analyzing the Cassini radar altimeter data from which we obtained the first bathymetries of extraterrestrial liquid bodies, starting from a brief introduction to the RADAR instrument characteristics and its capabilities. Later I will focus on the backscattering models we adopted in order to effectively interpret the radar altimeter nadiral power returns from the surface of Titan.

A detailed description will follow of the simulator we developed in order to reconstruct as accurately as possible how the Cassini radar receiving chain processes on board the incoming signal. Then, I will describe the results we obtained on Ligeia Mare and Ontario Lacus, giving some anticipations on the work ongoing for Punga and Kraken Mare.

The last part will be finally dedicated to our discovery on Titan of liquid-filled canyons directly connected to seas. I will describe how the radar altimeter was able to measure their depth and infer about their nature of sea flooded valleys by means of a comparison of the levels of their liquids.

Far from being just a library-based theoretical dissertation, this document will intentionally focus on the work we carried out and on the consequent results we obtained in the framework of

the Cassini mission. The techniques described herein and, in particular, the simulator and the Bayesian method for the estimation of unknown parameters we adopted for this work are the result of the fruitful collaboration between our Dipartimento di Ingegneria Elettronica e Telecomunicazioni (DIET) of "La Sapienza" University of Rome and the Astronomy department of the Cornell University in Ithaca (NY).

CHAPTER II
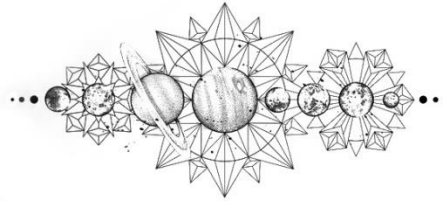
The Cassini RADAR: observations of Titan's liquid bodies with SAR and altimetry

The main science objective of the Cassini RADAR is to provide the most detailed information about the geomorphologic structure of Titan, allowing estimation of the composition of its surface/seafloors as well as the production of topographic and bathymetric maps. An introduction to the operation principles of the Cassini RADAR instrument and a more specific overview of the altimeter and SAR modes will follow.

a. The Cassini RADAR: scientific objectives and observation modes

The Cassini RADAR is a Ku-band (13.78 GHz) linear polarized radar instrument mounted aboard the Cassini orbiter. It can alternatively operate in several modes: as an altimeter it is able to generate topographic profiles, as a radiometer it can measure the emissivity, as a high resolution synthetic aperture radar (SAR) it can map the surface, as a scatterometer, finally, it is able to measure the real aperture backscatter reflectivity [IX].

The Cassini RADAR is composed of four big subsystems (see Figure 1): the Radio Frequency Electronics Subsystem (RFES), the Digital Subsystem (DSS), the Energy Storage Subsystem (ESS), the High Gain Antenna (HGA). While Alenia Spazio had the duty of integrating
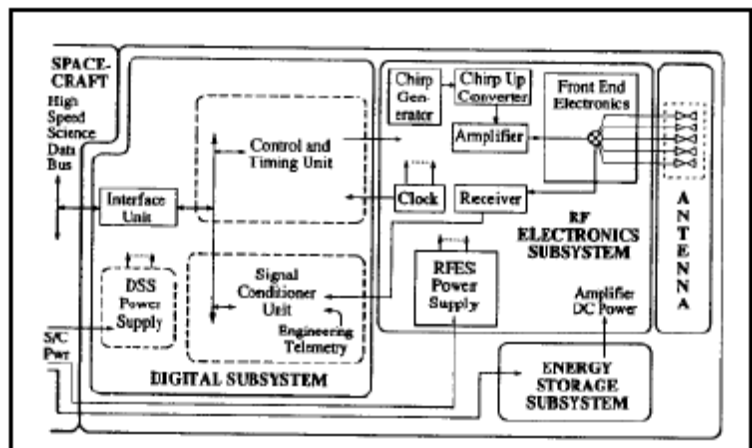
Figure 1: RADAR block diagram

Swath Name	Day (dd/mm/yyyy)	Number of Altimetry Bursts		
		Equatorial	North	South
Ta	26/10/2004	464	0	0
T3	15/02/2005	305	0	0
T8	28/10/2005	762	0	0
T13	30/04/2006	272	0	0
T16	21/07/2006	893	0	0
T19	9/10/2006	918	0	0
T20	25/10/2006	23	0	0
T21	12/12/2006	451	0	0
T23	13/01/2007	415	479	0
T25	22/02/2007	57	0	0
T28	10/4/2007	1248	5	0
T29	26/04/2007	986	0	0
T30	12/5/2007	3114	334	0
T36	2/10/2007	1839	0	0
T39	20/12/2007	644	0	0
T41	22/02/2008	408	0	0
T43	12/5/2008	600	0	0
T44	28/05/2008	661	0	0
T48	5/12/2008	133	0	0
T49	21/12/2008	448	0	468
T50	7/2/2009	211	0	196
T55	21/05/2009	240	0	400
T56	6/6/2009	198	0	100
T57	22/06/2009	442	0	124
T61	25/08/2009	137	0	0
T64	27/12/2009	589	0	0
T77	20/06/2011	1691	0	0
T83	21/05/2012	629	0	0
T84	6/6/2012	629	0	0
T86	26/09/2012	61	0	0
T91	23/05/2013	528	817	0
T92	10/7/2013	158	125	0
T95	14/10/2013	3	123	89
T98	2/2/2014	2084	0	155
T104	21/08/2014	125	912	0
T108	11/1/2015	127	335	0
T113	28/09/2015	204	0	0
T120	7/6/2016	130	0	160

Table 1. The altimetric dataset (TA-T120)

and testing RFES and HGA, the Jet Propulsion Laboratory (JPL) designed DSS and ESS.

The RFES is the radio frequency section of the Cassini radar. It allows to generate high power pulsed continuous wave or pulsed linearly frequency modulated signals programmable with different bandwidth, pulsewidth and center transmission frequencies. The RFES receives echoes and radiometer data, and performs the signal calibration as well.

The RFES is composed of seven subunits: the Digital Chirp Generator (DCG), the Chirp up Converter and Amplifier (CUCA), the Frequency Generator (FG), the RFES Power Supply (P/S), the High Power Amplifier (HPA), the Microwave Receiver (MR) and the Front-end Electronics (FEE).

The spacecraft main bus voltage (+30 V) is applied to the P/S, that regulates and distributes secondary voltage lines to the other RFES units. All the radar is coherently locked to a unique frequency source (10 MHz) which is generated by the FG and provide the signals needed by the three up and down conversions in TX and RX chains. The baseband signal is generated by the DCG which can be programmed to produce signals with pulsewidth up to 500 μs, bandwidth up to 5 MHz and center frequency up to 10 MHz. The CUCA translates the DCG baseband signal to the Ku-band. Its output works in a softly saturated region allowing an intrinsic amplitude flatness control and it is coupled to have an internal calibration signal. The HPA amplifies the signal in Ku-band through a TWT with a peak power of 183 W. An Electric power Conditioner (EPC) establishes the high voltage drawing

14

it from the ESS. The FEE is a circulator network able to route the TX signal from the HPA to the antenna through one of five waveguides and, conversely in RX, it routes the echo signal to the receiver path. The FEE is also able to provide an internal calibration path from the output of CUCA to receiver. Telemetry status signal allows FEE to drive HPA in TX mode avoiding damages to sensitive electronics of the receiver. An ambient temperature noise source has been placed in it to calibration purposes. The MR is the receiver and controls the echo signal power level with a dynamic range of 74 dB at 1 dB step. It can selectively filter up to four different signal bandwidths. The echo signals captured by the antenna and through a switching path are routed to a low noise amplifier. After some filtering and signal level control they are down converted to a baseband offset video frequency (2.5 MHZ) and finally passed to the digital section. The MR has a noise contribution less than 2.5 dB in noise figure (the noise figure of the whole receiving chain is 3.9 dB). The minimum output signal to be handle is -123 dBm. From the first part of the chain, it has been splitted a total power radiometer receiver which is able to receive low level signal (up to 200 K) with different integration periods (up to 90 ms). In the MR has been placed a hot noise calibration signal able to provide a reference signal both to radiometer and to altimeter/imaging path.

The DSS is the central control unit of the RADAR, making it possible to switch among the different operational modes. Thus its main duties are the reception and transmission of RADAR commands from and to the Command and Data Subsystem (CDS), it generates and controls the pulses transmitted by RADAR, it handles the transmission of scientific data to the CDS. The DSS is composed of five subunits: the Bus Interface Unit (BUI), the Flight Computer Unit (FCU), the Control and Timing Unit (CTU), the Signal Conditioner Unit (SCU) and the DSS power supply.

The ESS is responsible for the conversion from the + 30 V of the spacecraft main bus to the higher voltages requested by RADAR and handles the radio-frequencies filtering. As the Cassini spacecraft is electrically powered by radioactive thermal generators (RTG) that are not able to supply the peak transmitter power 195 W required by the RADAR during the 10 hours long flybys of Titan, the use of a battery was substituted by this bank of capacitors (the ESS), recharged between each transmitted burst, in a way that the final peak power requirement was reduced from 195 W to 30 W, with a power requirement of 86 W.

During its 13 years long Saturn tour, the Cassini spacecraft has not been orbiting around its principal target. Ever-changing orbital geometries produced several complications in the design of

RADAR, that has always been forced to operate exclusively during close flybys of Titan and with rapidly changing altitudes. In an optimal flyby sequence all the RADAR modes are activated in this order: radiometry only mode from 100,000 km to 22,500 km of altitude; scatterometry mode from 22,500 km to 9,000 km; nadir pointing altimetry mode from 9,000 km to 4,000 km; side looking imaging from 4,000 km to the closest approach. During the out-bound sequence the order of modes is normally reversed.

RADAR uses the spacecraft 4 m and five-beam HGA, that can operate in four different bands: the X/Ka for telecommunications, S for the radio occultation experiment and, as already mentioned, Ku for the RADAR.
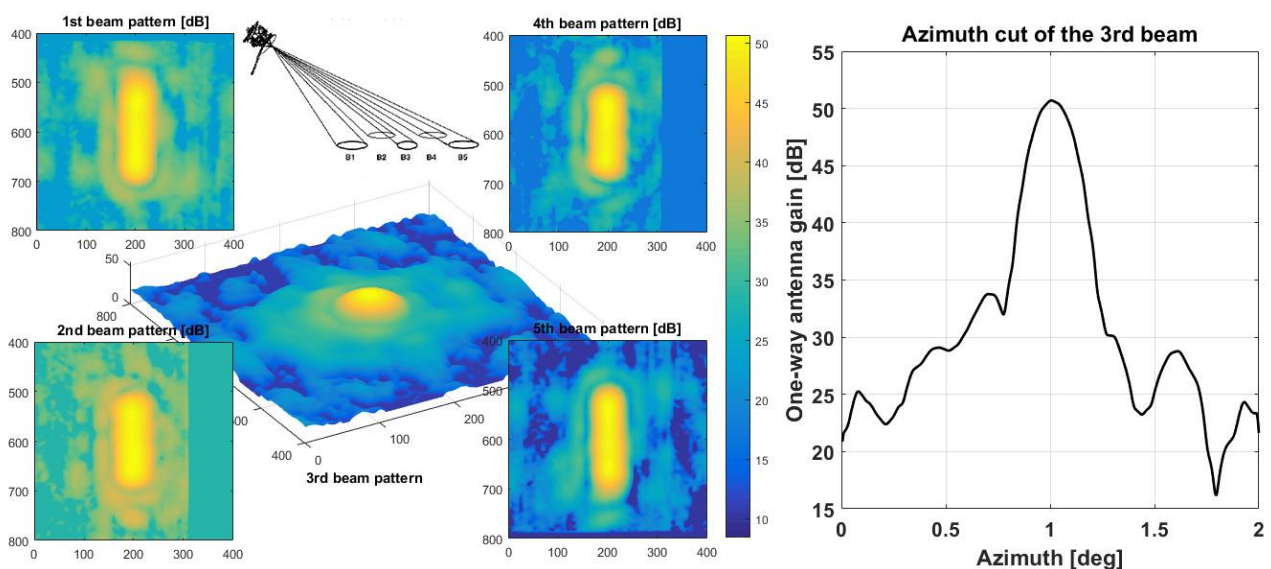
Figure 2. The Cassini antenna gain patterns

It is worth to note that while the highest–gain central beam is roughly circular (with a beamwidth of 0.35 degrees) and is used in all operative modes, the other four beams are activated only during the imaging mode, in a push broom scanner modality for maximizing coverage (see Figure 2 for actual beams patterns). Altimetry mode utilizes only the central nadir pointing antenna beam and, typically, altimeter tracks are not longer than few hundred kilometers.

By the end of the Cassini-Huygens mission SAR images will likely cover more than the 66% of Titan surface, while radiometer and scatterometer almost its totality. The altimetric tracks, although very sparse, have a relatively uniform distribution on the surface of Titan with a net prevalence of

±45° of latitude acquisitions (see Table 1 and Figure 3). Only the great interest of the scientific community in radar altimeter capabilities of plumbing the bottom of the seas has changed the volume of work for this instrument over the polar areas, especially from 2013 onwards.
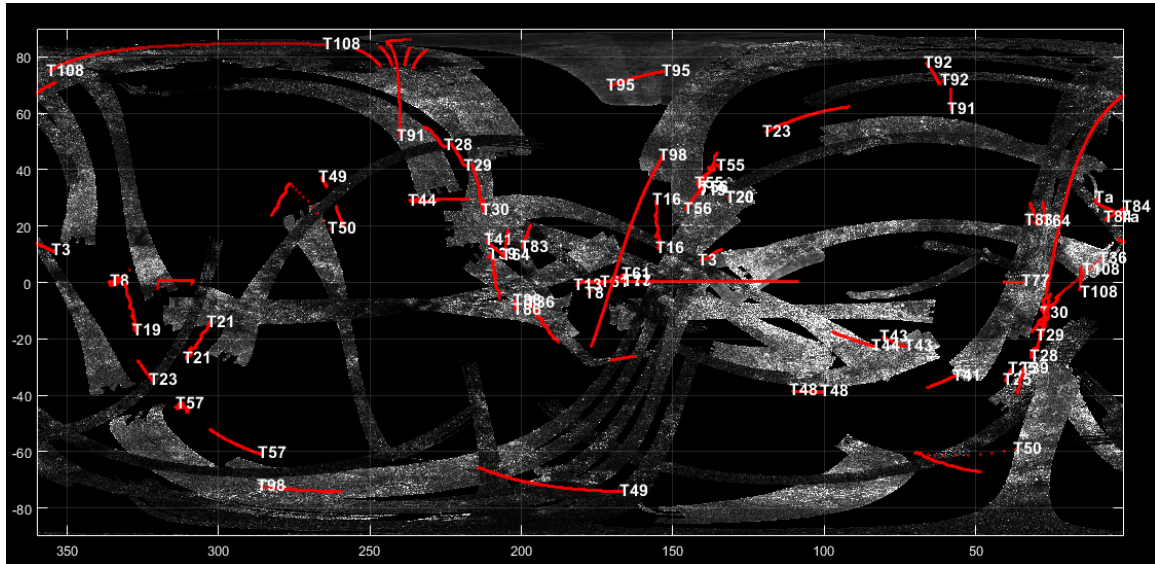
Figure 3. The altimetric dataset (TA-T108)

b. *Observations of Titan's liquid bodies in altimetric mode*

The Cassini altimeter operates in 'burst mode', this means that a train of pulses separated by 0.5-4 seconds are transmitted by the radar, that subsequently lies in wait mode to receive the return signals. Each burst is transmitted in 1.4-1.8 ms and is composed of a variable number (typically 21) of 150 μs long chirped pulses with a 4.25 MHz bandwidth. The resulting altimetry range resolution ("range bin") is of about 35 m.

Range compression and incoherent average of burst's pulses allow to obtain the main raw altimeter data product: an altimetric echo that averages the

Carrier Frequency	13.78 GHz
Carrier wavelength (λ)	2.17 cm
Burst period (T)	0.5-4 s
Chirped signal length	150 μs
Pulse repetion frequency (PRF)	4700-5000 Hz
Antenna 3dB beamwidth (θ_B)	0.35 deg
Chirped signal bandwidth (B)	4.25 MHz
Sample rate	10 MHz
Transmit time	1.4-1.8 ms
Peak transmitted power (PT)	48.084 W
Peak antenna gain (G_0)	50.7 dB
Titan mean radius (R_T)	2575 km
Vertical resolution (σ)	35 m

Table 2. Main parameters of the Cassini radar altimeter

17

topography over the 3-dB beam footprint area (ranging from 6 to 50 km depending on the spacecraft altitude). In order to give a correct estimation of the surface height relative to the center of mass of Titan it is necessary to have either the lowest possible absolute ephemeris error and uncertainty in pointing knowledge. As a matter of fact, the estimates of these two quantities are the major sources of error for the derived elevations that, however, result accurate at a 100-200m level [LII].

The Cassini RADAR Processing of Altimetric Data (PAD) is an ad hoc system developed by CO.RI.S.T.A. and DIET (ex INFOCOM) on behalf of the Italian Space Agency (ASI) to process and analyze the Cassini altimetry data. It is able to receive and process the Cassini RADAR Altimeter instrument raw data sets, to generate the corresponding science data products and to archive and manage them within the system.

By using optimized processing algorithms and tools expressly developed in a ©Matlab environment the Cassini RADAR PAD is able to manage the Long Burst Data Record (LBDR) altimeter data supplied by JPL to ASI and produced for every Titan flyby. The LBDR contains all the scientific data as well as the radar telemetry, timing and spacecraft geometry information.

Among the several logical components of the PAD we are mainly interested in understanding which ones are responsible for generating the altimetric profiles and how this work is done. First, the Altimeter Burst Data Record Production Tool (ABDR PT) deals with the creation of subsets of the input LBDR product, each one regarding one of the different Cassini RADAR active modes, and with the production of an intermediate burst ordered data product (BODP) file. The altimetric processing is carried out by the Science Look Tool (SLT), that automatically performs range compression of sampled data. The SLT evaluates altimeter profile range start, altimeter profile range step and altimeter profile length, since these data are subsequently required by the ABDR PT for the ABDR product creation.

In order to reduce the speckle noise, a single averaged pulse is created from each compressed burst [I].

During each fly-by, the Cassini radar altimeter operates in a particular range of spacecraft altitudes in which the dimension of the area of the beamwidth limited (BL) footprint and of the pulsewidth limited (PL) footprint are very similar [XXII]. In general BL mode validity starts when the spacecraft is going towards lower altitudes.

In PL mode the Cassini antenna beam is quite large respect to the high spacecraft altitude but the wide bandwidth adopted by the RADAR permits anyway to have a relative small spot on the ground.

In BL mode, on the other hand, the area illuminated by the antenna beam is smaller thanks to the lower altitude.

The scattering function $p_r(t)$ indicated in Figure 4 describes the overall response of a rough surface characterized by a gaussian probability density function of scatter points height. The larger is the spot on the surface the longer will be the rise time σ_p. After a peak value, $p_r(t)$ starts decreasing because of the limited dimension of the antenna beam and the related decreasing of the antenna gain [XXXVI].
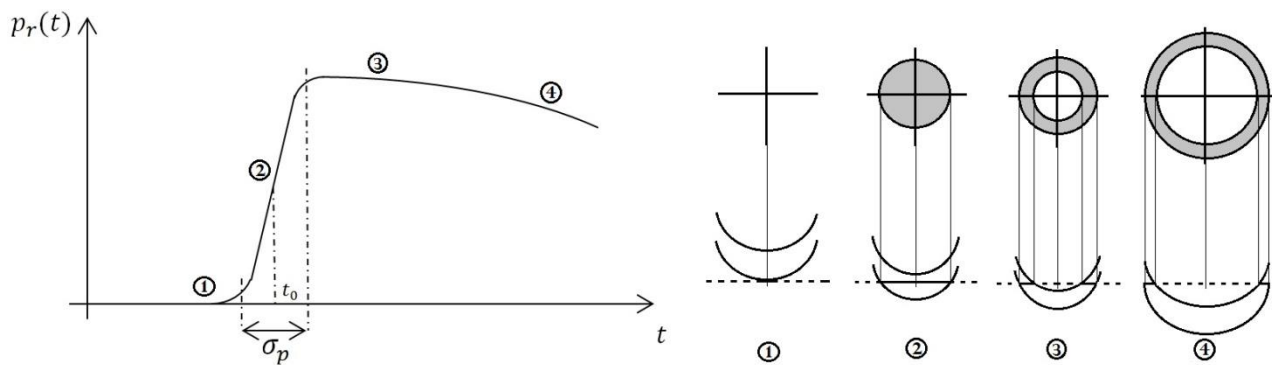
Figure 4: The scattering function trend and relative illuminated spot on the surface.

The amount of surface height variation and, above all, the Cassini antenna pointing error are the most important parameters affecting the echo's spread. Actually, the recorded mispointing values are rather small with respect to the 6.1 mrad of the Cassini antenna half power beam width (e.g., during the T30 fly-by the mean value has been of 0.6 mrad).

Despite a pointing accuracy of ~2 mrad and an absolute ephemeris error on the order of ~100 m, it is anyway possible to determine Titan's surface meter-scale roughness [LII]. The root mean square of the scatter points height (σ_h) is proportional to the standard deviation of the gaussian height probability density function. Thus, a scattering model can be described by a

statistical point of view allowing retrieval of the main altimetry parameters (mean delay from the surface t_0, reflectivity σ^0 and σ_h) by making use of estimation theory's laws.

At the time of Cassini RADAR design, many scientists were speculating that the surface of Titan could probably contain solid, liquid and muddy material creating features such as lakes, seas, or rivers. Because of this, the Cassini altimeter trackers have been chose for their ability to work both over ocean and land surfaces. As a consequence three different kinds of **height estimators** have been officially implemented in the Science Look Tool: threshold, I moment and Maximum Likelihood (ML).

The attainable height accuracy is strongly dependent on the Signal-to-Noise-Ratio (SNR) of the received echo and on the vertical roughness of the observed surface (σ_h), but it is also dependent on the choice of the height estimator. Thus, it is clear that for maximizing the performances of a radar altimeter the choice of an adequate estimation algorithm for the height retrieval is critical. This is not a trivial point, in fact we have to consider that every algorithm has different behaviors over different kinds of surfaces. Each algorithm is able to extract different information from the same observed surface and only the comparative analysis of an appropriate set of them could compose the most complete description of the observed surface.
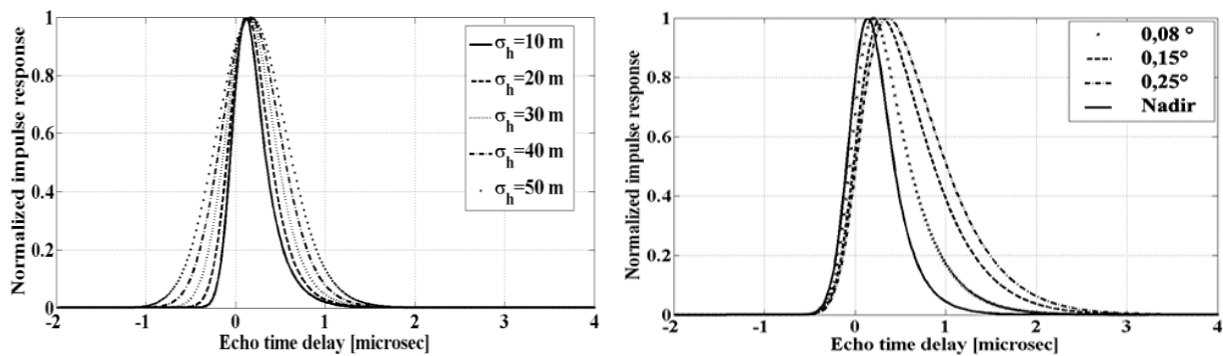
Figure 5: (left) Averaged and normalized nadir (Θ = 0°) impulse response evaluated at different values of surface roughness σ_h and at H = 5000 km of S/C altitude. (right) Averaged and normalized near-nadir impulse response of a rough surface evaluated at σ_h = 20m , altitude H = 5000 km, with different values of incidence angle Θ.

In Figure 5 some examples of received echoes from rough surfaces and with increasing incidence angle are shown. Note how the echo spreads varying the observation scenario.

The threshold estimator detects the return delay of the surface echo from the transmission event by finding the earliest time at which the intensity of the received echo exceeds the level of the received peak power divided by a suitable value adapted to the actual level of noise.

The estimation error $E(\theta)$ committed by this estimator increases dramatically as the off-nadir angle θ increases, with a low dependence on the surface RMS slope m. Figure 6 indicates estimation error varying the rising edge slope. For values of θ about half of the antenna beamwidth, the magnitude of the rising edge slope is four time lower compared to that of the nadir pointing case.
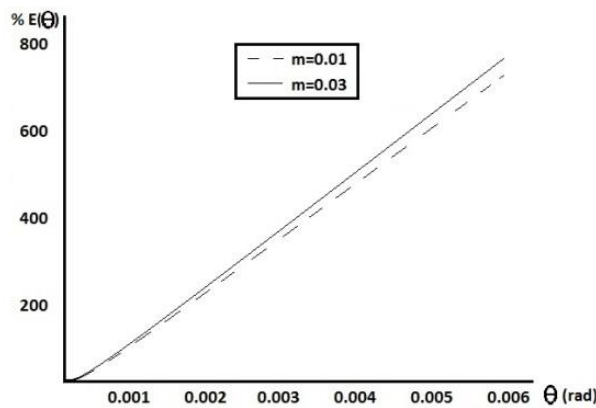
Figure 6: rising edge estimation error for a nadir pointing altimeter in the case of a threshold tracker.

The centroid tracker is a leading edge estimator based on the Offset Centre of Gravity (OCOG) algorithm developed by Wigham in 1986 [L]. This estimator first computes the centroid of the whole observed power distribution, as described by the first moment of the echo with respect to time (that is what is barely done by a simple Centre of Gravity (COG) algorithm). Then, it tracks the position of the waveform leading edge by subtracting the estimated half duration of the signal itself from the previous result. For improving the performance at low signal to noise ratios, the output of the filters is first squared before carrying out the calculation, in this way the OCOG algorithm exhibits wider dynamic range at high signal to noise ratios and good performance with many different models [III, IV].

The estimation of the time delay required by the signal to complete the two-way travel from a mean surface is characterized by an error function $E(\theta)$ increasing exponentially as the off-nadir angle θ increases, once again with a low dependence on the rms slope m (Figure 7). It is simple to

21

note how the error values for the centroid tracker are few orders of magnitude lower respect to the threshold estimator.
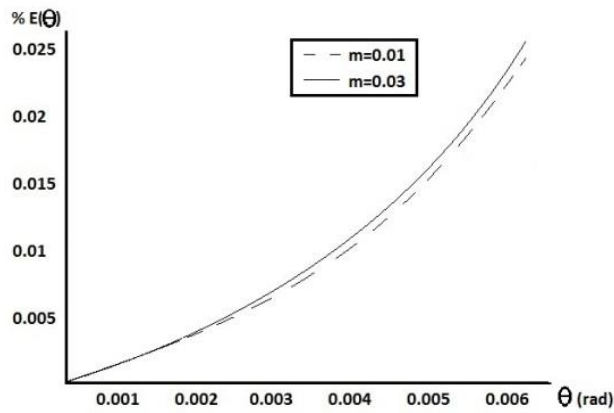
Figure 7: time delay estimation error with respect to the case of a nadir pointing altimeter for a centroid tracker.

It is important to consider that, while the centroid estimator is able to give information about the mean level of the area illuminated by the footprint, the threshold is characterized by an higher sensibility for the most elevated points inside the observed area.

The minimum root mean square on the distance measurement (precision) for the threshold and the centroid estimators on single pulse in the case of flat surface is given by:

$$\Delta r = \frac{c}{2} \cdot \frac{1}{\beta \sqrt{2 \cdot \text{SNR}}}$$

where c is the speed of light, SNR is the maximum signal to noise ratio, β is the signal bandwidth (see Figure 8) [XXXVI].
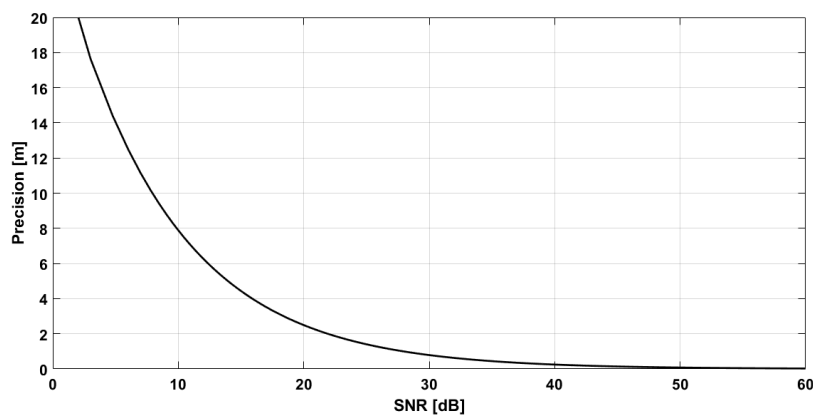
Figure 8: precision on distance measurement for threshold and centroid estimators

If a surface roughness is considered as well, we can include the RMS height σ_h in the last formula by substituting the bandwidth β with

$$\beta_r = \frac{1}{\sqrt{\dfrac{12}{\beta^2} + \left(\dfrac{2\sigma_h}{c}\right)^2}}$$

In Figure 9 it is shown an example of application of this formula.
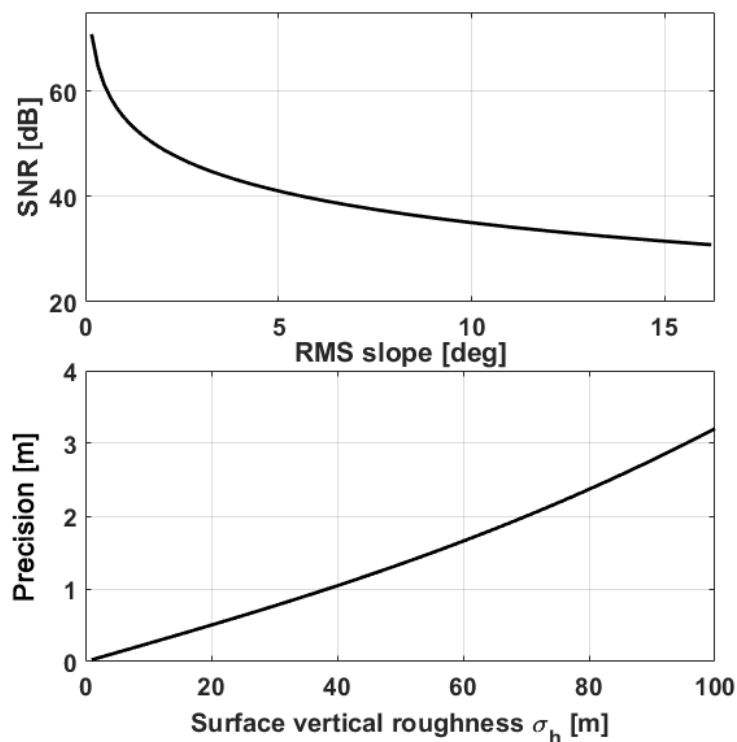
Figure 9: During the flyby T108 Cassini acquired an altimetric observation of the Fensal dunes field from an altitude of 6919.8 km and with a recorded SNR of about 33 dB. (upper panel) Signal to noise ratio obtained from the radar equation varying the RMS slope with a 500 m constant correlation length and (lower panel) precision on distance measurement varying the vertical RMS height of the observed surface.

The Maximum Likelihood Estimator (MLE) is based on iteratively fitting the averaged received echo with the reported theoretical model $p_r(t)$ by means of a progressive minimization of fitting error. The height retrieval is performed on real radar data, thus affected by thermal noise and speckle, but, differently from other unbiased estimators, the MLE is asymptotically efficient and, for a number of iterations that tends to infinity, it achieves the Cramer-Rao bound (this bound

23

provides the minimum variance of any unbiased estimator of a parameter of interest). When the error becomes lower than a fraction of the Cassini signal sampling interval the final height value is reached. According to a threshold criteria related to the current value of the off-nadir angle, the best altimetry non-coherent echo model to be used during the processing is automatically selected.

Simulations conducted by Alberti et al. [II] have given the actual performance of this estimator, at off-nadir angles ranging from 0 to 0.35 deg and spacecraft altitudes from 4000 to 9000 km, indicating surface height estimation errors with mean values between ±6 m and standard deviation (std) values of about 5 m for the nadir model and of about 15 m at higher off-nadir angles.

I conducted myself a campaign of simulations by setting the antenna pointing angle at nadir, the spacecraft altitude at 4000 km and a mean SNR of 33 dB (typical value for a number of Cassini radar flybys over solid surfaces). The results in terms of means surface height estimated and precisions are resumed in the following Table 3 where a comparison among different tracker has been performed. The Maximum Likelihood Estimator resulted to be the most accurate for the whole set of simulated roughness. The Threshold estimator resulted to be the most precise for the whole set of simulated roughness.

sigmah [m]	10	20	30	40
ML mean [m]	9,01	12,58	11,65	21,28
ML std [m]	47,74	53,97	59,76	68,04
I MOM mean [m]	70,33	72,56	70,30	77,01
I MOM std [m]	45,16	50,12	58,04	67,51
TRESH mean [m]	-62,71	-83,80	-108,97	-137,88
TRESH std [m]	19,95	27,31	36,43	46,64
EL mean [m]	55,00	55,81	52,50	54,46
EL std [m]	33,50	37,58	44,40	51,40
OCOG mean [m]	-210,62	-233,34	-266,55	-297,76
OCOG std [m]	45,04	53,63	60,95	68,21
SNR mean [dB]	33,96	33,64	33,42	33,15
SNR std [dB]	3,16	3,07	2,63	2,58

Table 3: trackers performances for the Cassini radar altimeter simulated echoes. The I moment tracker is based on the same principle of the OCOG tracker but it is able to adapt to the actual level of noise. I implemented trackers and simulated the reflection of the Cassini burst from more than 4000 different synthetic surfaces with varying sigma_h (sampled at 10 m). All the variance estimations are have been obtained with a precision <2.3%.

For the estimation of Titan surface **backscattering coefficient σ^0** in the case of a beam-limited radar altimeter, we need to take into account two main different observation cases: liquid bodies and solid surfaces. We will suppose, in general, a Gaussian model for the probability density function of the surface height, with a spatial correlation length $l_x = l_y = 1$ and a surface RMS slope $m = \sqrt{2}\sigma_h/l$ (Gaussian correlation function).

Coherent backscattering: if we consider a smooth spherical surface A (with $2\pi R_{sphere}/\lambda \gg 1$), illuminated by a flat impinging wave coming from nadiral direction, the backscattering is $\sigma = A\Gamma(0)$ [m^2], with $\Gamma(0)$ is the Fresnel reflectivity at normal incidence (see below). For Titan we would have

$$\sigma = \pi R_{Tit}{}^2 \Gamma(0) \quad [m^2]$$

However, in this case, the greatest backscatter contribution is the coherent one coming from a much smaller area (Fresnel zone) opposite to the radar, whose radius is $r_F = \sqrt{R_{Tit}\lambda/2}$ [m]. So, in this case it is possibile also to approximate the area πR_{Tit}^2 to a disc of radius $R_F = \sqrt{\lambda H/2}$ [m] and obtain

$$\sigma = \Gamma(0) * \pi R_F^2 = \Gamma(0) * \pi \frac{\lambda H}{2} \quad [m^2]$$

Take care that if we have, instead, the dual case of a spherical wave impinging a flat surface we have just to substitute R_{Tit} with the spacecraft altitude H; otherwise, if we have both wave and surface spherical, R_{Tit} has to be substituted by $H_C = (R_{Tit} * H)/(R_{Tit} + H)$.

At small incidence angles, when roughness is negligible and Kirchoff approximation is applicable (correlation length and curvature radius in each point of the surface larger than the incident wavelength), it is necessary to consider the Physical Optics (PO) model, that describes the coherent component of the backscattering. This is the case of the extreme flat Titan liquid bodies surfaces, where the coherent component clearly prevails on the non-coerent, typical of the

returns received from Titan solid surfaces and very well described by the Geometrical Optics (GO) model.

But what happens if we want to take into account the small scale vertical roughness σ_h of the observed Titan liquid bodies surface? Always considering a flat wavefront impinging on a spherical surface of radius R_{Tit}, the radar-cross section become:

$$\sigma = \Gamma(0) * \pi R_{Tit}^2 * e^{-4k\sigma_h^2} \quad [m^2]$$

with $k = 2\pi/\lambda$.

For a spherical wave impinging a spherical surface we have to substitute R_{Tit} with H_c:

$$\sigma = \Gamma(0) * \pi H_C^2 * e^{-4k\sigma_h^2} = \Gamma(0) * \pi H_C^2 * e^{-4(2\pi/\lambda)\sigma_h^2} \quad [m^2]$$

At this point, in order to obtain the σ^0 adimensional value we need simply to normalize σ by the area πH_C^2, so that we will obtain

$$\sigma^0 = \Gamma(0) * e^{-4k\sigma_h^2} \quad [adim]$$

In order to infer about dielectric and geometric properties of the observed surface from real Cassini RADAR altimeter data, let's see now how to obtain the value of σ^0 by inverting the radar equation:

$$K = \frac{P_t}{4\pi H_C{}^2} G_t \sigma \frac{A_r}{4\pi H_C{}^2} * B * T \quad [W]$$

with $A_r = \frac{G_r}{4\pi}\lambda^2$ and with $B * T$ the compression gain.

After few simple calculations we have

$$K = \frac{P_t G^2 \lambda^2 B\, T}{(4\pi)^3 H_C{}^4} \Gamma\, \pi\, H_C^2\, e^{-4k^2\sigma_h^2} = \frac{P_t G^2 \lambda^2 B\, T}{64\,\pi^2 H_C{}^2} \Gamma\, e^{-4k^2\sigma_h^2} = \frac{P_t G^2 \lambda^2 B\, T}{64\,\pi^2 H_C{}^2} \sigma^0 \quad [W]$$

Now let's consider the actual signal power (P_{RX}) received by the Cassini RADAR altimeter during an observation of Titan. We have to subtract the noise (P_N) and introduce the calibration constant (C) together with the attenuator level adopted for the selected fly-by ($at3_{tot}$), so that we can write the formula:

$$P_{RX} = \frac{2 * (P_S - P_N) * C}{at3_{tot}} \quad [W]$$

If we match P_{RX} with the expression of K we finally obtain the value of the backscattering coefficient σ^0:

$$P_{RX} = K$$

$$\Rightarrow\ \sigma^0 = \frac{2 * (P_S - P_N) * C * 64\,\pi^2 H_C{}^2}{at3_{tot} * P_t G^2 \lambda^2 B\, T} \left(= \Gamma(0)\ * e^{-4k^2\sigma_h^2}\right) \quad [adim]$$

from which with a simple inversion we can infer possible values of dielectric and geometric properties of the observed surface, such as the dielectric costant ε_r or the surface small scale roughness σ_h, in fact we have to remember that

$$\Gamma(0) = \left|\frac{\sqrt{\varepsilon_{r1}} - \sqrt{\varepsilon_{r2}}}{\sqrt{\varepsilon_{r1}} + \sqrt{\varepsilon_{r2}}}\right|^2 \xrightarrow{\varepsilon_{r1}=1\ (air)} \left|\frac{1 - \sqrt{\varepsilon_{r2}}}{1 + \sqrt{\varepsilon_{r2}}}\right|^2 \quad [adim]$$

Note that the formula obtained for σ^0 is valid for single echo, if more echoes are averaged the result needs simply to be divided by the number of pulses composing the received burst.

Non-coherent backscattering: for what concerns the non-coherent component of the backscattering (dominating when surface roughness is not negligible with respect to the incident wavelength, i.e. the greatest part of Titan's solid surfaces) two different echo models [XXXII, II] varying the off-nadir angle (ξ) have been developed for the Cassini RADAR altimeter:

$$\begin{cases} p_r(t) = \sqrt{\dfrac{\pi}{2}}A\sigma^0 \exp\left[\dfrac{\delta^2}{2} - \dfrac{\delta t}{\sigma_{eq}}\right]\left[1 + \mathrm{Erf}\left(\dfrac{t}{\sqrt{2}\sigma_{eq}} - \dfrac{\delta}{\sqrt{2}}\right)\right] & \xi < 0.04 \text{ deg} \\[4mm] p_r(t) = \sqrt{\dfrac{\pi}{2}}A\sigma^0 \exp\left[-\dfrac{4}{\gamma}\sin^2\xi\right]\cdot\sum_{i=1}^{N} C_i \exp\left[\dfrac{\delta_i^{\;2}}{2} - \dfrac{\delta_i t}{\sigma_{eq}}\right]\left[1 + \mathrm{Erf}\left(\dfrac{t}{\sqrt{2}\sigma_{eq}} - \dfrac{\delta_i}{\sqrt{2}}\right)\right] & 0.04 \leq \xi < 0.29 \text{ deg} \end{cases}$$

where the different parameters are defined in the appendix of this chapter at Page 35.

However, while electromagnetic model used to describe surface parameters is independent on the altimeter operative mode, it is strongly dependent on the scattering mechanism (mainly non-coherent as we said, because of the short Cassini wavelength). In this context the normalized cross-section is:

$$\sigma^0(\xi) = \frac{\Gamma(0)e^{-(tan^2\xi/2m^2)}}{2m^2cos^4\xi}$$

always remembering that $\Gamma(0)$ is the Fresnel reflectivity at normal incidence and $m = \sqrt{2}\sigma_h/l$.

As previously anticipated the Cassini RADAR PAD performs an iterative best fitting of the echo model reported above varying the mean delay from the surface t_0, the reflectivity σ^0 and the large scale surface roughness σ_h. In particular the processor adopts this formula:

$$K = \frac{P_t G^2 \lambda^2 \, c \, \pi \, \sigma_p \sigma^0}{2 \, (4\pi)^2 H_C^{\;3}} B \, T \quad [W]$$

with $\sigma_p = \frac{1}{2B\sqrt{2\ln 2}}$

that, after few simple calculations, becomes

$$K = \frac{P_t G^2 \lambda^2 \, c \, T \sigma^0}{64\pi \, \sqrt{2\ln 2} \, H_C{}^3} \quad [W]$$

Matching K with

$$P_{RX} = \frac{2 * amp_{ML} * C}{at3_{tot}} \quad [W]$$

where amp_{ML} is the amplitude of the echo model fitted over the real received echo.

Finally, we obtain the value of the backscattering coefficient σ^0:

$$P_{RX} = K$$

$$\Rightarrow \quad \sigma^0 = \frac{2 \, amp_{ML} * C}{at3_{tot} * K} = \frac{2 \, amp_{ML} * C * P_t G^2 \lambda^2 \, c \, T}{at3_{tot} * 64\pi \, \sqrt{2\ln 2} \, H_C{}^3} \left(= \frac{\Gamma(0) e^{-(tan^2\xi / 2m^2)}}{2m^2 cos^4\xi} \right) \quad [adim]$$

For what concerns the **altimetric observations of Titan liquid bodies**, they are relative to a small number of bursts respect to the big dataset acquired, that is composed by more than 23000 (up to T113) bursts. First RADAR altimetry observation of a liquid body occurred only on April 26, 2007. During the **flyby T49** of Titan. In that occasion, Cassini acquired altimetry across the Ontario Lacus, a 220 km by 60 km lake located in the southern polar area, providing evidence of its liquid nature and information about the slopes driving drainage into the lake. Due to the unexpected strong specular reflections received from the flat surface of this liquid body, the acquired altimetric bursts resulted saturated.

For the next observation of a liquid body, we had to wait until May 23, 2013, when in occasion of the **flyby T91** the Cassini RADAR pointed its antenna at nadir, acquiring one of the most important altimetric track of the whole mission along ~300 km of the Ligeia Mare liquid surface.

Since the greatest part of the northern polar area of Titan was already mapped by the Cassini RADAR imager and following the outstanding results of the T91 observation, during which part of the signal bounced on the hundred meters deep seafloor and was received back by the radar, a longer observational time was granted to the altimetry mode. This coincided with a great number of flybys overflying the three great seas and the small lakes of Titan with the radar altimeter turned surprisingly into a real radar sounder.

Figure 10: the Huygens Landing Site

During **flyby T92** the altimeter received once again specular reflections from two small unnamed lakes. We have just one footprint (burstID# 250032590) on the first and four (burstID# 250032609/612) on the second. During **flyby T95** the altimeter received five more echoes from another small unnamed lake (burstID# 253033411/415).

The following altimetric observation, performed during the **flyby T98,** is one of a kind in the Cassini mission since the altimetric track covered a couple of surfaces located in the equatorial area, that resulted compatible with the presence of liquids (the famous putative "tropical lakes"). This acquisition has to be combined with the observation made by the Visual Infrared Mapping Spectrometer (VIMS) of long-lasting low albedo localities in the same area [X]. Clear evidences of the presence of liquids shaping the landscapes of Titan have been undoubtedly found on January 14, 2005 by the European Space Agency's Huygens probe during its successful descent and landing in the western part of the Shangri-La equatorial region on Titan. Here Huygens observed a network of pluvial/fluvial channels connected to a large alluvial plain (see Figure 10) in which it finally landed, finding pebble-sized ice blocks, whose shape was clearly the result of erosion from fluvial activity. The limited resolution of the Synthetic Aperture Radar of Cassini (ranging from 350 m to over 1 km) could never confirm these evidences indicating the presence of liquids in the equatorial area of Titan. Another interesting observation that would eventually confirm the presence of liquids in the equatorial areas are the specular reflections that have been detected

30

using the Arecibo Observatory's (AO) 13 cm wavelength radar system. Smooth surfaces characterized by few degrees RMS slopes are indicated, by the fitting of echo spectra with scattering models, as the responsible for generating such strong radar returns [XVII].

Part of the **flyby T104** was devoted to the altimetric acquisition of reflections from Kraken Mare across three different sections of the sea (from burstID# 261039615 to 261039685, from 261039763 to 261039999 and from 261040081 to 261040183). Unfortunately, the extraordinarily strong reflections from the perfectly flat surface of the sea caused signal saturation in the western and in the first half of the central section of the sea. To this flyby pertains also the small Cayuga lacus observation (burstID# 261041627).

To the third biggest sea of Titan, Punga Mare, was dedicated part of **flyby T108** altimetric data take, which includes as well echoes received from a number of small lakes. The first unnamed one is observed at burstID# 265025251. Then we have a second unnamed and bigger lake at burstID# 265025275. The wide connection between Kraken Mare and Punga Mare was covered by burstID# from 26502529, 26502531 and from 265025311 to 265025341. We have a third unnamed lake from burstID# 265025357 to 265025361 and, finally, the bursts related to the Punga Mare observation from 265025397 to 265025461.

Finally, some other small lakes, located in the north polar area, will be eventually covered on April 22, 2017 during the last flyby of Titan, namely the **flyby T126** (see Figure 11 for the map of the Northern polar area of Titan).

c. Observations of Titan's liquid bodies in SAR mode

The RADAR side looking imaging mode provides variable resolution synthetic aperture (SAR) images of Titan's surface used to describe its complex morphology. SAR resolution varies from 350 m at closest approach to over 1 km at the maximum nominal altitude of the SAR mode, with higher resolution in the center of the SAR strips and lower at the ends. Combining all the five beams it's possible to obtain strips 120 km wide and about 5000 km long, at fly-bys with 1000 km of closest approach altitude, see Figure 12 for an example. SAR images brightness represents normalized microwave energy backscattered from the surface, which is a function of surface slope, dielectric properties and roughness.

Figure 11: Titan's North Polar lakes and seas as revealed by the Titan RADAR mapper. Credits: R. Kirk

Due to the presence of the speckle noise, SAR images appear, furthermore, somehow grainy.

It should be clear from the above how the Cassini RADAR images could differ from what the surface appears to the eyes and how much care should be taken during SAR images interpretation. Created for helping scientists in this task, the PAD Map Tool (MT) is a graphical application that allows users to display Titan 2D and 3D maps. This tool has been designed for the analysis of maps informative content and as instrument of interpretation of scientific data. The content of Basic Image Data Records (BIDR) is extracted by means of a Data Production Utility (developed by CO.RI.S.T.A. for ASI), that saves all relevant information needed to produce MT datasets (map files) containing SAR data. The BIDR data files, produced at Jet Propulsion Laboratory (JPL) by the Cassini

32

RADAR Science Team (CRST), are single-pass, calibrated and gridded SAR image data that are archived in the imaging node of the NASA's Planetary Data System (http://pds-imaging.jpl.nasa.gov/) in more than one word type (e. g. byte vs. floating point) and resolution [XLIV]. The BIDRs are produced in an oblique cylindrical coordinate system and organized in different files containing different steps in the processing of the backscatter images. The primary images are the BIF files that contain floating point normalized radar cross section (NRCS) data from which systematic biases due to thermal and quantization noise, as well as systematic variations due to incidence angle have been removed. Moreover, the USGS Flagstaff Astrogeology Team is responsible for converting BIF files to 8-bit format log-scale images at various resolution; these latter are called BIB files and are archived by the JPL together with the full-resolution floating-point images [XXXII].

The first observation of lakes date back to 22 July 2006 in occasion of the **flyby T16** when SAR swath covered part of the Northern Lakes Region and, among many others unnamed lakes, imaged Bolsena Lacus, Koitere Lacus, Neagh Lacus and Mackay Lacus. Later, the **Flyby T18**'s swath imaged some more lakes in this same region including the famous "kissing lakes", namely the Abaya Lacus, and the Feia Lacus.

On October 9, 2006 during the **flyby T19** the RADAR swath covered part of the big Jingpo Lacus, a small part of Punga Mare, Sparrow Lacus, Waikare Lacus, Myvatn Lacus, Oneida Lacus.

Parts of Jingpo Lacus, Kraken Mare and the whole Ligeia Mare are included in the **flyby T25** SAR image acquired on February 22, 2007 together with a targeted distant look taken on the Northern Lake District where a number of lakes are shown, among them we remember the Kivu Lacus and the Müggel Lacus.

During **flyby T28** the Cassini RADAR mapper acquired one of the most suggestive SAR swaths (Figure 12). Starting from the Fensal dunes fields in the equatorial area of Titan the radar moved up to the North covering parts of Jingpo Lacus, Kraken Mare, Ligeia Mare, Towada Lacus, Uvs Lacus, Atitlan Lacus, Cayuga Lacus, Sevan
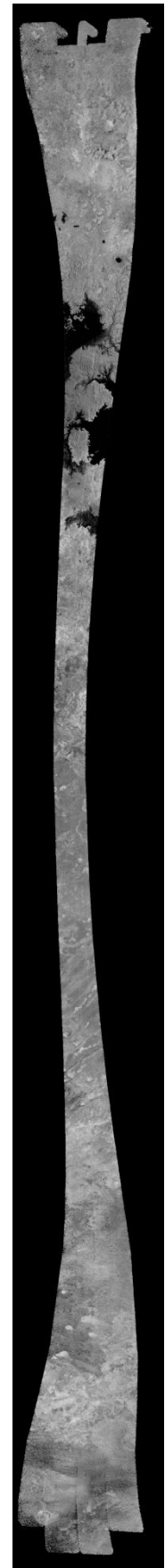
Figure 12: flyby T28 SAR swath. North is up.

33

Lacus, Logtak Lacus, Albano Lacus, Junin Lacus and a part of Vänern Lacus. This SAR image includes also the whole course of Vid Flumina, a drainage network of liquid-filled canyons on which I will report in the last part of this dissertation.

Bolsena Lacus, Punga Mare, Ligeia Mare, the whole Vänern Lacus, Lanao Lacus, Ohrid Lacus, Cayuga Lacus, Sevan Lacus, Logtak Lacus have been imaged on April 26, 2007 during **flyby T29**.

On May 12, 2007 during **flyby T30** the Cassini SAR imaged part of the central Kraken Mare next to the throat of Kraken (the strait between North and South Kraken Mare).

While an Hi-SAR (low resolution SAR) was acquired just over a small lake near the Ontario Lacus during **flyby T55** on May 21, 2009, we had on June 22 and July 8 (**Flyby T57 and T58** respectively) a partial coverage of the Ontario Lacus.

The **flyby T64** SAR data acquired on Dec 29, 2009 contain many gaps because of a downlink issue to the antenna complex in Madrid, Spain, but it covers part of the Punga and Ligeia Mare as well as Vänern Lacus, Sevan Lacus, Ohrid Lacus and Logtak Lacus.

The **flyby T65** imaged the whole Ontario Lacus and the small lake next to it (see flyby T55) in SAR mode and part of the Ontario Lacus in HiSAR.

The North Polar lake district was once again imaged during the **flyby T83** (May 22, 2012) acquiring SAR data of a number of small lakes and on part of the Abaya Lacus (or "kissing lakes").

An Hi-SAR swath acquired part of the Western Kraken Mare on **flyby T84** and was followed by the **flyby T86** observation that offered a different of Jingo Lacus, Kraken and Ligeia Mare, Cayuga Lacus and the Vid Flumina channels network.

During the **flyby T91** was acquired a very interesting segment, the fourth, where a number of small named and unnamed lakes appears. The named ones are Waikare Lacus, Myvatn Lacus, Mackay Lacus and part of Oneida Lacus. In this swath are present two intermittent lakes: the Woytchugga Lacuna, that with its 449 km in length it is the longest lake on Titan, and the Nakuru Lacuna, probably the sixth largest body of liquid on Titan.

Flyby T92 swath covered the same lakes an lacunae of flyby T91. Along with these a part of Ligeia Mare is imaged, together with Uvs Lacus and Towada Lacus. An image of Vid Flumina is acquired as well. The second segment of this radar acquisition covers Neagh Lacus, almost the whole Punga

Mare and the Kraken Mare's Moray Sinus with the labyrinth of channels connecting Ligeia and Kraken Mare (Okahu Sinus and Trevize Fretum).

Uvs Lacus, Atitlan and southern Ligeia Mare were observed in the second segment of **flyby T95**, while the third segment imaged Ontario Lacus and one unnamed lake nearby.

The first and fourth segments of the SAR swath acquired on **flyby T98** includes of the whole Ontario and the two small unnamed lakes close by.

Segment 5 of **flyby T104** SAR image mapped Freeman Lacus and Ligeia Mare. Right after this acquisition (segment 7) the first beam of the antenna was pointed to the central portion of Kraken Mare for taking images of the area of Penglai and Bimini insulae while the third beam was acquiring its altimetric track of Kraken Mare over Kraken Mare.

On **flyby T108** the RADAR mapper observed part of Ligeia Mare, as well as Ohrid Lacus, Logtak Lacus, Vänern Lacus and the Eyre Lacuna, Melrhir Lacuna and Ngami Lacuna.

Flyby T121 was devoted to the acquisition of images of the equatorial area, comprising the zone for which putative lakes had been revealed by VIMS and the radar altimeter. While the image interpretation for this recent acquisition is still ongoing, what it is already clear is that big liquid bodies are not present in this dunal area and that if lakes have been present they are intermittent.

The last SAR acquisition, the **flyby T126,** will take place on April 22, 2017 and will eventually map part of the northern polar area.

d. Chapter two appendix

Recalling equation at Page 28, σ is the transmitted pulselenght and B is the chirp bandwidth; A and A_{eq} are respectively the area of the pulsewidth and beamwidth limited circle;

$$\delta = r_A \sqrt{1 + 2F} \text{ with } r_A = A/A_{eq};$$

$$F = \left(\frac{2\sigma_h}{c}\right)^2 \Big/ 2\,\sigma^2;$$

$$\sigma_{eq} = \sqrt{\left(\frac{1}{B\sqrt{8\ln 2}}\right)^2 + \left(\frac{2\sigma_h}{c}\right)^2}.$$

For the other parameters definition and more details about the echo model adopted for $\xi \geq 0.04$, that is the result of an exponential approximation of an integral equation (that cannot be solved in a closed form) please refer to Alberti et al., 2009 [II].

<div align="center">

CHAPTER III

</div>

<div align="center">
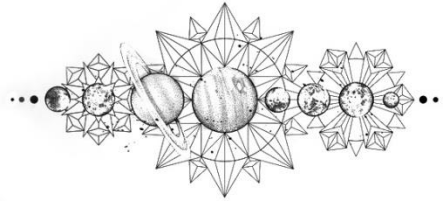
SIMULATION OF CASSINI ALTIMETRY WAVEFORMS FROM LIQUID BODIES ON TITAN

</div>

R adar sounding a is technique which allows the exploration of planetary interiors up to several kilometers under the surface. As the Cassini RADAR altimeter has recently turned into a radar sounder capable to probe the seafloor of Titan seas, we need to investigate the penetration capability into liquid hydrocarbons media by the Cassini RADAR electro-magnetic waves. This ability depends in general on the wavelength adopted by the radar sounder: longer wavelengths guarantee deeper penetrations.

Radar sounding is a useful technique in planetary exploration for characterizing subsurface geological structures and dielectric properties. As a sounder the Cassini RADAR can be used to probe the depth and constrain the composition of hydrocarbon seas on the Saturn's moon Titan. Altimetry waveforms received during observations of seas and lakes are frequently composed of two main reflections: the one generated at the surface of the liquid and the one coming from the seabed. The time interval between these two peaks is a measure of depth, and the attenuation from the propagation through the liquid is a measure of the effective dielectric properties (loss tangent), which is a sensitive measure of liquid composition. Such attenuation can be estimated by adopting inversion techniques which use the amplitudes and times of the two reflections along with an appropriate model. However, radar measurements are affected by uncertainness that include thermal and speckle noise, processing artifacts and receiver distortion. Furthermore, when the liquid depth is similar to the radar range resolution, the amplitude and time delay measurement can be affected by waveform interactions between the surface and subsurface peaks. To rigorously treat these problems I have developed a simulator of the Cassini radar altimeter echoes coming from liquid bodies of Titan. I simulate the Ku-band altimetry signal

received from Titan's seas using a two layer model, where the surface is represented by a specular reflection and the subsurface is modeled using a facet-based synthetic surface. The simulation accounts for thermal noise, speckle effects, analog to digital conversion (ADC), block adaptive quantization (BAQ), and allows for possible receiver saturation. I use a random walk Monte Carlo method to compare simulated and observed waveforms and retrieve the probability distributions of depth, surface/subsurface amplitude ratio and subsurface roughness for each double-peaked waveform. I demonstrate also the possibility to retrieve bathymetric information from the saturated data of the T49 (December 2008) altimetry observation of Ontario Lacus and present a complete analysis of the T91 (May 2013) flyby over Ligeia Mare. This analysis provides the Ku-band attenuation of Ligeia Mare and Ontario Lacus and results in an estimate of their loss tangent and composition. This method could potentially be adopted in several other applications in the field of radar sounding for planetary exploration.

In Figure 13 is shown a complete workflow describing the three subsequent main blocks in which this work can be divided. *Cassini raw signal simulation* takes in input the actual parameters of the transmitted chirped signal and the parameters specifying the synthetic scenario to be generated and gives in output a lookup table containing all the simulated waveforms generated at this first step.

The *Monte Carlo and waveform fitting* block takes in input the real waveform received by the Cassini radar and each one of the simulated waveforms contained in the lookup table (possibly in a parallel computing modality for minimizing time of processing) and gives in output the most probable values defining the scenario that generated such a received echo together with an associated estimation error for each parameter.

The third and last block, called *Estimation*, concerns the determination of a loss tangent value for the media filling the observed liquid body. This is performed by means of an adequate inversion model that takes in input the seafloor roughness, the signal intensity ratio between surface and seafloor echoes and the seafloor estimated roughness providing in output a loss tangent value that will be eventually used for later laboratory measurements able to yield the most appropriate liquid's composition for that value.
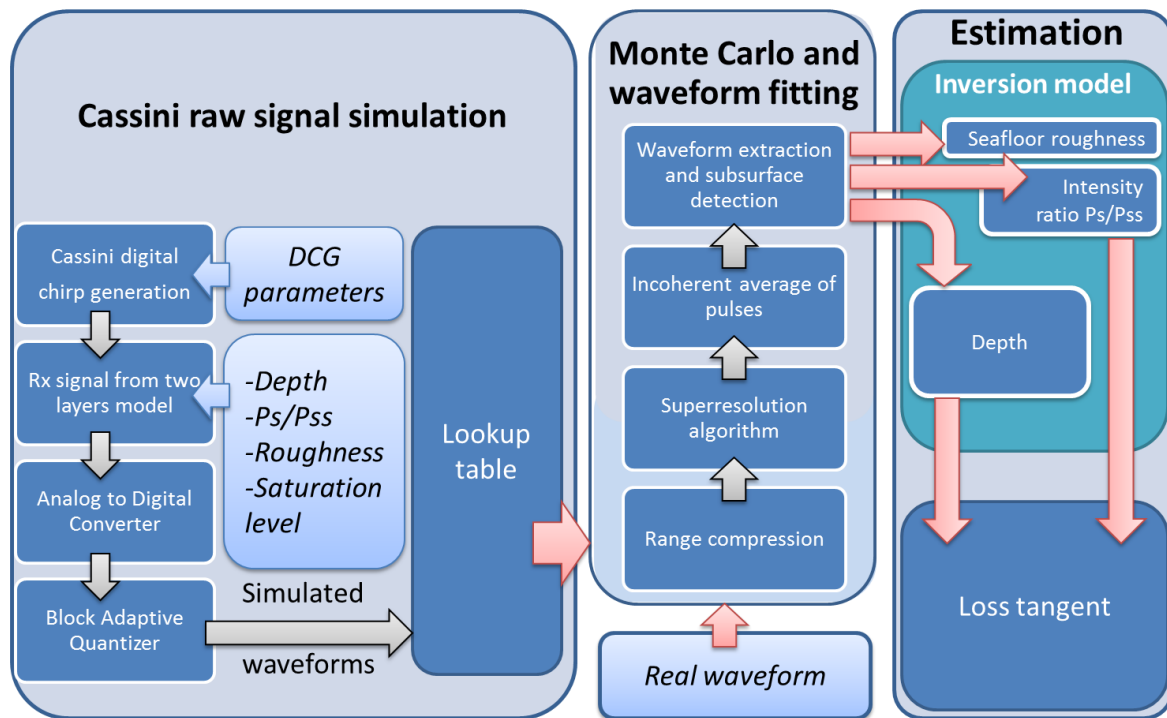
Figure 13: Workflow, signal simulation and estimation of the parameters of interest for Titan liquid bodies.

a. *About the development of a Cassini radar altimeter signal simulator*

In order to simulate the beam limited mode Cassini Radar altimeter waveforms as we receive them from the extremely smooth surfaces of Titan liquid bodies and their sea-beds, I adopted a model with two layers.

The first one, relative to the sea surface, is represented by a flat plane with a small superimposed roughness (i.e. RMS height of 0.5 mm, see [LIII]) and whose radar cross-section can be expressed by that of a sub-satellite single point scatter in accord to the Physical Optics (PO) model (see above).

The second layer is represented by means of facets method [VII] as the coherent addition of all the contributions relative to the single scatterers of which the seabed is composed, each one scaled in amplitude with the appropriate antenna gain (Gaussian beam), incidence angle and scattering function. Furthermore, phase is evaluated by considering the distance of each facet from the spacecraft.

39

Thus, the scattering response can be modelled as a combination of the signals received from the sea surface as well as the seabed and can be written as follows:

$$g(t) = a\delta(t - t_0)\exp(-2jkh) + \sum_i^N \sum_j^M b_{ij}\,\delta(t - t_{ij})\exp[-2jk(r_{ij} + z_{ij})] \qquad [volts]$$

with $t_0 = \dfrac{2h}{c}$, $t_{ij} = \dfrac{2(r_{ij}+z_{ij})}{c}$, h the spacecraft altitude, k the wave number, N and M the number of facets composing the dimensions of the synthetic seafloor generated, r_{ij} the distance from the spacecraft to the sea-surface along each facet direction, $z_{ij} = d_{ij}/\sqrt{\varepsilon_{r1}}$ the apparent additional path within the liquid medium and ε$_{r1}$ its dielectric constant, a is the amplitude of the echo reflected by the sea surface obtained by means of the PO model, b is the amplitude of the echo coming from the seabed (it takes into account surface's dielectric properties and macroscale roughness as well as the attenuation of the signal). Note that the b parameter is set in such a way that it gives the desired Ps/Pss we want to simulate.
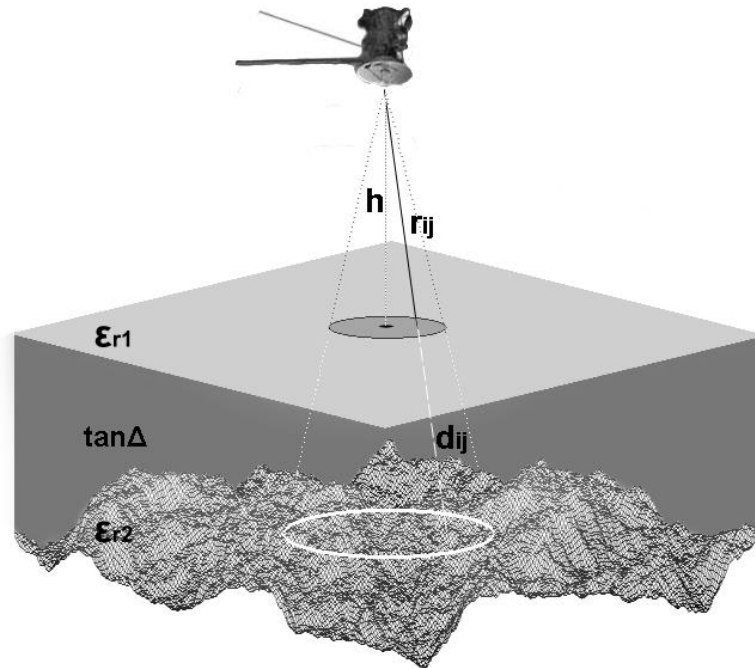
Figure 14. Simulation scenario for altimetric observations of Titan seas, a two-layers model with surface and seabed has been implemented.

The compressed received echo is obtained by means of the following convolution:

$$s(t) = g(t) \otimes m(t)$$

where $g(t)$ is the obtained the scattering response and $m(t)$ the transmitted quadratic-phase signal that is generated by the Digital Chirp Generator (DCG).

Each burst transmitted by the Cassini RADAR altimeter is composed by 21 of these consecutive chirped signals at fixed rate of which at least 13 of them are generally effectively received back within the receiver time window and recorded. The burst repetition interval (BRI) is conveniently adapted according to the science targets of each observation.

In example, designing the T104 flyby observation of Kraken Mare we asked the Cassini Project to perform a nadir observation with the lowest possible BRI in order to have the greatest number of footprints covering the Kraken Mare and, thus, the most accurate determination of composition and the most along-track resolved bathymetry. The Project accorded us a 0.555 s of BRI but, being of great scientific interest the waves height determination as well, they decided to alternate beam 3 (the altimetric one) with beam 1 in order to observe the surface of the sea with a 2.2 deg of off-nadir. The BRI we finally obtained was a good 1.11 s that resulted enough for obtaining tens of bursts over the sea and a continuous along-track acquisition.

The simulator accounts also for the phase of the received signal, as resulting from position and movements of the spacecraft, allowing generation of speckle noise and eventual pulse-to-pulse correlations.

Modelling the scenario in this way I consider multiple reflections to be absent as well as volume scattering between the two layers. I'm allowed to do this simplification because of the typical shape of received waveforms (always two-peaked) and because ethane and methane are the most abundant materials (liquid under Titan conditions) with no solid compounds having the requisite low loss tangent.

I simulate seafloor scenarios larger than the half-power beam footprint and presenting a macroscale geometry described by a fractal function with the Hurst exponent equal to 0.5. All

these choices resulted in an fairly accurate description of the actual scenario, in fact I was finally able to correctly represent the waveforms we received with their intensity ratios between the surface/seafloor reflections and their relative delays, associated to sea's bathymetric depth. These two parameters, together with the RMS height of the macroscale seabed roughness, are the physical values of interest for this study: the parameters that I want to determine for each of the Titan seas observed by the Cassini RADAR altimeter. In the next paragraphs we will see in which way I'm allowed to do this.

b. Bayesian Theory for Parameters Estimation and Monte Carlo method

The problem on which we focus here is the estimation of unknown parameters on the basis of a serie of measurements (each characterized by measurement errors) and by means of a random sampling of the permitted values spaces (each defined by its a priori probability distribution). The basic idea of the Bayesian approach (differently from the frequentist) is the fact that the solution can be represented as a density, rather than a fixed value. Given an a priori knowledge of the possible ranges of variability of the parameters, we will select for each of them the most likelihood (most probable) value, that we will also call the maximum a posteriori value (MAP). In this frame, maximum likelihood is thus associated to the value characterized by the highest number of occurrences (mode) for the obtained posterior distribution. Moreover, the upper and lower bounds of the errors of this estimation can be directly read on the distribution as n-sigma quantiles.

Let's assume that the Likelihood could be written as

$$L(\mu|x) = P_\varepsilon\big(\mu - f(k, x)\big)$$

with k representing the a priori knowledge, x the unknown parameters, μ the measurements, P_ε the Probability density function (PDF) of the error.

We are basically assuming that the measurement error is independent from the unknown parameters and, thus, that the difference between the measurements and the predicted values has the same PDF of the error. If we assume that measurement errors are independent and normally distributed the combined likelihood for all the measurements can be described by the following PDF:

$$L(\mu|x) = \prod_{i=1}^{N} P(\mu_i|x) = \frac{1}{(2\pi\sigma^2)^{N/2}} e^{-\frac{1}{2\sigma^2}\Sigma_{i=1}^{N}(\mu_i - f(k_i,x))}$$

with $P(\mu_i|x)$ the likelihood for a certain measurement i.

In the frame of this work, the a priori knowledge about our parameters refers only to their range of variation, that's why we will consider for them simply a uniform prior in that interval. The final range of investigation is the result of a progressive reduction from the whole and coarse resolved interval of variation of the parameter of interest to an higher resolved range that will contain its entire final a posteriori distribution.

Thus, being uniform the prior distributions, the MAP value will identifies with the Maximum Likelihood Estimate:

$$MLE = \max_{x} L(\mu|x)$$

that is equivalent to minimizing $-\log L(\mu|x)$, a function that is easier to optimize and that can result more suitable for least square minimization routines.

Methods capable of generating stochastic realizations of a variable by sampling them from a given arbitrary probability distribution are called "Monte Carlo (MC) methods". For my radar echo simulations, I'm interested in sampling the normal distribution for generating the thermal noise that has to be summed to the radar signal of interest. In this regard, the noise level measured in the time interval between the echoes composing the received Cassini burst becomes the mean value around which the normal distribution is centered.

c. Generation of synthetic discrete sampled rough surfaces

Here I would like to describe the process of generation of scale-model representations of Titan sea bottom useful for radar signal simulations. Surfaces I consider are statistically characterized by the properties of homogeneity, isotropy and ergodicity and defined as a realization of a random process described by a power-spectral density (PDS) following a power-law form over a portion of the spectrum. Furthermore, I define the root mean square of the surface roughness σ_h as the standard deviation of probability density function (PDF) of surface height, which assumes, for real random rough surfaces, Gaussian shape as a consequence of the central-limit theorem.

In the spectral domain the fundamental statistical descriptors of a Gaussian random process are fully expressed by means of the higher-order statistical descriptors of its PDS, whose Fourier transform is related to its autocorrelation function (defined as the auto covariance function normalized by the variance of the PDF).

Another way to describe random surfaces characterized by such power law weighted PDS is by means of self-affine stochastic fractals geometry. In practical realizations however, it will be necessary to apply high and low cutoff to the power law form of the PDS that will limit the range of scales on which such a correspondence applies. Fourier transformation can be effectively used to generate discrete sampled surfaces where high and low cutoffs will correspond to sampling interval and array size, respectively.

In my simulations, the process of generation of a synthetic surface starts with the generation of a PDS by means of a 2D Fast Fourier Transform (FFT) of a spatial matrix of normally distributed random numbers. This matrix will already have the dimensions of our simulation scenario.

For sea-topography generation it is typical at this point to weight this PDS with an inverse power law function $k^{-\gamma_2}$ of the radial spatial wavenumber k with $\gamma_2 >2$. In my simulations I chose $\gamma_2 = 2.5$. Thus, the resulting PDS can be written as $s/(rk)^{\gamma_2}$ with r the reference length (unit) and s the spectral strength expressed in number of units. This PDS is finally cutted at low and high cutoff values (that I have chosen to be 0 and 3) in such a way that elsewhere will be equal to zero.

Going back to the spatial domain it is possible at this point to set the required statistics of the surface to the desired RMS height.

In order to simulate the backscattering response from a rough surface I decided to approximate it with the Facet Method. A serie of planar facets, each one tangent to the actual surface and behaving like reflectors characterized by a radiation pattern and by an orientation, have been used to model the surface illuminated by the radar wave. The overall surface response, radiated back to the radar, is the sum of all the responses from the facets. In my simulation I chose a 200 m square facets distributed on a squared scenario 1,5 times bigger the actual -3dB Cassini footprint.

Moreover, the amplitude of the signal backscattered by each facet is dependent from the dielectric properties of the material composing the surface (the Fresnel reflection coefficient) and from its microscale roughness (in terms of RMS slope σ_s). Among the possible models that can be adopted to determine the backscattering coefficient I chose the Hagfors model [XII], that has often been used for planetary gently-undulating-surfaces applications (i.e., the analysis of Pioneer-Venus and Magellan radar altimeters data):

$$\sigma^0(\vartheta) = \frac{\Gamma \, h_c (\cos^4 \vartheta + h_c \cos^2 \vartheta)^{-1,5}}{2}$$

with ϑ the angle between the normal to each facet and the segment connecting the radar to the facet itself, Γ the Fresnel reflectivity, h_c is equal to the inverse square of σ_s (which has been set constant at 15 deg).

These backscattering values need finally to be weighted by the Cassini antenna pattern, roughly assimilable to a Gaussian, that distinguishes among facets falling right in the antenna pointing direction from others far away.

d. Saturation and artefacts

During its thirteen years of observations (Ta-T126) the Cassini RADAR altimeter has achieved precise global measurements of the mean elevation and backscattering of Titan's surfaces. The extreme variety of observed scenarios, shown also by SAR images, is perfectly reflected in the rich altimeter dataset that is composed by forty different acquisitions. Not a few difficulties have to be addressed in order to give an effective interpretation of radar returns. This task is challenging

45
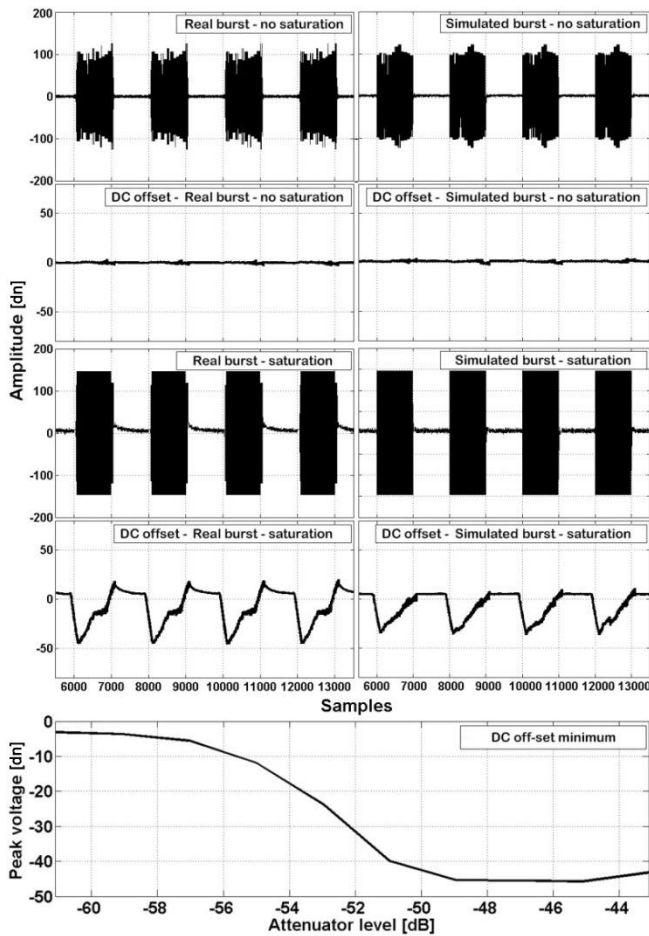
Figure 15: On the left column some chirped signals recorded during an engineering test performed during the flyby T56 are shown in the case of saturation and without saturation, they are alternated with the relative DC offset obtained by low pass filtering the signal using a uniform moving window of 20 μs. The same graphs obtained for simulated signals are shown on the right column. The lower panel indicates the minimum value of dc offset varying the attenuator level set. Saturation starts from a value of −58 dB.

because radar measurements are affected by thermal noise and speckle, and sometimes by distortions and processing artifacts as well. On a total of about 28000 bursts acquired by the Cassini radar altimeter, less than 1% of them is strongly peaked, and resembling the radar impulse response. All these echoes pertain to footprints illuminating (totally or in part) liquid bodies' surface and exhibit the presence of well-defined pre- and post-cursors symmetrically centered about the main echo returning from the smooth surface of the sea. These features can be identified as the effect of instrument saturation, whose effects have been observed in a number of missions on which altimeters flew, i.e. on Skylab, GEOS-3 and Seasat. In 1987, D. J. Wingham & C. G. Rapley [XLIX] demonstrated that, analyzing Seasat radar returns, it was possible to develop an analytic model of the consequences of saturation, and showed these echoes to coincide with the expected location of saturation artefacts.

In order to analyze these narrow-peaked waveforms, we need a deep understanding of the saturation mechanism that could result only from a precise simulation of the raw Cassini radar altimeter waveform. This simulation must incorporate all the operations that are applied by the on-board system and subsequent ground processing, allowing it to reproduce processing artifacts, including saturation effects introduced by the analog to digital conversion (ADC) and block adaptive quantization (BAQ) systems [XX].

When saturation occurs, the 8-bit Analogue Digital Converter (ADC) of the Cassini RADAR reception chain causes an hard clip of the signal amplitude. The incoming chirped signal can be

represented only in a range of 255 discrete values of digitized voltage (dn), with the extreme negative and positive amplitudes being represented by -127.5 and +127.5 dn, respectively (see Figure 15).

In order to reduce the downlink data rate of the Cassini RADAR altimeter, an 8 to 4 bit Block Adaptive Quantization (8-4 BAQ) compression algorithm is applied on-board. This method introduces some effects in the final data that should be understood in order to recover the actual signal values received.

TX	RX
1111 if X < -1,1000Th	-1,2490Th if Y = 1111
1110 if -1,1000Th <= X < -0,8400Th	-0,9455Th if Y = 1110
1101 if -0,8400Th<= X <-0,6550Th	-0,7395Th if Y = 1101
1100 if -0,6550Th<= X < -0,5000Th	-0,5740Th if Y = 1100
1011 if -0,5000Th<= X < -0,3650Th	-0,4305Th if Y = 1011
1010 if -0,3650Th<= X <-0,2375Th	-0,3000Th if Y = 1010
1001 if -0,2375Th <= X < -0,1175Th	-0,1775Th if Y = 1001
1000 if -0,1175Th<= X < 0	-0,0585Th if Y = 1000
0000 if 0 <= X < 0,1175Th	1,2490Th if Y = 0111
0001 if 0,1175Th<= X < 0,2375Th	0,9455Th if Y = 0110
0010 if 0,2375Th <= X < 0,3650Th	0,7395Th if Y = 0101
0011 if 0,3650Th <= X < 0,5000Th	0,5740Th if Y = 0100
0100 if 0:5000Th <= X < 0,6550Th	0,4305Th if Y = 0011
0101 if 0,6550Th <= X < 0,8400Th	0,3000Th if Y = 0010
0110 if 0,8400Th <= X < 1,1000Th	0,1775Th if Y = 0001
0111 if 1,1000Th <= X	0,0585Th if Y = 0000

Table 4: this table reports the 16 words used by the 8-4 BAQ algorithm to encode on board the received block samples.

Each burst of 15 echoes consists of 30000 samples. Each echo is represented by a 2000 samples, that are divided in 24 blocks of 83 samples.

The algorithm requires calculation of a vector of 24 block variances estimated from the first and last 4 echoes of each burst by using the first and last 8 samples of each block.

A threshold value equal to Th=0.98/F(μ), with

$$F(\mu) = 127.5 - \sum_{n=1}^{127} erf\left(\frac{n}{\sigma\sqrt{2}}\right)$$

is finally obtained for each block. It will be used in order to represent the value of each sample contained in that block by means of the Table 4, here reported.

When it happens that the dynamic range of the RADAR receiver is not wide enough to represent the incoming signal, we have saturation and the BAQ algorithm incurs in a degradation of its coding capabilities that causes the signal to assume levels from a reduced set of 10 values instead of 16 (in these cases Th reaches its highest value of 254).

The attenuation level adopted during each RADAR observation starts from a value that is determined prior to the flyby and, during the passage, it depends on the ability of the receiver auto-gain function to adapt to the incoming signal levels. The auto-gain increases and decreases

the level of attenuation with steps of 2 dB every 50 burst by evaluating the signal level of the last burst of the preceding group.

In order to investigate about the possibility of recover the actual signal values from those bursts affected by severe saturation we analyzed the data acquired during an in-flight engineering test conducted during the flyby T56. During this experiment ten bursts were routed directly from the transmitter to the receiver while incrementing the level of attenuation with steps of 2 dB. This opportunely caused different levels of saturation to occur.

In an attempt to study distortions introduced by saturation, I low-pass filtered with a moving window (20 µs long) the received bursts. When saturation occurs, a time varying DC offset of the received signal is produced by variations in the amplitude level input to the ADC. I reproduced this phenomenon by adding a linear decreasing time varying function (a downward ramp) with slope that increases with increasing saturation levels to each signal of the burst.

As a matter of fact, from the adopted attenuation level depends the level of saturation occurred during Titan's seas observations. As shown in the lower panel of the Figure 15, I have been able to plot a curve that describes how the lowest peak voltage of the filtered burst varies with the attenuation level. This means that, if the saturation is not too severe, the information relative to the actual signal amplitude is not lost.

Thus, let's consider radar altimeter observations acquired on the sea far away from coastlines and whose echoes were not saturated. After an adequate scaling for the spacecraft altitude and the coherent scattering contribution, it is possible to take the amplitude of the most powerful among them (indicative of a flatter surface) as a reference for reconstructing the actual signal amplitude of the saturated signals. All you need is to make vary the proportionality constant that exists between attenuation and saturation levels until you reach the echo amplitude as it was received by the Cassini radar altimeter during the observation (level of saturation can be opportunely described by a variable $C >= 0$, with saturation corresponding to values >1). The constant obtained in this way can be used to reconstruct the actual signal amplitude for those observations relative to the nearby surrounding marine areas.

As a further comment on the Figure 15, it is interesting to note how the simulated signals result comparable with the distorted ones acquired during the engineering test. The lower panel function shows a maximum slope of 2.3 dV/µs for an input amplitude of 570 dV. The DC offset minimum value decreases monotonically from about 0 dV to -45 dV for a range of ADC input

amplitudes from 90 dV (when saturation occurs at -60 dB) to 450 dV (-48dB, in Figure 15) respectively, and after that tends to be constant up to 570 dV (-45 dB).

e. Burg's superresolution algorithm

The 4.25MHz chirp bandwidth of the Cassini RADAR altimeter allows production of relative elevation profiles with a vertical resolution of about 35 m. The limited number of observations and the fact that we will not have a chance to repeat them for years to come (at least until a new spacecraft will come back to Titan) requires us to find new ways for processing this altimetric dataset in order to extract all the information herein contained. Especially acquisitions over the seas are extremely important in order to assess the total liquid hydrocarbons volume and global environmental conditions on Titan.

Approaching the shorelines, a shallower sea can make some bathymetric measurements really challenging if compression schemes based on the conventional Fourier techniques are adopted. The range resolution and side lobe levels of the Cassini RADAR system depend mainly on the shape and extent of the signal spectrum. In general, we should overcome the idea that the unavailable data samples beyond the lower and higher edges of the frequency window are just zero. The application of an parametric autoregressive (AR) time-series model can effectively be used in order to improve range resolution of coherent radar returns by making realistic assumptions about the sinusoidal properties of the target's frequency response, especially in those cases in which it consists in the superimposition of sinusoids from a series of discrete scattering centers.

As a result, extrapolation of the received signal prior to pulse compression can produce an improvement in the range resolution of a factor up to x4. Furthermore, the linearity of this kind of processes makes recompressed pulses still suitable for backscattering and phase responses studies.

These extremely promising methods, like the Burg's Maximum Entropy Method (MEM) that I applied on Cassini data, are based on the idea that an equi-spaced set of signal samples multiplied by a set of complex weights, or prediction coefficients, will predict the next sample. These coefficients are obtained by minimizing the error between predicted and measured signal values and can be used to make prediction in the forward direction as well as in the backward (in the latter case complex conjugates of the weights must be used).

49

The Burg's method adds a further control on the extrapolated data by preventing it to exponentially increase in amplitude. The recursive procedure that allows this pretty good stability (Levinson recursion) permits to obtain single coefficients at each step by means of a sequence of least-square minimizations. Choosing a number of coefficients significantly higher than the expected number of sinusoids composing to the signal spectrum can prevent these unwanted effects. With respect to this choice, simulations showed that the use of too many coefficient may increase the noise level in the output time-serie and that a bandwidth extrapolation factor of 3:1 could be more appropriate, bringing a final effective increase in the SNR as the noise presents lesser effects in the expanded bandwidth.
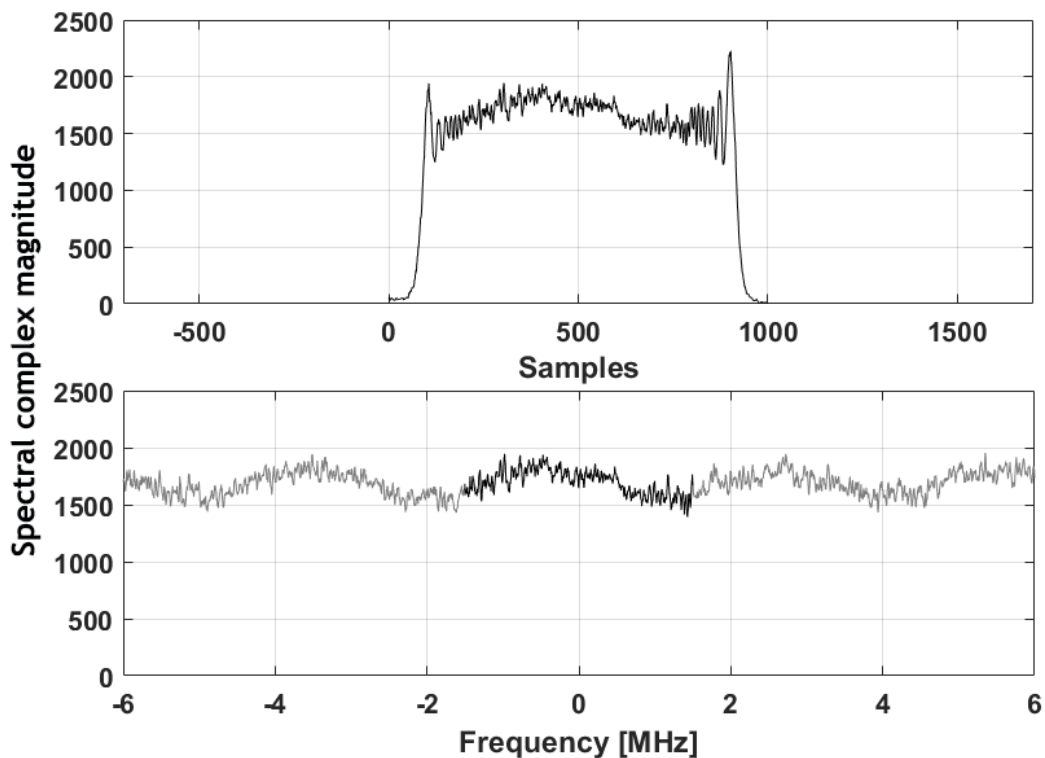
Figure 16: Example of x4 bandwidth extrapolation of a simulated pulse spectrum received from a 2 layers scenario for which I imposed 20 m of separation between the interfaces, 15 dB of Ps/Pss ratio and 0 m of RMS vertical roughness for the second interface. In the upper panel the original 4,25 MHz signal bandwidth, in the lower panel the extraction of the central 3 MHz (in black) is followed by a backward and forward extrapolation leading to a final bandwidth of 12 MHz (black + gray). For increasing visual clarity the spectrums have been filtered with a moving average filter with a span of 5.

In conclusion, the application of the Burg's method can be very useful in the Cassini RADAR data processing and analysis, as it can increase the system range resolution (up to 10/15 m) and detection possibilities of closely spaced point scatterers (i.e., sea surface and seafloor), but it

50

should also be taken into account that frequency dependences (like resonance), that are not predictable from the measured spectral signal, may cause the extrapolated data not always to perfectly represent the true signals at larger bandwidth.

As already mentioned, in my work I apply the Burg algorithm with an extrapolation factor of x4, this results particularly suitable for extracting bathymetric information wherever the echoes from sea surface and sea floor tends to merge because of the shallowness of the marine areas closer to the coastline (see Figure 17). In order to perform an accurate bandwidth extrapolation and achieve a real improvement in resolution, it is also important to avoid data samples near the edges of the spectrum, this because the greatest spectral distortion effects due to the Fresnel ripples are located right in these regions. In my case, for instance, of the 4.25 MHz Cassini radar altimeter bandwidth I used about 3 MHz, taken from the central portion of the spectrum (see Figure 16).
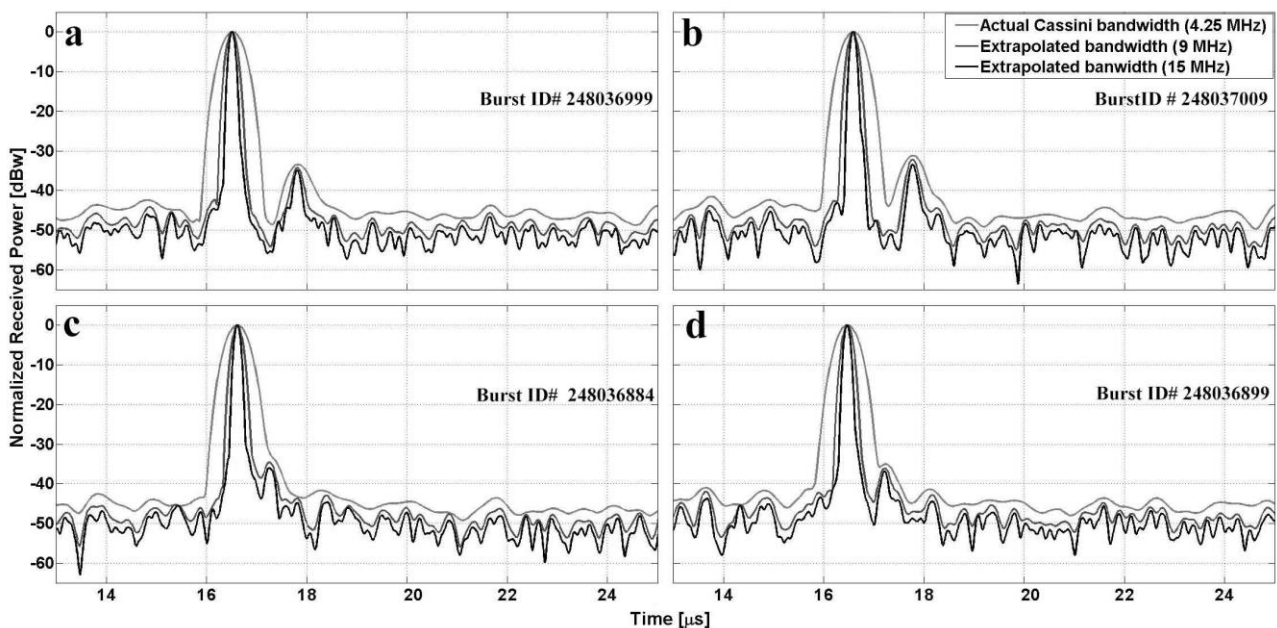
Figure 17: Burg's Maximum Entropy Method applied to Cassini T91 altimeter data in order to improve resolution for coastal bathymetry measurements. Superresolution methods can be very useful when it happens that the seafloor echo is very weak respect to the surface one, and a taper window with a strong sidelobes attenuation is needed to bring out the hidden subsurface signal. The application of such strong windows, like Blackman or Chebyshev, causes a worsening in resolution that can be mitigated thanks to these methods. As shown, superresolution allows to distinguish surface from subsurface peaks under the nominal radar range resolution (c, d) and improve the time distance measurements of surface-subsurface peaks (a, b).

CHAPTER IV
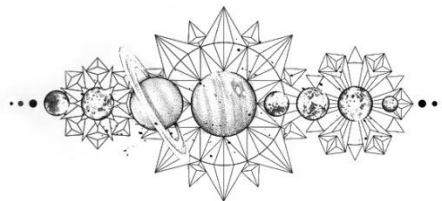
MONTE CARLO SIMULATION, WAVEFORM APPROACH AND LOSS TANGENT ESTIMATION

The properties of Titan's seas I want to investigate are seafloor depth and its roughness, as well as the amplitude ratio between the echoes received from the surface and the seafloor. The latter, in particular, is very important if combined with the knowledge of the depth because it can allow estimations of the dielectric properties of the liquid, when appropriate assumptions about the composition of the seafloor are made.

The need for a statistical approach to these measurements is driven by the necessity to determine the most probable values for these parameters as well as the associated estimation errors. Errors that, necessarily, come from those speckle and additive white Gaussian noise (AWGN) that have been carefully added to our simulations, in accordance to what is possible to measure in real data in the inter-pulse regions of the received bursts. Furthermore, wherever saturation applies, noise is scaled according to the attenuator level by using the relationship found by Lauren C. Wye in her PhD dissertation:

$$y = ae^{bx} + ce^{dx}$$

where a = 43407, b = -0.215, c = 46.9 and d = -0.049 and where y is the noise power measured in dW and x is the logarithm of the total attenuation loss.

a. *Random walk Monte Carlo method guided least square minimization and posteriori probability density functions for the retrieval of best-fit values (depth, Ps/Pss, seafloor roughness).*

After pulse recompression and incoherent average of the pulses contained in each burst, namely the final steps of the processing chain that allows the final simulated altimetric sampled time waveforms to be obtained, these echoes are stored in a lookup table that will be conveniently used for the successive least squares minimizations stage for comparing simulated and received waveforms. The dimension of such a table depends on the width of the model space that we need to explore. In our case we move in a 3-dimensional space, of which we need to determine the edges. In order to pursue my goals I took advantage of the availability of 6 powerful PCs, each equipped with 12 core at 2.1 GHz and supplied by the Cornell Center for Astrophysics and Planetary Science (CCAPS).

As an initial idea the ranges of values that should be selected are centered around the set of values primarily measured directly on the received waveforms. For Ligeia Mare, i.e., this a priori knowledge of depth and intensity ratio could be also extracted from "The bathymetry of a Titan sea" by Mastrogiuseppe et al. and dating back to 2014 [XXVIII]. As already mentioned above, starting from coarse resolved intervals of variation for the parameters, I progressively identified the final high resolved ranges of investigation that contain the entire final a posteriori distributions (see Figure 18). For what concerns the seafloor roughness (RMS height) range of values to be simulated, let's consider that this should be set to vary only from 0 m to depth/2. Greater values, in fact, would imply a partially exposed seabed topography (islands or headlands), which do not appear in the SAR images relative to the marine areas under analysis.

I explored depth and vertical roughness spaces with a 2 m step, and the intensity ratio (Ps/Pss) space with a 1dB step. These choices lead finally to a number of combinations of 29403 for Ligeia Mare, and 5890 for the shallower Ontario Lacus. For each triplet of values, I stored in the lookup table a thousand of different Monte Carlo realizations, for a total amount of stored waveforms of about 29,4 million. Such big lookup tables would take a great storage space, that's why I eventually decided to store only a 2 μs window of the resulting waveform appropriately centered around the normalized surface peak. These are the final time vectors that will be fitted to the real waveforms, in order to find the ones that minimize the 3-D error function by means of a least square procedure.
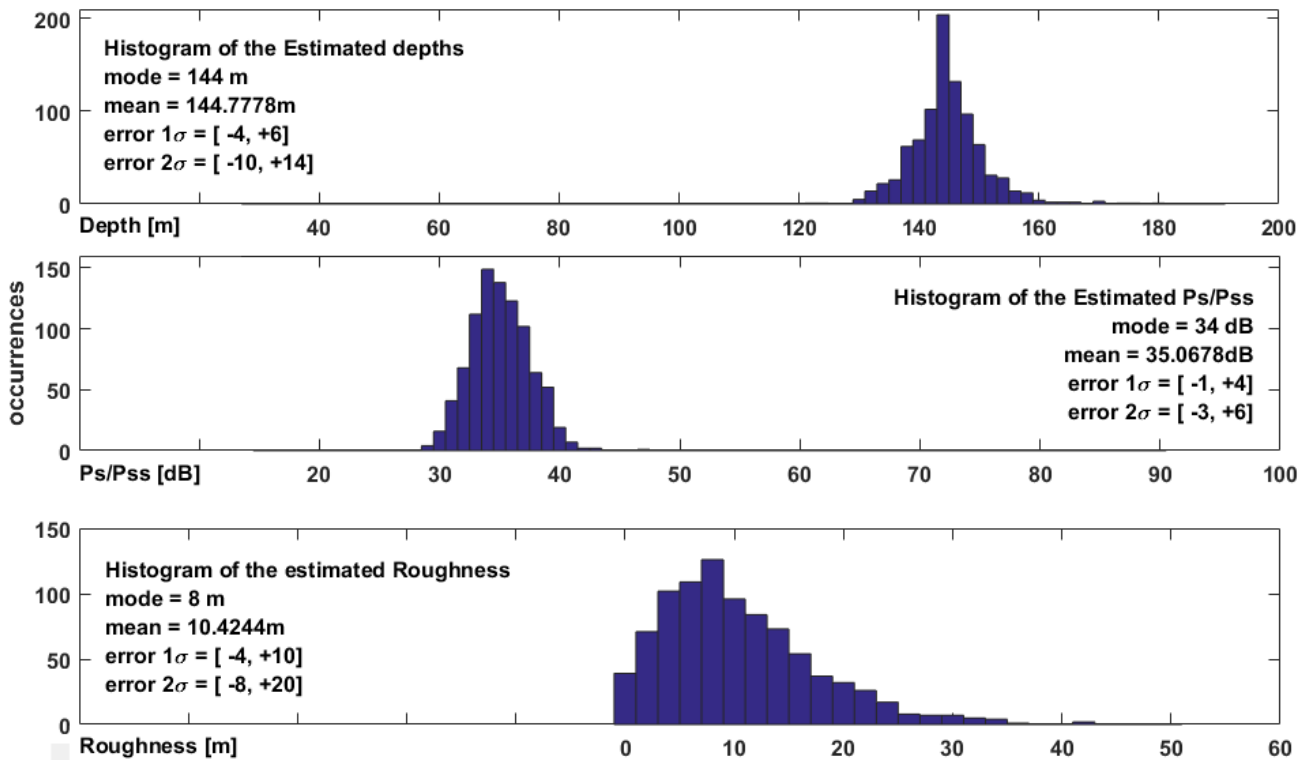
Figure 18: Example of the obtained final a posteriori distributions. These are relative to burstID#248037004 of flyby T91 over Ligeia Mare. In these histograms the MAP can be associated to the mode and the estimation errors to the 1- and 2-sigma intervals of confidence (indicated with respect to the mode value).

The Bayesian like approach here adopted allowed me to retrieve the triplets of most probable values (maximum a posteriori probabilities or MAP) and their relative triplets of intervals of confidence (posteriori probability density functions). This approach has been successfully applied for estimating the three parameters of interest for each of the 35 Cassini bursts acquired over Ligeia Mare and each of the 31 relative to the Ontario Lacus. The reader may look at the attached Figure 18, that shows one of the retrieved triplets of probability density functions, each associated to the three parameters of interest depth, intensity ratio and seabed roughness.

For Ligeia Mare the retrieved best fit parameters (see Table 5) depict this liquid body as divided in two distinct regions at 80° N latitude by the presence of an elevated seafloor feature. However, the two areas appears as characterized by similar posteriori distributions of depths and, thus, likely by similar roughness characteristics. We will come back later, in chapter V, to a deeper analysis of the characteristics of the retrieved distributions.

For what concerns Ontario Lacus, the Ps/Pss ratio is quite smaller than Ligeia Mare (see Table 6), presumably due in part to the shorter column of attenuating liquid, in fact depths here

are only a few tens of meters, close to the resolution limit of the Cassini RADAR instrument and quite far from the inferred depth of Ligeia of about 160 m.

Latitude (°)	W Longitude (°)	Depth (m)	1σ down (m)	1σ up (m)	PsPss (dB)	1σ down (dB)	1σ up (dB)	Roughness (m)	1σ down (m)	1σ up (m)
82,37	242,31	50	-14	6	21	-4	3	10	-4	2
82,21	242,27	44	-2	10	23	-2	4	10	-2	2
82,05	242,23	54	-4	4	29	-2	2	10	-4	2
81,89	242,18	42	-2	10	30	-2	3	8	-4	2
81,73	242,15	68	-4	6	33	-2	3	14	-8	0
81,57	242,11	74	-6	10	29	-3	2	16	-2	2
81,41	242,08	90	-12	6	29	-2	3	18	-4	4
81,25	242,04	88	-6	6	36	-2	3	10	-8	8
81,08	242,00	98	-16	6	34	-2	3	20	-6	2
80,92	241,98	100	-8	4	33	-1	3	8	-2	10
80,75	241,94	92	-2	26	44	-3	3	14	-10	8
80,58	241,90	102	-10	6	41	-2	4	2	0	16
80,41	241,84	114	-10	14	39	-3	2	22	-12	6
80,25	241,79	122	-16	10	43	-3	3	20	-16	6
80,08	241,73	104	-10	13	40	-3	2	20	-12	2
79,90	241,68	66	-2	24	40	-1	7	12	-8	4
79,73	241,63	124	-12	26	42	-1	6	22	-18	6
79,56	241,58	150	-26	28	41	-3	5	30	-18	6
79,39	241,52	150	-10	26	45	-4	3	18	-8	16
79,21	241,48	182	-18	4	38	-2	3	30	-14	8
79,04	241,43	154	-8	2	40	-1	6	0	2	18
78,87	241,38	162	-18	18	47	-4	2	0	4	33
78,70	241,36	148	-2	34	43	-2	4	0	4	32
78,52	241,33	166	-10	16	38	-1	5	22	-10	12
78,35	241,31	148	-2	30	40	-3	2	28	-18	8
78,17	241,28	148	-8	6	38	-3	2	14	-8	10
78,00	241,26	148	-4	6	37	-3	2	6	-4	9
77,82	241,24	144	-4	6	34	-1	4	8	-4	10
77,64	241,22	136	-2	10	35	-2	3	4	-2	14
77,46	241,19	132	-2	4	32	-1	3	2	0	12
77,29	241,17	122	-6	12	31	-2	2	22	-10	6
77,11	241,15	120	-10	8	35	-2	2	20	-8	6
76,93	241,12	114	-3	8	34	-2	2	8	-4	10
76,75	241,10	110	-10	10	36	-2	3	22	-10	2
76,57	241,08	76	-4	10	33	-2	3	12	-4	4

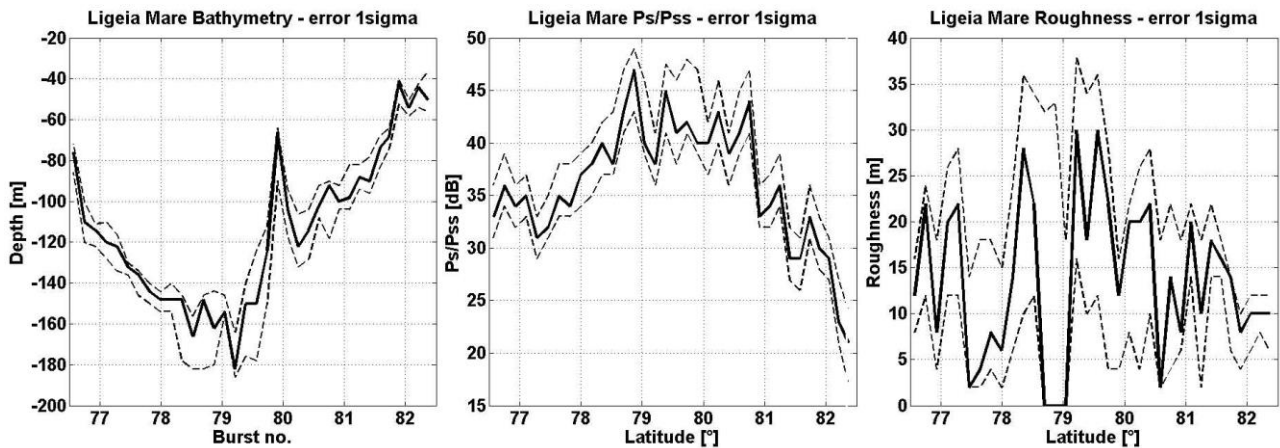**Table 5: Estimated values and relative errors obtained for Ligeia Mare**

Figure 19: Estimated values and relative errors obtained for Ligeia Mare

Latitude (°)	W Longitude (°)	Depth (m)	1σ down (m)	1σ up (m)	PsPss (dB)	1σ down (dB)	1σ up (dB)	Roughness (m)	1σ down (m)	1σ up (m)
-73,54	-0,53	**12**	0	2	**14**	0	2	**0**	0	4
-73,53	-0,42	**12**	-2	0	**13**	-1	1	**4**	-2	0
-73,52	-0,30	**44**	-8	14	**12**	-1	2	**16**	-4	6
-73,51	-0,18	**14**	0	14	**14**	-2	1	**6**	-2	4
-73,51	-0,06	**36**	-28	2	**10**	0	14,5	**0**	0	12
-73,50	0,05	**12**	-1	4	**14**	-2	1	**4**	-4	0
-73,49	0,17	**24**	-2	6	**10**	0	1	**2**	-2	8
-73,48	0,29	**14**	-2	10	**15**	-1	4	**0**	0	4
-73,47	0,41	**18**	-2	10	**13**	-2	2	**6**	-2	4
-73,46	0,52	**20**	-2	10	**11**	-1	1	**4**	-2	4
-73,45	0,63	**20**	0	16	**14**	-2	3	**10**	-6	2
-73,44	0,74	**28**	0	0	**17**	-1	0	**0**	0	4
-73,43	0,86	**26**	0	2	**19**	-3	0	**0**	0	10
-73,42	0,97	**12**	0	14	**13**	0	5	**4**	-2	4
-73,42	1,09	**52**	-26	2	**26**	-6	0	**6**	-2	8
-73,41	1,20	**46**	-10	6	**22**	-5	2	**8**	-2	8
-73,40	1,32	**20**	0	10	**14**	-1,5	1	**0**	0	10
-73,39	1,43	**20**	0	18	**14**	-2	3	**6**	-4	6
-73,38	1,55	**34**	-6	10	**14**	-3	1	**10**	-2	6
-73,37	1,66	**32**	-14	4	**16**	-5	0	**2**	0	10
-73,36	1,77	**16**	2	28	**10**	0	4	**6**	-2	10
-73,35	1,89	**32**	-8	6	**19**	-4	1	**4**	-2	6
-73,34	2,00	**48**	-8	16	**15**	-1	3	**18**	-6	6
-73,33	2,11	**42**	-6	14	**15**	-3	1,5	**16**	-6	6
-73,32	2,22	**14**	0	6	**16**	-1	4	**0**	0	6
-73,30	2,33	**12**	0	50	**14**	-1	4	**18**	-14	6
-73,29	2,45	**20**	-8	40	**19**	-6	2	**4**	-2	16
-73,28	2,56	**16**	-4	38	**21**	-2	3	**0**	0	18
-73,27	2,67	**10**	22	56	**17**	-2	3	**18**	-8	8
-73,26	2,78	**16**	-2	14	**19**	-6	2	**8**	-6	2
-73,25	2,89	**10**	0	0	**14**	-2	1	**0**	0	4

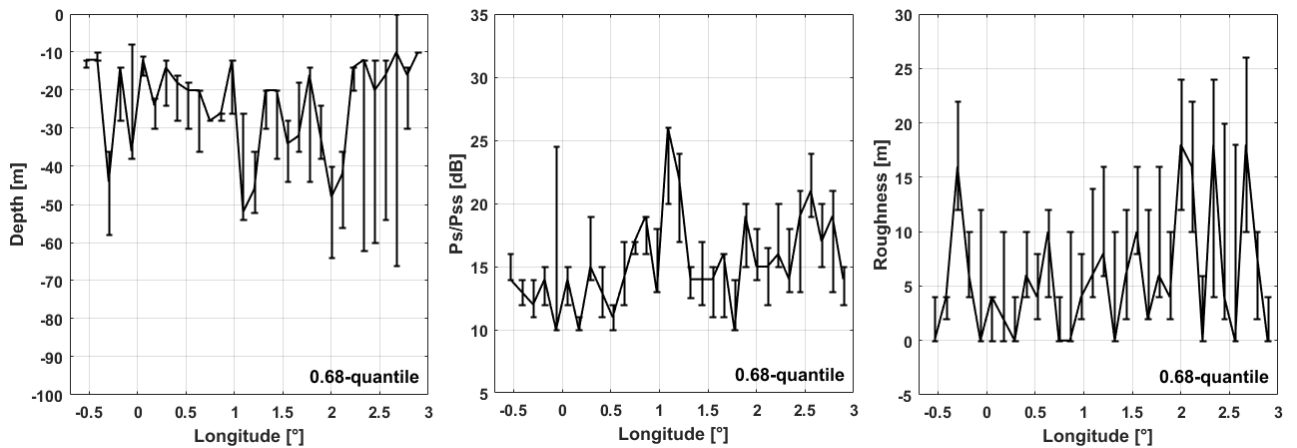**Table 6: Estimated values and relative errors obtained for Ontario Lacus**

Figure 20: Estimated values and relative errors obtained for Ontario Lacus

b. *Parametric inversion model for the retrieval of dielectric properties of the liquid*

As already mentioned above, the best-fit values can be identified with the modes of the retrieved discrete posteriori probability density functions and, in order to establish the relative measurement errors, we calculated 0.025, 0.16, 0.84, 0.975 quantiles, thus obtaining the 1- and 2-sigma confidence intervals of these probability distributions. The results for Ligeia Mare and Ontario Lacus are resumed in the attached tables and figures, which graphically show the retrieved most probable values, reported with errors indicated with a 68% confidence interval (one-sigma).

Furthermore, Figure 21 shows the radargrams obtained by processing the data of T49 and T91 fly-bys.
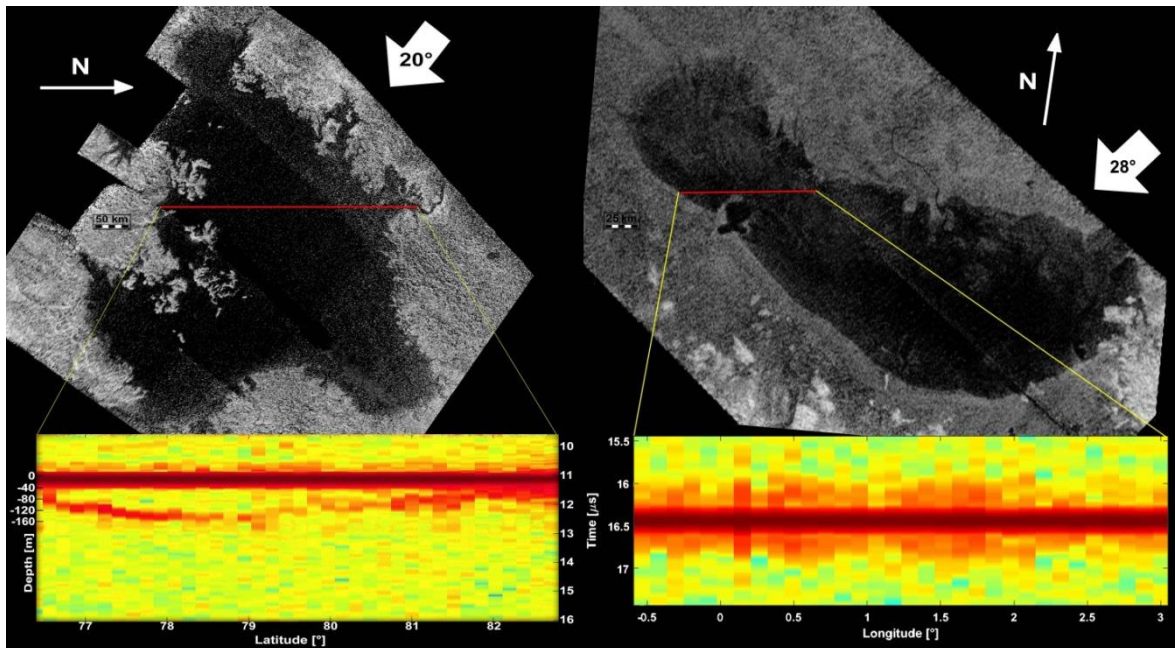
Figure 21: In the left panel it is shown the whole Ligeia Mare from the T25 SAR acquisition, with the ~300 km long T91 altimetry track superimposed. The radargram obtained by processing T91 data is shown as well, with scales in time (right) and in depth (left). The right panel shows the radargram obtained during the T49 fly-by of Ontario Lacus. Blackman taper and Burg x3's superresolution were applied here. Although the presence of seafloor signal is indubitable for Ontario Lacus, it is clear that saturation caused the presence of several artefacts (i.e. time symmetric precursors). The shallowness of the lake respect to Ligeia can be clearly noted here also by visual inspection of the reduced time scales from which lakefloor signals came back to the radar.

The range of values of the three parameters that has been necessary to explore for Ontario Lacus has been less extended than in the Ligeia Mare case. Our a priori knowledge, derived from the received waveforms, allowed us to let the depth vary from 0 to 90 m for Ontario and from 0 to 190

m for Ligeia. The intensity ratio, on the other hand, varied from 10 to 50 dB for Ontario and from 15 to 50 for Ligeia. Finally the RMS vertical roughness solutions have been bounded for Ontario between 0 and a maximum of 15 m. The latter value resulted in some cases lower than depth/2, but this is still acceptable if we consider that the RMS vertical roughness of the terrains outside the lake resulted by my measurements to be approximately of 5 m. For Ligeia, finally, I let the roughness vary from 0 to a maximum of 90 m.

The results obtained in the first step of this work are now exploited in order to retrieve the dielectric properties of the sea, that I modelled as an ideal two layers scenario in which the dielectric properties do not vary neither along track nor along the path traversed by the signal in the medium.

The following step consists in the estimation of the loss tangent of the liquid and in the definition of a possible composition of the medium traversed by the signal during its 2-ways path from the sea surface to the bottom. In order to obtain this result I need a parametric inversion model expressing the specific attenuation of the medium by means of the linear relationship eventually existing between the retrieved sea depths and power intensity ratios Ps/Pss (the latter, in logarithmic scale). It is important to consider that we need a specific 2 layers model able to describe such amplitude ratio between surface ad subsurface reflections by taking into account the depth of the sea, the dielectric properties of the medium and the seafloor, as well as the roughness at the interfaces.

If we represent the backscatter received from the surface (S) and the subsurface (SS) respectively as $\sigma_S = \Gamma_S * f_S$ and $\sigma_{SS} = \Gamma_{SS} * f_{SS}$ it is possible to describe the received intensity ratio as [XXXIV]:

$$\left[\frac{P_S}{P_{SS}}\right]_{dB} = [\Gamma_S]_{dB} - [1 - \Gamma_S]^2_{dB} - [\Gamma_{SS}]_{dB} + [K]_{dB} + \left[\frac{f_S}{f_{SS}}\right]_{dB}$$

with:

$\Gamma_S = \left|\frac{1-\sqrt{\varepsilon_1}}{1+\sqrt{\varepsilon_1}}\right|^2$ and $\Gamma_{SS} = \left|\frac{\sqrt{\varepsilon_1}-\sqrt{\varepsilon_2}}{\sqrt{\varepsilon_1}+\sqrt{\varepsilon_2}}\right|^2$ the reflection coefficients relative to the surface and subsurface interfaces and ε_1 and ε_2 the dielectric constants (or relative permittivities) of the liquid medium and the seafloor solid material; f_S and f_{SS} are geometrical terms accounting for the scattering losses caused by surface and subsurface roughness; K is the wave attenuation at delay $\Delta\tau$, which is the result of the combined effect of volume scattering and medium absorption.

58

The signal extinction K at depth z inside the medium can be expressed as:

$$[K(z)]_{dB/km} = 1.8 * 10^2 * \sqrt{\varepsilon_1} * \tan\delta(z) * [f_0]_{MHz}$$

but it can be also indicated varying the time delay Δτ:

$$[K(\Delta\tau)]_{dB/\mu s} = 27 * \tan\delta(\Delta\tau) * [f_0]_{MHz}$$

with f_0 the radar signal carrier frequency and $\tan\delta$ that represents the energy dissipation of an electromagnetic field in a lossy medium and it is defined by the ratio between its resistive (lossy) and reactive (lossless) components

$$tan\delta = \frac{\omega\varepsilon'' + \sigma}{\omega\varepsilon'}$$

with $\varepsilon' = \varepsilon_0\varepsilon_r$ and ε'' respectively the real and imaginary parts of permittivity and σ the conductivity.

Roughly speaking, the loss tangent describes how lossy a material is. In example, if σ << ω ε, we have a lossless material (or a bad conductor). Methane, that is a nonpolar dielectric molecule, belongs to this last category and its loss tangent can be written as $tan\delta = \varepsilon''/\varepsilon'$ resulting in a very low value in the order of 10^{-5}.

The determination of the loss tangent from our estimations can be carried out by means of a formula like

$$\left[\frac{P_S}{P_{SS}}(\Delta\tau)\right]_{dB} = A + B * \Delta\tau$$

that can represent the linear relationship of our interest. This relation features the dielectric properties of the liquid, represented by coefficient A (in dB), and the specific attenuation of the media, indicated with B (in dB/μs).

Applying a linear regression of amplitude ratio Ps/Pss vs subsurface depth on the acquired data it is possible to estimate the values of B, angular coefficient of the regression, and A , the y-intercept that takes into account the surface and subsurface reflectivities as well.

Prior to the regression it is important to operate a preliminary selection process. This procedure permits to filter away those bursts featuring the presence of increased seafloor roughness, or the tendency to show lower secondary peaks in the distributions, likely due to the presence of multiple distinct surfaces extending at the seafloor and occurring in the same antenna footprint. Furthermore, selection of data is a common practice in radar sounding analysis and the resulting ambiguities in the retrieval approach are sensibly reduced by choosing unimodal distributions. Results with the relative confidence intervals obtained from such regressions are shown in Figure 22.
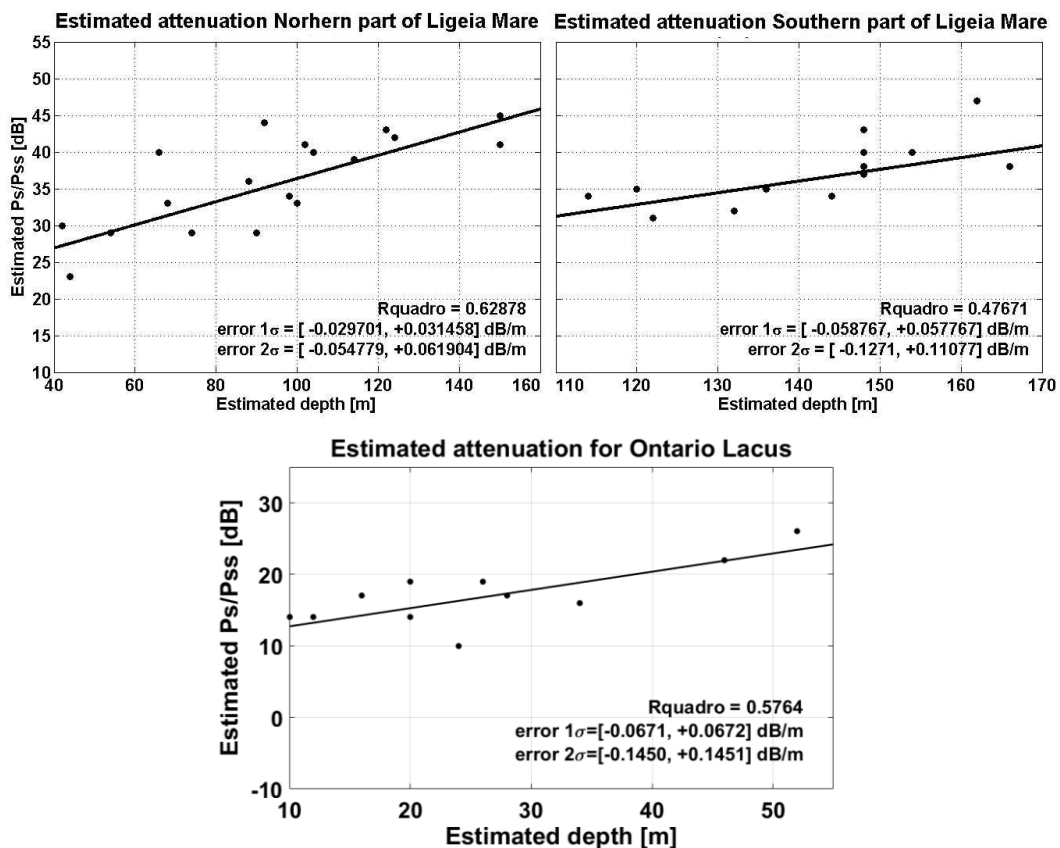
Figure 22: linear regressions for Ligeia Mare and Ontario Lacus. The Rquadro (or Rsquare) term indicates the goodness of the fit and it can take values from 0 (bad fit) to 1 (the variance is perfectly accounted for by the model). Namely, the Rquadro is the square of the correlation between the response values and the predicted response values. The Figure shows also for each graph the 1- and 2-sigma intervals of confidence calculated on the residuals of each fit.

The results that we obtain for B are: 0.14 dB/m for the northern part of Ligeia Mare, 0.145 dB/m for the southern and 0.2 dB/m for Ontario Lacus.

It is possible and appropriate to perform an evaluation of the most probable value for attenuation and its relative associated errors over the selected 13 (North Ligeia), 18 (South Ligeia) and 11 (Ontario) bursts of each dataset in a more reliable way than the simple linear regression. Thus, in order to obtain our three attenuation posteriori distributions, we generate ten thousand possible linear regressions by randomly extracting values from the selected bursts posteriori distributions of depth and Ps/Pss, obtained at the first step of the inversion processing.

At this point, I can obtain the loss tangent $\tan\delta$ by inverting the relation that links it to the attenuation [XXXIV]:

$$\tan\delta = \frac{[B]_{dB/\mu s}}{27\cdot[f_0]_{MHz}}$$

As a result (see Figure 23), for northern and southern regions of Ligeia Mare we obtained respectively B_{North} = 0.14 ±0.03 dB/m (or 16.1 ± 3.5 dB/µs) and B_{South}= 0.145 ±0.05 dB/m (or 16.7 ± 5.7 dB/µs), corresponding to $\tan\delta_{North}$ = 4.3 x10^{-5} ±1.2 x10^{-5} and $\tan\delta_{South}$= 4.5 x10^{-5} ±1.5 x10^{-5}. Furthermore, if we assume the composition of northern and southern regions of Ligeia to be the same, the average loss tangent is 4.4 x10^{-5} ±0.9 x10^{-5}.

The intercepts, on the other hand, result to be A_{North} = 20.57 ±2.57 dB and A_{South} = 13.7 ±7.1 dB.
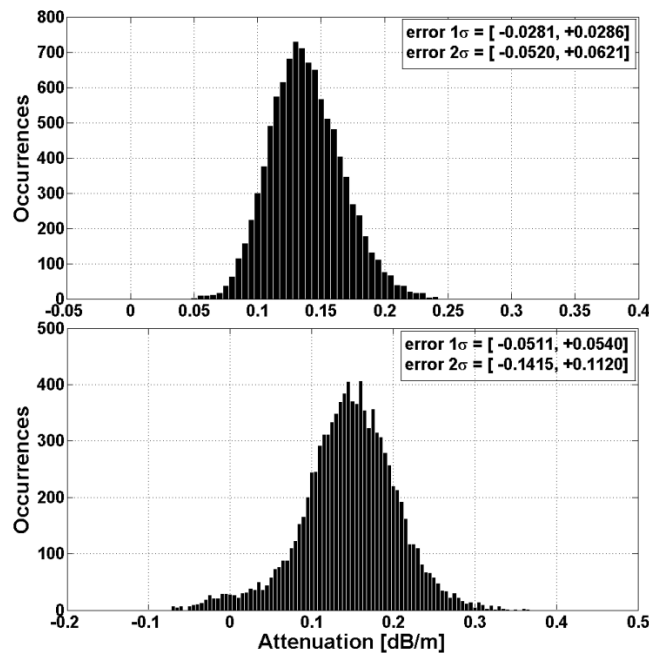
Figure 23: Specific attenuation distribution for the northern (up) and southern (down) regions of Ligeia Mare.

For Ontario Lacus, on the other hand, we obtained B = 22.66 dB/µs ±9.9 dB/m (or 0.2 dB/m ±0.07 dB/m), corresponding to tanδ = 7 x10^{-5} ±3 x10^{-5}. The retrieved intercept is A = 10.18 dB ±1.87 dB.
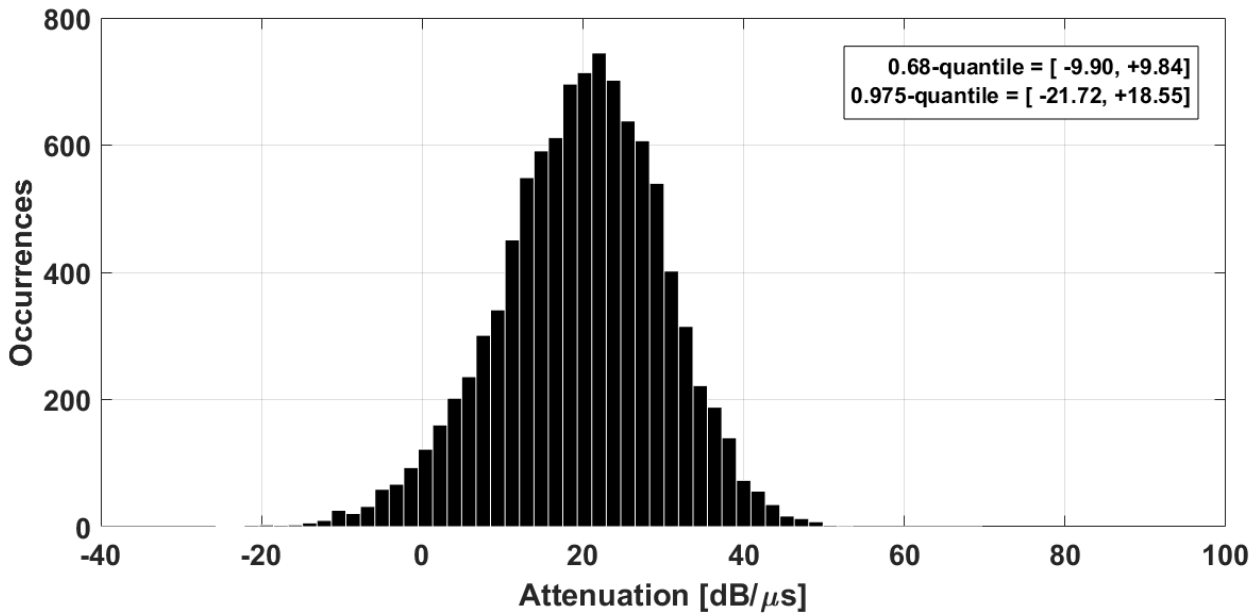
Figure 24: Specific attenuation distribution for Ontario Lacus.

c. Liquid composition

It is likely that the liquid composing the Titan seas and lakes is a ternary mixture of methane, ethane and nitrogen, in facts these are the most abundant materials on Titan that have loss tangents low enough to match our inferred values (see Table 7).

As reported by the measurements done by the Huygens probe, that on January 14, 2005 at 12:43 UTC landed on Titan (see Figure 25) at about 10.2°S, 192.4°W, the surface temperature was about 93.8 K (-179.35 °C / -290.83 °F) and the surface pressure 1.448 atm (1.4676 bar). At these conditions hydrocarbons are liquid and no solid compounds can be characterized by the so low loss tangent we are inferring.

Nitrogen can dissolve in pure ethane and methane [VIII] and its mole fraction in the liquid is determined by the partial pressure (1.5 bars) of nitrogen in contact with the open seas. The solubility of nitrogen has been measured in pure ethane and, in a recent experiment conducted by Malaska et al. (2016), it has been shown that the quantity of dissolved nitrogen may vary with the temperature and composition of the mixture. Namely, slight heating of the seas or additions of pure methane, respectively due to sunlight or rains, can sometimes result in localized nitrogen releases by bubbling. Furthermore, in a recent paper, Mitchell et al. [XXXI] determined the Ku-band microwave absorption coefficient of the mixture to be a combination of its individual components, by using the Lorentz-Lorenz mixing rule and nitrogen solubility in methane-ethane determined by Malaska et al. at 91 K temperature.
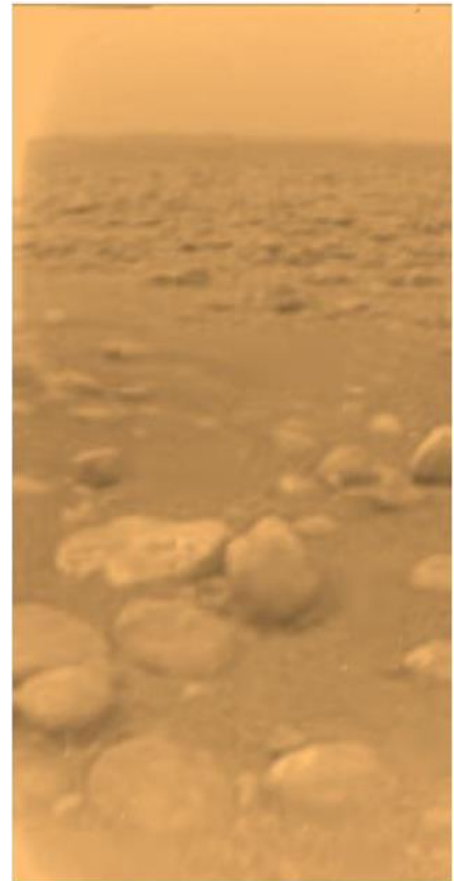
Figure 25: the surface of Titan photographed by the Huygens probe

Category	Material	ε'	ε''	tgδ	note
Atmosphere	Nitrogen, N_2 (98,4 %)	1	0	0	-
	Methane, CH_4 (1,5 %)				
	Others - ethane, acetylene, diacetylene, benzene, various nitriles, various gases such argon and helium (0,1 %)				
Dry land	Water Ice, H_2O	3,15	7.56×10^{-4}	2.4×10^{-4}	RC-13GHz-77K
	Carbon Dioxide Ice, CO_2	1,55	3×10^{-4}	$1,9 \times 10^{-4}$	RC-10GHz-77K
	Compacted Simple organic	2÷2,4	20÷22	8,8÷10,9	RC-10GHz-77K
	Polymers	5÷5.5	0	0	
	Water Ammonia Ice	3.17÷4.38	$(1,8÷4,2) \times 10^{-3}$	$(5,7÷9,6) \times 10^{-5}$	-
	Acetylene Ice	3,12 ?	5×10^{-3} ?	$1,6 \times 10^{-3}$?	-
Seas	Methane, CH_4 (49÷69 %)	1,6	$4,33 \times 10^{-5}$	$2,71 \times 10^{-5}$	RC-14GHz-90K
	Ethane, C_2H_6 (14÷41 %)	1,83	$2,07 \times 10^{-4}$	$1,13 \times 10^{-4}$	RC-14GHz-90K
	Nitrogen, N_2 (10÷17 %)	1,45	2×10^{-4}	$1,4 \times 10^{-4}$	FS-13GHz-77K

Table 7: Dielectric characteristics of the most abundant materials found on Titan. Column 'note' reports info about the method and conditions of the measurements with RC (Resonant cavity method) and FS (Free-space method). These values are found in literature, see [XXXI].

Coupling these laboratory measurements with our estimations of Titan seas liquid attenuation, the resulting best-fit composition for Ligeia Mare is 72% CH_4, 11% C_2H_6, and 16% N_2 mole fraction, or 71% CH_4, 12% C_2H_6, 17% N_2 volumetric, while for Ontario Lacus it is 54% CH_4, 35% C_2H_6, 11% N_2 mole fraction, or 49% CH_4, 41% C_2H_6 and 10% N_2 volumetrically. As a matter of fact, under the same assumptions, Ontario Lacus clearly results more ethane rich than Ligeia Mare.

<div align="center">

CHAPTER V
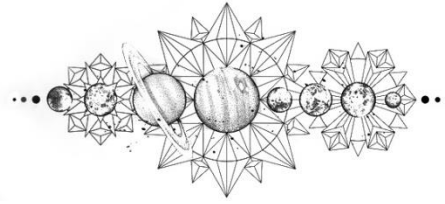
Discussion of the results

</div>

In this chapter I will discuss the obtained results, with the aim of inferring about the characteristics of the Titan liquid bodies here examined.

a. Ligeia Mare: bathymetry, Ps/Pss, subsurface roughness

The results of our depth estimations tell us about a Ligeia Mare that is clearly divided at about 80° of northern latitude in two distinct regions by the presence of a relatively high seafloor feature (see Figure 26). However, this physiografic division is not reflected in the characteristics of the seafloor for the two zones. The Northern Region (NR), in facts, shows posteriori parameters distributions of depth that look very similar respect to the Southern Region (SR). If we compare the average width of the 2σ confidence intervals for the two regions (see Table 8 in this chapter appendix), we find out that we have 41 m for NR and 43.3 m for SR (hereafter I filtered out the three bursts with depths 104, 66 and 124 around 80°N, where clearly the seafloor feature is present). Furthermore, fitting second degree polynomials on the two bathymetries gives similar results in terms of standard deviation of residuals (7.8 m and 8.6 m for NR and SR, respectively), suggesting a similar large scale roughness for the two regions as
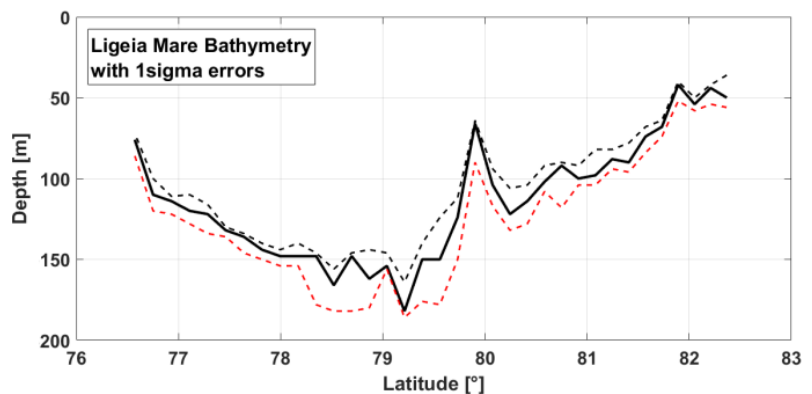

Figure 26: Estimated bathymetry with 1-sigma confidence intervals.

well. This fact is confirmed also on the footprint scale by the average roughness calculated for NR (13 m) and SR (13.7 m) and by the behavior of Ps/Pss ratio that roughly follows the estimated bathymetry and reveals once more a substantial homogeneity in the overall roughness and permittivity of sea surface and seafloor, with the attenuation of the signal that is basically function of the traversed path into the liquid.
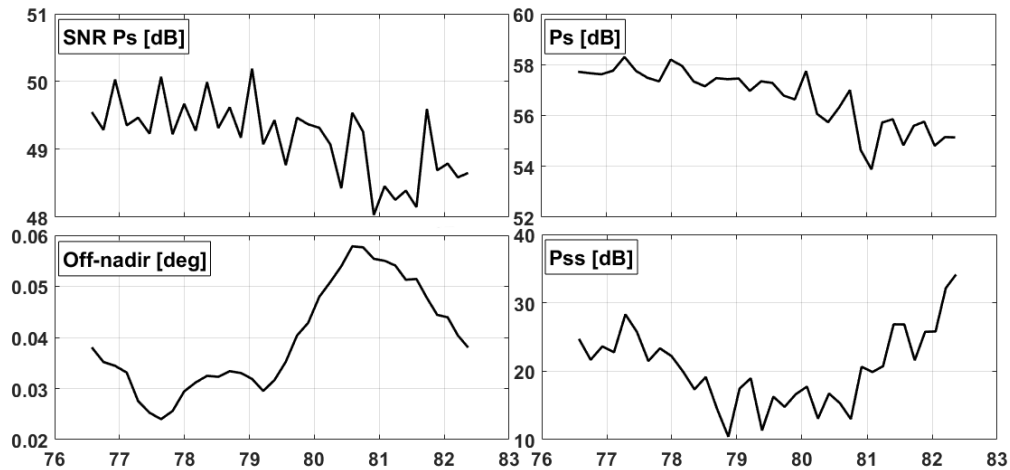
Figure 27: Signal-to-Noise Ratio (SNR); antenna mispointing angle (Off-nadir); uncalibrated signal power recorded for surface (Ps) and seafloor (Pss) echoes acquired over Ligeia Mare during the T91 flyby.

The antenna mispointing angle trend over the Ligeia Mare shows a slight and gradual variation of about one tenth of the antenna beam (0.35°) in the middle of the track, that causes a decrease of about 1 dB in the SNR and 2 dB in the surface signal power (see Figure 27). Moreover, it is interesting to note that the signal power variability over the SR is lower respect to the one of the NR. Standard deviation of linear fitting residuals over the surface signal power gives 0.73 dB and 0.28 dB respectively for the northern and southern regions. This behavior could be attributed to a different state of the sea in the two regions: in particular, to a lower small scale roughness at the SR. Given that the surface signal does not suffer of strong variations in power, the seafloor signal shows a trend that, similarly to what happens for the Ps/Pss ratio, nicely follows the estimated bathymetry. Standard deviation of second degree polynomial fitting residuals over the NR and SR seafloor signal power gives 2.6 dB and 2.9 dB respectively evidencing one more time a substantial homogeneity in the dielectric/roughness characteristics of the Ligeia Mare seafloor.

Let's consider for a moment the region in which the Ligeia Mare is located as it appears in Figure 28 from the I moment T91 altimetry profile. It is possible to note the presence of few interesting geologic features that could be identified as dry lake beds, along the altimetric track at latitudes 56° N, 63° N and 68° N. These three deep (about 180m, 160 m and 130 m) basins appear to be similar in shape to the seafloor of Ligeia Mare, which has been plotted over the altimetric profile in the same figure for convenience. At this point it is simple to understand how the shape of the northern polar area of Titan is the result of the action of the liquids found there, that in the billions years long history of Titan have carved its surface.
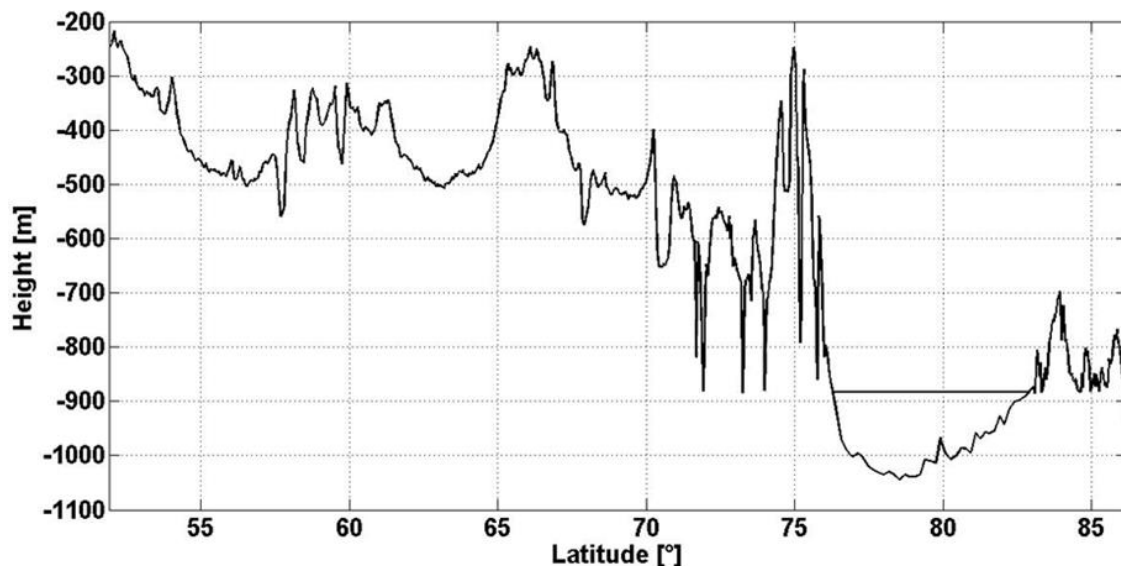
Figure 28: reproc1 T91 inbound I moment altimetry of the Northern Polar Area.

b. Ontario Lacus: bathymetry, Ps/Pss, subsurface roughness

The retrieved depths for Ontario Lacus tells us about a quite shallow lake respect to the hundred meters deep northern seas of Titan. This is compatible with the fact that lacustrine features on Titan are found mostly in the North, where they cover the 11% of the poleward of 55°N observed area (about the 60% of the total). On the other hand, the South region benefits of high resolution images for the same percentage of the total poleward of 55°N area but here only the 0.5% of these territories are liquid-filled.

Aharonson et al. in 2009 described the Titan's southern summer solstice as nearly coincident with Saturn's perihelion and causing a flux of methane and ethane from the South

to the North about 25% higher than what can be found during the northern summer. The net flux of volatiles would eventually slow and reverse with dynamical shift in the orbital parameters with a cycle of about 50k years.

At least four dry broad basins have been suggested to be paleoseas that were filled during an earlier epoch, their names are Ontario, Romo, Rossak and Buzzell. Thus, the Ontario Lacus would be the residue of a recent or ongoing desiccation process causing an increase of less volatile, but more absorbing, compounds such as longer-chain hydrocarbons and/or nitriles. This condition is consistent with the higher loss tangent estimated for Ontario Lacus (7×10^{-5} $\pm 3 \times 10^{-5}$) respect to Ligeia Mare ($4.4 \times 10^{-5} \pm 0.9 \times 10^{-5}$), as well as with the case of an increased content of liquid ethane, that has been spectrally identified by the Visual and Infrared Mapping Spectrometer (VIMS) in 2007 [V].

Another loss tangent estimate for Ontario Lacus has been carried out in 2010 by Hayes et al. [XV] using SAR backscatter and near-shore altimetric slopes: this study, relative to the near-shore areas, resulted in a loss tangent of about 6×10^{-4}. An order of magnitude higher value that is compatible with eventual larger presence in the near-shore suspended particles and, thus, in an increased microwave absorptivity in coastal zones.

Concerning our estimation results (see Figure 29), the average depth is 23.6 m and, if the deepest point along the T91 bathymetric profile of Ligeia Mare was 182 m, here for Ontario Lacus we found a shallower 52 m right in the middle of the track, 1° W Longitude, where a sudden seafloor lowering and increase of the Ps/Pss ratio refers to the presence of some sort of discontinuity in the lake-floor.

Referring to the two burst interested by the deepest point in the lake (depths 52 and 46 m), the west section results in an average depth of 22.8 m, Ps/Pss ratio of 15.8 dB and roughness of 7.3 m, on the other hand the eastern section exhibits 20.9 m, 13.5 dB and 4 m. The results for the two regions are quite similar, thus the surface and lake-floor geometric/dielectric characteristics should be pretty homogeneous like in the Ligeia Mare case.
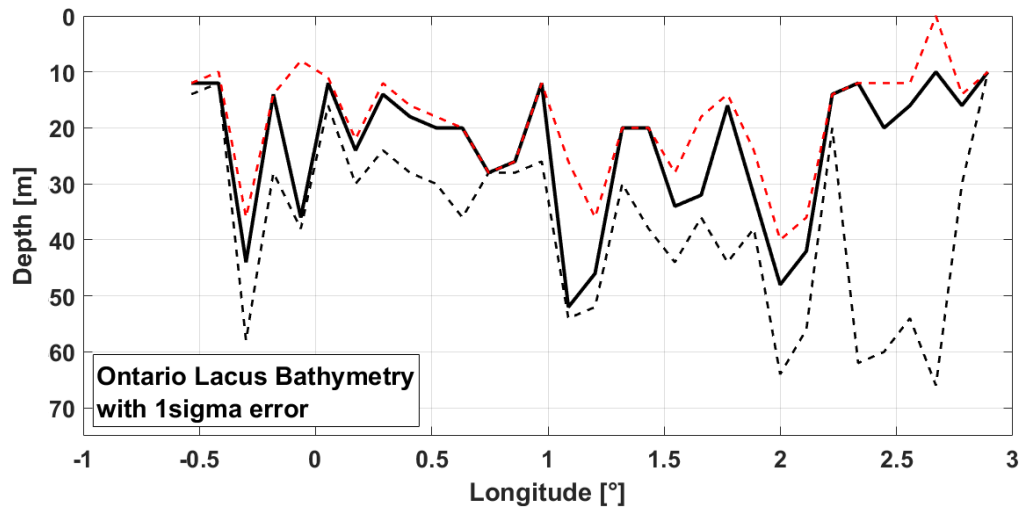
Figure 29: Estimated bathymetry with 1-sigma confidence intervals for Ontario Lacus.

Finally, it is possible to note that if we extend the I moment T49 altimetry profiles into the lake from both east and west directions the herein retrieved depths look quite consistent with their trends.
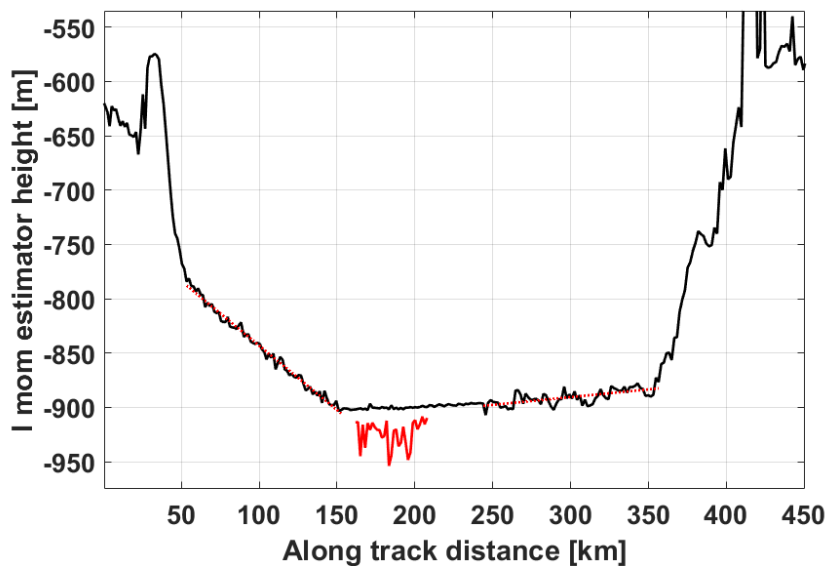
Figure 30: Indicated in red the estimated bathymetry plotted over the I moment altimetry profile. Topographic slopes leading up to Ontario lacus are present on the western coast from 50 to 150 km along track with a value of (1.22 ± 0.03) × 10⁻3, and on the eastern from 250 to 350 km with a value of (1.7 ± 0.6) × 10⁻⁴ [XV].

c. *Punga Mare: preliminary results*

Punga Mare has been repeatedly imaged in high resolution by the Cassini RADAR in SAR mode, notably during T19 (Oct. 9, 2006), T29 (Apr. 26, 2007) and T64 (Dec. 28, 2009). Despite this, we will not have a total high resolution coverage of its surface at the end of mission as the northern and western coasts have been imaged only with low resolution infrared, optical and HiSAR mode.
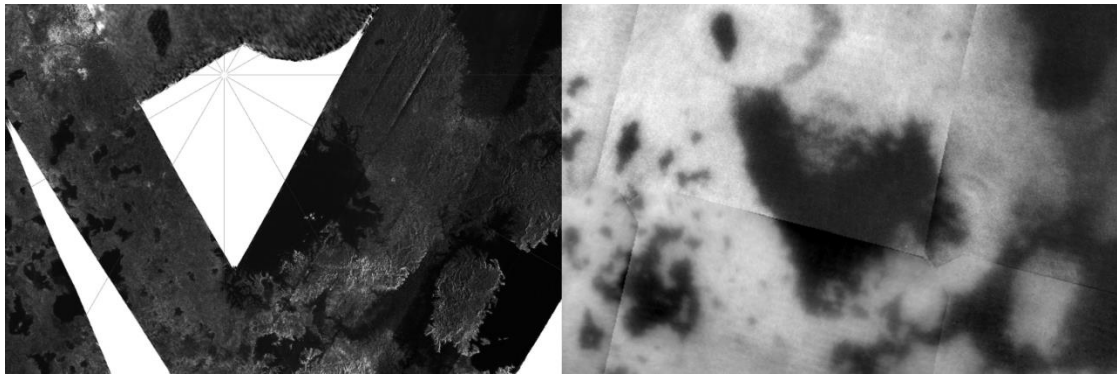
Figure 31: Punga Mare in SAR images mosaic (left) and in optic images (right).

Punga Mare is located close to the North Pole of Titan (85°N, 342.1°W) and with its diameter of about 340 km (NE-SW) it is the third sea for areal extension (6.1×104 km^2 [XIII]) after Kraken and Ligeia Mare.

After the scientific achievements obtained from the analysis the Cassini radar altimeter data for Ligeia Mare and Ontario Lacus, on January 11, 2015 the Punga Mare has been observed in altimetry mode during the flyby T108 in order to allow a quantitative investigation of seafloor depth and shape, as well as of the loss tangent of the liquid.

Previous specific studies have been conducted by Grima et al. [2016] and Barnes et al. [2014].

The first of these works exploits the Cassini radar altimeter dataset acquired during the T108 flyby and by means of the application of a technique called Radar Statistical Reconnaissance (RSR) it estimates surface RMS height σ_h of Punga Mare as varying from 2.3 (methane dominant liquid) to 2.5 mm (ethane dominant liquid), correlation length l_c ranging from 30 to 36 mm and effective slope ($s_e = \sigma_h/l_c$) from 3.6 to 4.9. Comparing Punga Mare values with the results obtained for the other seas, comes clearly out that this sea of Titan is somewhat rougher than Ligeia and Kraken

Mare, in particular they show that its surface is characterized by a σ_h similar to the one estimated over Kraken Mare but with an significantly lower l_c.

The second study is based on the analysis of the VIMS dataset acquired during flyby T85 on July 24, 2012 and showing this mare has been characterized by isolated patches of increased roughness with typical slopes up to 6° ± 1° and significant wave heights of 2^{+2}_{-1}cm [Barnes et al., 2014].

In Figure 32 it is shown (left panel) the outbound altimetry acquired during fly by T108 of Punga Mare, herein the half power footprint walk across the marine surface of southern Punga Mare for about 200 km (from ~650 to ~850 km along track). It is possible to note that altimetry profiles obtained by means threshold, centroid and maximum likelihood estimators show the presence of two pretty smooth areas preceded and followed by abrupt changes in topography in the order of hundreds of meters. The first one of them, that extends from ~300 to ~500 km along track, is relative to a system of channels and flooded areas which provides connection between Punga and Kraken Mare.

Available SAR images of the Punga Mare surface show the clear presence of a radar brighter feature in the middle of the sea, in correspondence about of the kilometer number 735 of the altimetric track. This is consistent with the presence of an island, part of which the radar altimeter could have observed. The strong specular reflection received therein is, however, indicative of an high percentage of the footprint illuminating the smooth liquid surface of the sea.
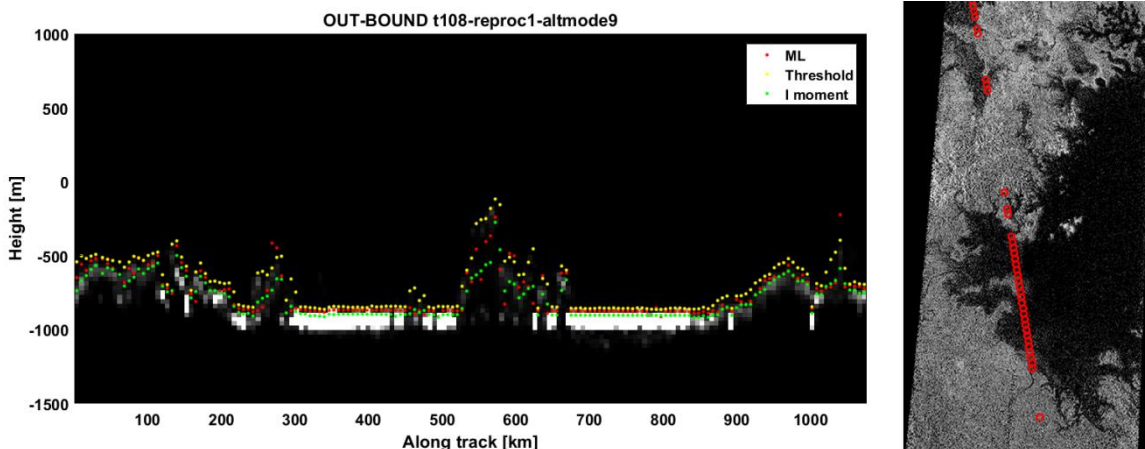
Figure 32: In the left panel the reproc1 T108 outbound I moment altimetry profile over the Punga Mare area. In the right panel the T29 flyby SAR image of the area with superimposed the T108 footprints for which specular reflection occurred.

Like in the case of Ligeia Mare, the T108 radargram (see Figure 33) clearly shows the presence of a secondary echo coming from the seafloor that can be easily tracked and gives a maximum depth of 142 m (refractive index = 1.32).

The preliminary retrieved values of depth and Ps/Pss ratio are compatible with a very low attenuation that points to a composition of the liquid that, similarly to Ligeia Mare, should be extremely methane dominated.
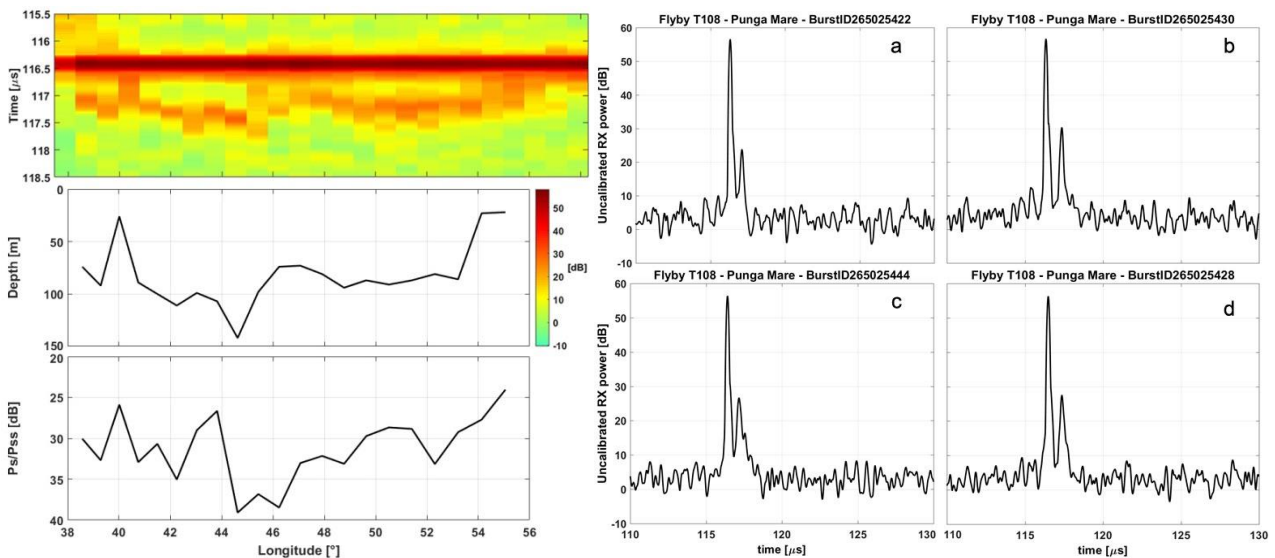
Figure 33: In the left panel the T108 flyby radargram over Punga Mare and the preliminary results of tracking the seafloor peak. In the right panel are shown four echoes processed with Blackman tapering and x4 Burg superresolution. Panels a, b, c and d show echoes with respectively a depth of 89 m, 115 m, 86 m and 99 m.

Directly connected to Punga Mare there are two liquid-filled channels that have been observed by the radar altimeter with two footprints located at 900 and 1000 km along track. The time distance measurements between the peaks relative to the liquid surface and the echo reflected from the surrounding areas indicates depths of 126 m, for feature 'a', and 193 m, for feature 'b' (see Figure 33). These values are indicated with a precision of about the Cassini radar range resolution (~35 m).

For what concerns the level of the liquid filling the canyons, the preliminary measurements show that for feature 'a' the level is about the same of the nearby sea. On the other hand, for feature 'b' we have that the surface of the liquid is placed 13.7 m over the sea, indicated with a precision of about 0.6 m. Indeed, assuming a flat Punga Mare sea and referring to the geoid model of Titan [XVIII], the standard deviation of the retrieved sea levels is 0.58 m (2-sigma).

72

Figure 33: left panel shows a comparison between the two echoes over the canyons and an echo received from Punga Mare as a mean sea level reference (see the black dotted line). The T29 SAR image shown in the right panels presents a detail of the areas interested by the presence of the two canyons with the footprints 'a' and 'b' overplotted together with a red dotted line highlining the track of the 'b' canyon.

d. Chapter five appendix

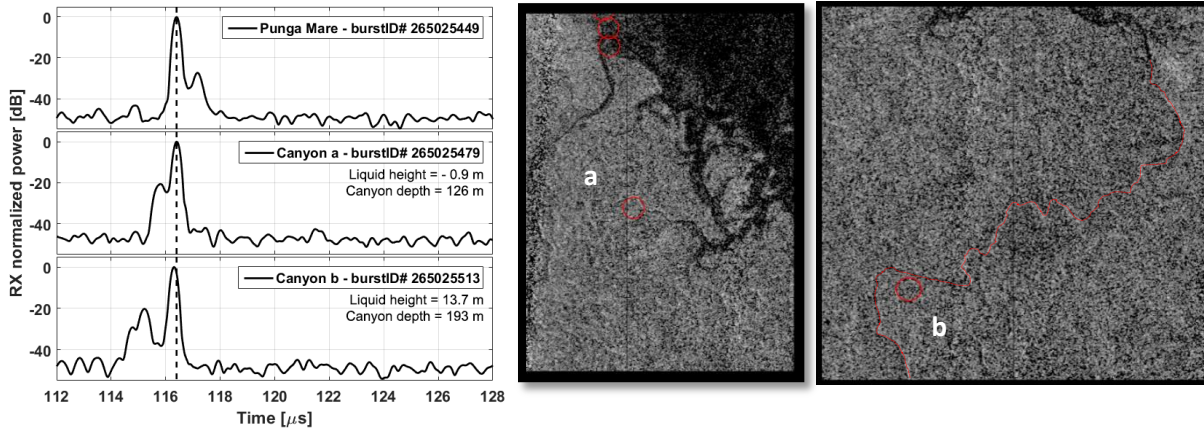| Latitude (°)	W Longitude (°)	Depth (m)	1σ down (m)	1σ up (m)	PsPss (dB)	1σ down (dB)	1σ up (dB)	Roughness (m)	1σ down (m)	1σ up (m)
82,37	242,31	50	-24	10	21	-6	6	10	-8	4
82,21	242,27	44	-10	14	23	-5	8	10	-6	2
82,05	242,23	54	-10	6	29	-5	5	10	-8	4
81,89	242,18	42	-6	16	30	-5	5	8	-8	4
81,73	242,15	68	-12	14	33	-4	5	14	-14	4
81,57	242,11	74	-14	20	29	-5	4	16	-6	4
81,41	242,08	90	-20	16	29	-4	5	18	-8	6
81,25	242,04	88	-14	16	36	-4	6	10	-10	12
81,08	242,00	98	-24	16	34	-4	6	20	-12	6
80,92	241,98	100	-16	14	33	-3	5	8	-6	16
80,75	241,94	92	-12	80	44	-5	6	14	-14	18
80,58	241,90	102	-16	20	41	-4	8	2	-2	24
80,41	241,84	114	-20	44	39	-5	5	22	-20	14
80,25	241,79	122	-36	54	43	-6	6	20	-20	14
80,08	241,73	104	-16	28	40	-5	5	20	-18	10
79,90	241,68	66	-12	98	40	-4	10	12	-12	14
79,73	241,63	124	-36	56	42	-3	8	22	-22	16
79,56	241,58	150	-38	38	41	-5	8	30	-30	12
79,39	241,52	150	-30	38	45	-7	5	18	-18	22
79,21	241,48	182	-36	8	38	-4	7	30	-26	14
79,04	241,43	154	-20	24	40	-4	10	0	0	34
78,87	241,38	162	-68	26	47	-7	3	0	0	42
78,70	241,36	148	-22	40	43	-5	7	0	0	42
78,52	241,33	166	-22	24	38	-3	7	22	-18	20
78,35	241,31	148	-12	40	40	-6	6	28	-28	14
78,17	241,28	148	-16	16	38	-5	5	14	-12	20
78,00	241,26	148	-10	12	37	-5	4	6	-6	20
77,82	241,24	144	-10	14	34	-3	6	8	-8	20
77,64	241,22	136	-8	18	35	-4	6	4	-4	26
77,46	241,19	132	-8	14	32	-3	6	2	-2	22
77,29	241,17	122	-12	26	31	-3	4	22	-18	12
77,11	241,15	120	-18	20	35	-4	4	20	-14	12
76,93	241,12	114	-8	16	34	-4	4	8	-8	18
76,75	241,10	110	-18	22	36	-4	5	22	-18	8
76,57	241,08	76	-10	18	33	-4	5	12	-8	8

Table 8: Estimated values and relative 2-sigma confidence intervals obtained for Ligeia Mare useful for inferring about the characteristics of the seafloor.

CHAPTER VI
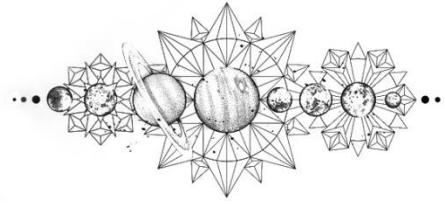
LIQUID-FILLED CANYONS ON TITAN

In May 2013 the Cassini RADAR altimeter observed channels in Vid Flumina, a drainage network connected to Titan's second largest hydrocarbon sea, Ligeia Mare. Analysis of these altimeter echoes shows that the channels are located in deep (up to ~570 m), steep-sided, canyons and have strong specular surface reflections that indicate they are currently liquid filled. Elevations of the liquid in these channels are at the same level as Ligeia Mare to within a vertical precision of about 0.7 m, consistent with the interpretation of drowned river valleys. Specular reflections are also observed in lower order tributaries elevated above the level of Ligeia Mare, consistent with drainage feeding into the main channel system.

a. Introduction

Saturn's largest moon, Titan, has an active methane-based hydrologic cycle [XXVI] that drives the formation and evolution of morphologic features and processes with striking similarities to those found on Earth [XIII]. Titan's north polar region is partially covered by three large hydrocarbon seas (in order of areal extension Kraken, Ligeia and Punga Mare) that have been observed by the Cassini RADAR [IX] using its synthetic aperture radar (SAR) mode (Fig.34, Left Panel).

Prior analysis of radar altimeter mode data acquired in May 2013 (T91 flyby) revealed reflections from both the seabed and sea surface. *Mastrogiuseppe et al.* [XXVIII] used the time difference between these reflections to measure depths up to 160 meters along the altimetry track. The relative returned power between the surface and subsurface reflections was used to

estimate the liquid loss tangent, the low value of which implies a methane-dominated composition [XXVII].

As formerly predicted by *Lorenz* [XXII], *Ori et al.* [XXXIII] and others, in addition to seas and lakes, Titan also has networks of fluvial valleys and channels that extend for hundreds of kilometers across the surface at all latitudes [*XXV*, VI]. The most prominent examples are in the north polar region, where 90% of the surficial liquids are located. Herein, we report an analysis of altimetry echoes acquired from Vid Flumina (Fig.34, right panel), a network of channels that drain into Ligeia Mare.

Even though SAR images reveal the presence of sinuous radar-dark features interpreted as fluvial valleys (e.g., [VI]), they do not directly prove the physical extent and/or presence of liquid filling them. Such features display a variety of forms and characteristics quite similar to our terrestrial examples [VI] and due to their low microwave backscatter, it has been assumed that they are liquid filled like the seas, yet no direct measurement has ever been made to demonstrate such a claim.

Herein, we use Cassini Ku-band (λ = 2.17cm) radar altimeter nadir observations to directly detect the presence of liquid in Titan's north polar channels and characterize their width and geomorphologic context. Altimeter returns from the Vid Flumina channels are highly specular and the measured steep increases in backscatter with respect to the surroundings require surfaces roughness on the millimeter scale over the ~250 m diameter of the Fresnel zone (see below). Similar to *Wye et al.* [LI], *Zebker et al.* [LIII] and *Mastrogiuseppe et al.* [XXVIII], we interpret these smoothness constraints are requiring liquid surfaces. This represents the first direct detection of liquid-filled channels on Titan.

Furthermore, channels exhibit canyon-like morphology, with the liquid surface elevations of the higher order tributaries of the Vid Flumina network (herein we will refer to the Strahler stream order) occurring at the same elevation as Ligeia Mare. We also find lower order tributaries with liquid surface elevations above the level of Ligeia Mare, consistent with elevated tributary networks feeding into the main channel system.
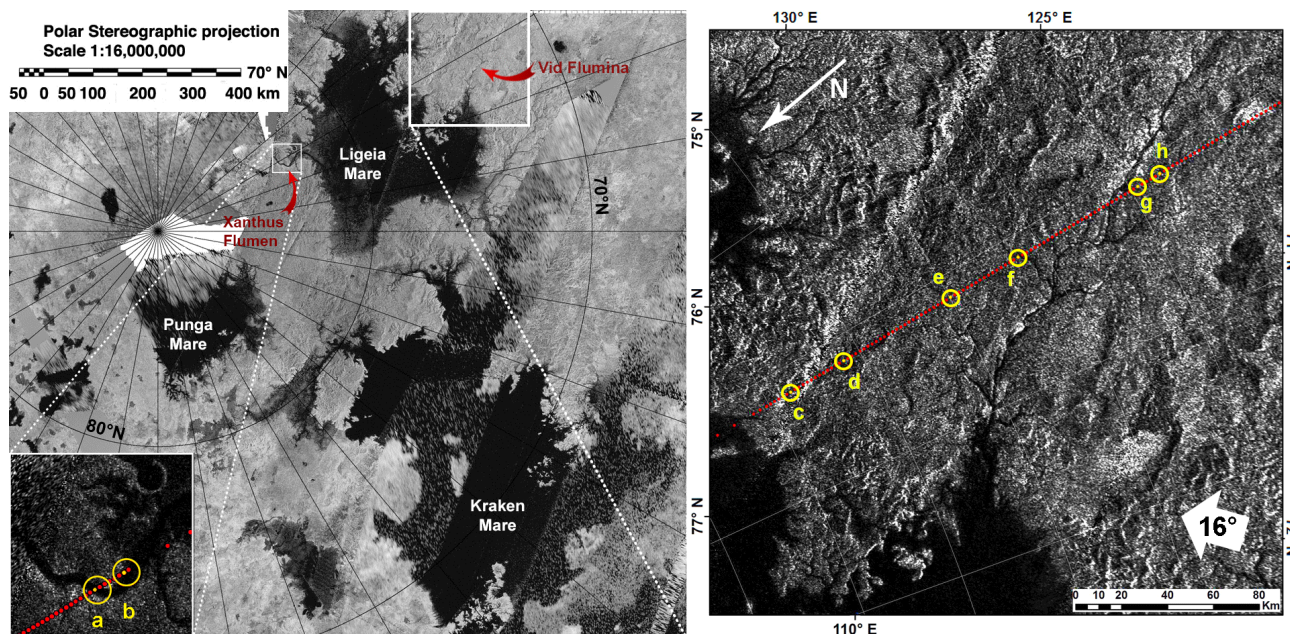
Figure 34: The Northern polar area of Titan and Vid Flumina drainage basin. *Left Panel*. On top of the image, the Ligeia Mare; in the lower-right the North Kraken Mare; the two seas are connected each other by a labyrinth of channels. On the left, near the North pole, the Punga Mare. Red arrows indicate the position of the the two flumina significant for this work. At the end of its mission (Sept. 15, 2017) the Cassini RADAR in its imaging mode (SAR+HiSAR) will have covered a total area of 67% of the surface of Titan [XIII]. Map credits: R. L. Kirk. *Right Panel*. Highlighted in yellow are the half power altimetric footprints within the Vid Flumina drainage basin and the Xanthus Flumen course for which specular reflections occurred. At 1400 km of spacecraft altitude, the Cassini antenna 0.35 degree central beam produces footprints of about 8,5 km in diameter (diameter of yellow circles). It is easy to note that we don't have a specular reflection at each intersection of the altimetric track with the channels. This is mainly due to the very limited area covered by the Fresnel zone (~250 m) and to the 0.6 s of the Burst Repetition Interval (BRI) of the radar. The result is that in some cases the Fresnel zone just missed the strong reflection from the liquid coming from nadiral direction.

b. *Radar Observations of Channels*

Vid Flumina is classified as a dendritic network whose links span for total length of 412 km [VI]. Its drainage basin has been imaged several times by SAR (notably on flybys T28, T86 and T92), where it appears as a branching, sinuous, radar-dark feature that terminates at the shoreline of Ligeia Mare. The very low backscatter may be indicative of the presence of a smooth surface, absorptive materials, or a shadowing effect. This SAR-dark appearance contrasts with many of Titan's equatorial channels, which instead appear radar-bright [XXV, XXI]. In such cases, the brightness of the channels could indicate dry river beds with coarse gravel and/or strongly retroreflective cobbles [XXI]. The May 2013 T91 altimeter track, which crossed a number of Vid Flumina's channels, provides an opportunity to understand this scattering difference by combining SAR images with closest-approach altimetry observations.

The morphological similarities of Titan's dark patches shown in SAR images with terrestrial lakes, their location in topographic depressions, and the presence of branching valley networks along the seas shorelines has been used to suggest that these features are liquid-filled [XLIII, XIV, LI]. Furthermore, the exceptionally strong reflection from altimetry returns with sub-radar point that falls onto these radar-dark patches requires exceptional flatness of < 2.7 mm (= $\lambda/8$, according to the Rayleigh Criterion) root mean square (RMS) height and is a strong indication of the liquid nature of these features. In fact, reflections are specular when received from a smooth plane reflector and comply with the Fresnel reflection laws. In these cases, the backscattered signal, composed by both coherent and incoherent power, is mainly dominated by the coherent component and the resulting fraction of total incident power specularly reflected is equal to $e^{-2(2\pi\sigma_h/\lambda)^2}$ [XL]. It is also interesting to note that Cassini has observed liquid-filled channels previously – strong near-nadir radar echoes observed during Cassini's flyby of Earth were determined [XXIV] to be due to the dammed Paranaiba River in Brazil.

When a specular reflection occurs, the transmitted signal is reflected by the Fresnel zone, an area that is located at nadir when observing a liquid surface and whose diameter is always smaller than a few hundred meters at the operative altitudes of the Cassini radar altimeter. See also *Grima et al.* [XI], that exploited these concepts for determining surface roughness on Mars. In 2014, *Zebker et al.* [LIII] provided estimates regarding the surface flatness of Ligeia Mare, indicating RMS height values of roughness σ_h ranging from 0.5 to 1.5 mm over the Fresnel zone. Contributions coming from scatterers composing these extremely flat surfaces add coherently and yield the raw signal to assume unexpected strong amplitudes that occasionally caused the Cassini RADAR receiver saturation [LI].

In order to show the liquid nature of the Vid Flumina channels we compare the backscattering values (σ_0) obtained by the Cassini radar altimeter for the T91 flyby with those pertaining to all solid surfaces of Titan. The exploited dataset consists of all altimetric observations from Ta to T98, covering roughly 10 years of the Cassini mission and excluding all observations of Ontario Lacus (T49), Ligeia Mare (T91), small lakes of T92/T95 and putative tropical lakes of T98. As a result, Vid Flumina channels are characterized by σ_0 values (~30 dB) that no solid surface of Titan, observed to date by the altimeter, has been capable to produce (see Figure 35).
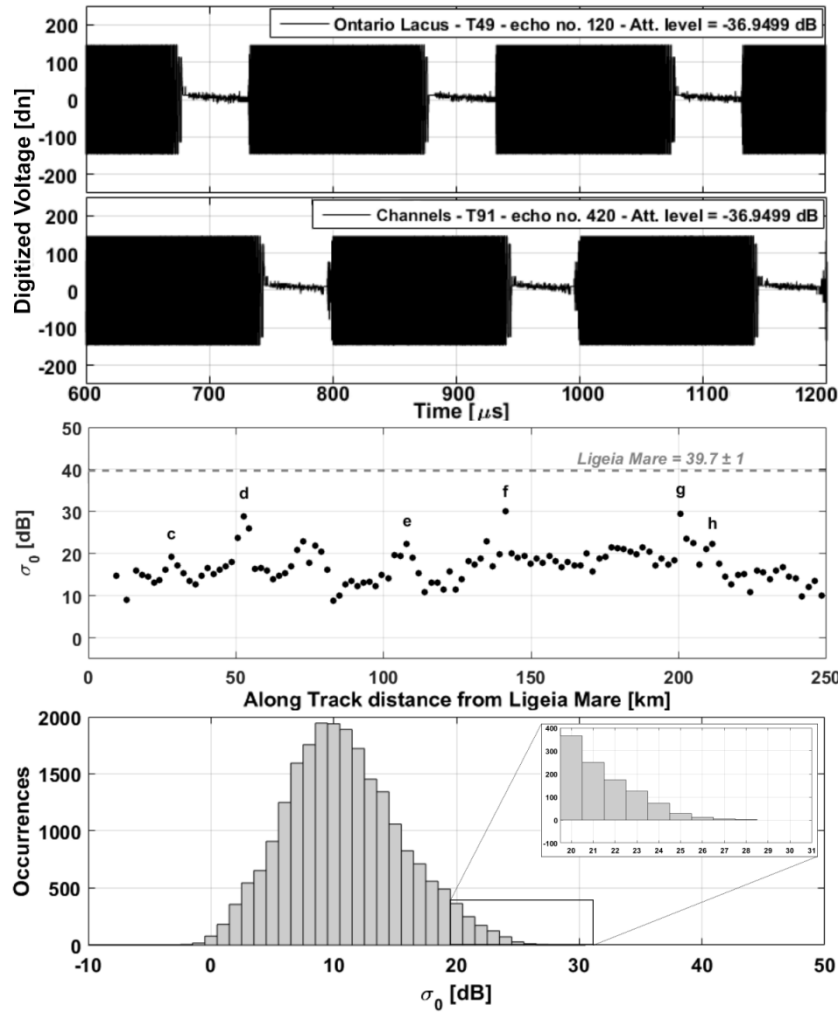
Figure 35: Saturated bursts over Ontario Lacus and channels, backscattering values retrieved over the Vid Flumina area and over all the solid surfaces of Titan from the Cassini radar altimeter. *Upper panel*. **Comparison between two bursts of chirped signals (burst no. 120 or burstID 177011373 and burst no. 420 or burstID 248037064) received from Ontario lacus and Vid Flumina respectively. Note that they result clipped at ±148.5 dV due to the strong level of saturation;** *Middle panel*. **Backscattering levels retrieved from altimetry observations of the Vid Flumina area. Features 'd', 'f' and 'g' pertain to channels observations for which saturation occurred and exhibit values of ~30 dB. The gray dotted line represents the mean sigma-nought value retrieved for Ligeia Mare. Standard deviation indicated in the associated label;** *Lower panel*. **Histogram showing sigma-nought values retrieved from the Cassini radar altimeter dataset including flybys from Ta (Oct 2004) to T98 (Feb 2014) and ruling out all the observations over liquid surfaces. Mean value is 10.8 dB with a standard deviation of 4.7 dB. Note the total absence of backscattering values higher than ~28 dB.**

c. Measurements and results

We selected eight bursts along the T91 altimetric track, two north of Ligeia Mare and six to the south (Figure 34), that are marked from "a" to "h". Mean surface height estimations useful for outlining the topographic profile are obtained by tracking the centroid of the observed power distribution, as described by the first moment of the altimetry echo with respect to time [LII]. The

78

resulting profile is characterized by significant decreases of hundreds of meters (Figure 36, Middle Panel), to which correspond strong enhancements in the level of received power (Figure 36, Upper Panel).
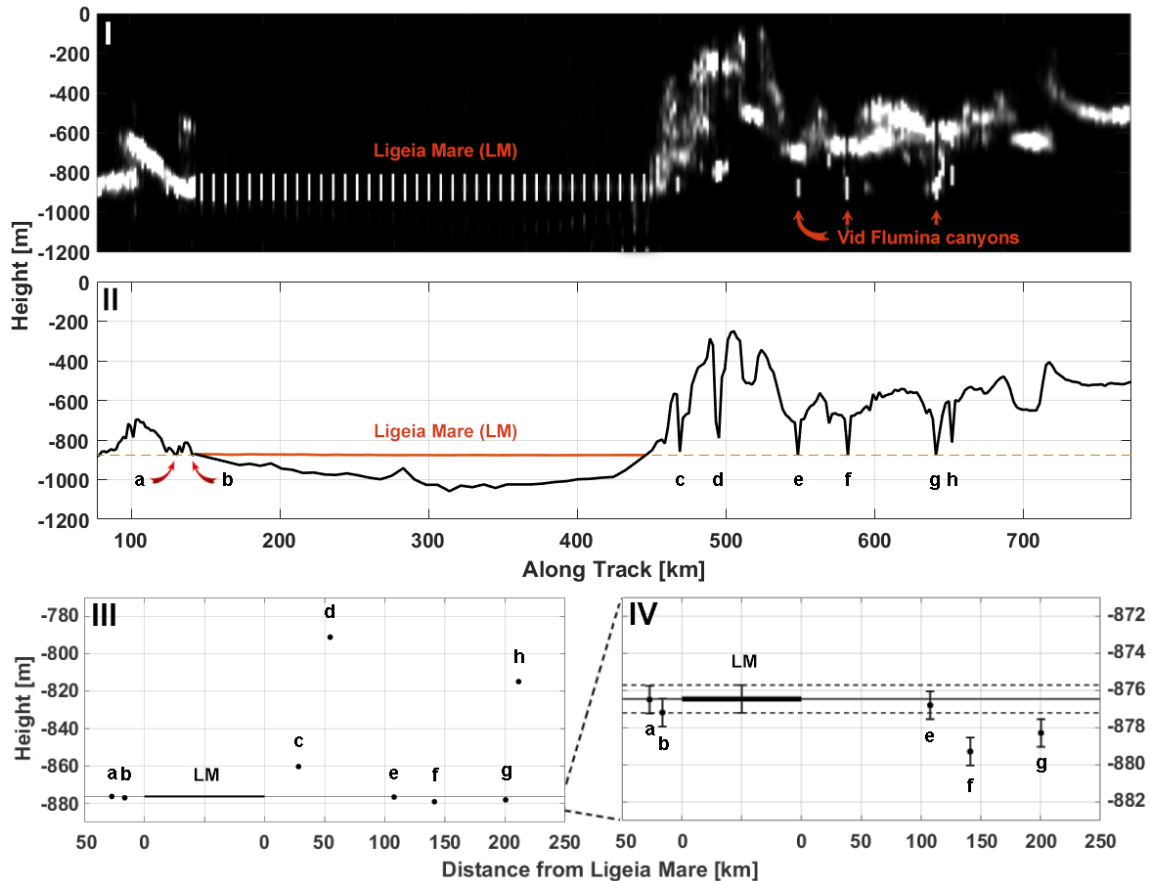

Figure 36: Radargram and results. *Panel I.* **Each column of the radargram represents an incoherently averaged echo received during the T91 flyby from the region hosting Ligeia Mare and channels. Pixel intensity indicates the received backscatter as function of time. The surface of Ligeia Mare results dotted because of the peculiar design of the T91 flyby, which consisted in an alternated acquisition of echoes from a nadir and a slight off-nadir antenna pointing geometry. Arrows indicate specular reflections from the main trunk (feature "g") of Vid Flumina and from two of its tributary branches (features "e" and "f").** *Panel II.* **Titan's heights given by the Cassini Processing of Altimetric Data (CPAD) are reported as relative to a 2575 km sphere, centered at Titan's center of mass. Observations featuring specular reflections from the liquid are indicated with progressive letters from North to South; the position of Ligeia Mare can be recognized by the extremely flat region extending from about 140 to 440 km along track; Vid Flumina hydrographic basin interests an area ranging from about 440 to 680 km along track. The altimetry profile shown here is useful to give an idea of the geomorphologic shape of the area and highlines the relative flatness of the surface, whose greatest elevation difference between higher and lower points is about 630 m. This profile has been produced by means of a centroid tracker, that is a leading edge estimator based on the Offset Centre of Gravity (OCOG) algorithm. In particular, we used the I moment tracker, that sets the altimetric echo 2-way travel time by computing the centroid of the observed power distribution, as described by the first moment of the echo with respect to time. For all the echoes relative to channels, the centroid has been computed only on that portion of the signal reflected from the liquid.** *Panel III.* **Channels level and relative distance from the sea along the T91 altimetric track. Measurements have been provided with an error bar indicating a 2σ precision of ~0.7 m (see the Appendix of this chapter for further details). The mean Ligeia Mare level is at -876.5 m. This panel shows a coarse detail altimetry of the levels of the liquids filling the channels.** *Panel IV.* **This panel shows a more detailed altimetry spanning in a reduced range of heights around the sea-level. Note that the features that stand about at the same level of the sea, in this more detailed figure are placed in a range of heights from 0 to 2.8 m below the mean sea level (see the Appendix of this chapter for further details).**

79

Among these eight observations, the -3dB antenna footprints relative to features "e", "f" and "g" are perhaps the most interesting because they illuminate areas crossed by two tributary branches of Vid Flumina ("e" and "f") and by its main trunk ("g"). The elevation profile of the regions comprising these specular reflections shows the presence of deep and tight valleys that range in depth from 220 to 330 m with respect to the surrounding terrain and less than a kilometer in lateral extent (see below). The associated specular reflections, as we have seen, suggest that the bottom of these canyon-like features are very smooth with respect to the Cassini RADAR incident wavelength, a typical characteristic of altimeter returns from Titan's liquid bodies. Considering the high values of backscatter recorded on the channels (above any solid surface of Titan), we determine the elevation of the floor of these channels with respect to the surface of Ligeia Mare in order to infer the process that led to the formation of such features and, at the same time, investigate possible hydraulic connections between Vid Flumina channels and the sea that SAR images clearly would suggest ("e", "f" and "g").

First, we examine specific shape of the received altimetric waveforms (Figure 37, Right Panels). Targeted radar signal simulations (an example of which is also represented in Figure 37) have explicitly shown that saturated echoes from canyon floors, including specular reflections, are expressed as three-peaked waveforms. With reference to the arrival time, the first reflection is attributed to the canyon rim and surrounding topography. The second and most powerful peak of the triplet is perfectly symmetrical in shape at -6 dB and is identifiable as the reflection returning from the flat liquid surface at the bottom of the canyon. We interpreted the third peak, as a post-cursor echo or 'ghost echo', which is an effect that has been observed in terrestrial data by *Wingham and Rapley* [XLIX] using the Seasat altimeter. This artifact is the result of instrument saturation, and has been studied by *Mastrogiuseppe et al.* [XXVII] using data acquired over Ontario Lacus (T49) and Ligeia Mare (T91) along with radar data simulations. Simulations have been able to reproduce saturation effects, including also distortions introduced by the Cassini RADAR's 8-bit Analog-to-Digital Converter and the 4-bit Block Adaptive Quantizator (BAQ). In both *Wingham and Rapley* [XLIX] and *Mastrogiuseppe et al.* [XXVII], finally, it is shown that the range measurement of well-defined pre- and post-cursors is unaffected. Regarding the Vid Flumina waveforms, the first and third peaks are precisely symmetric in time with respect to the echo received from the liquid channel. As such, our interpretation of the data from both the SAR images and individual altimetric waveforms is a scenario where there are two main reflectors, one associated with the

smooth liquid surface at the canyon bottom, and another that corresponds to the elevated, surrounding terrain adjacent to the canyon (Figure 37, Left Panel).
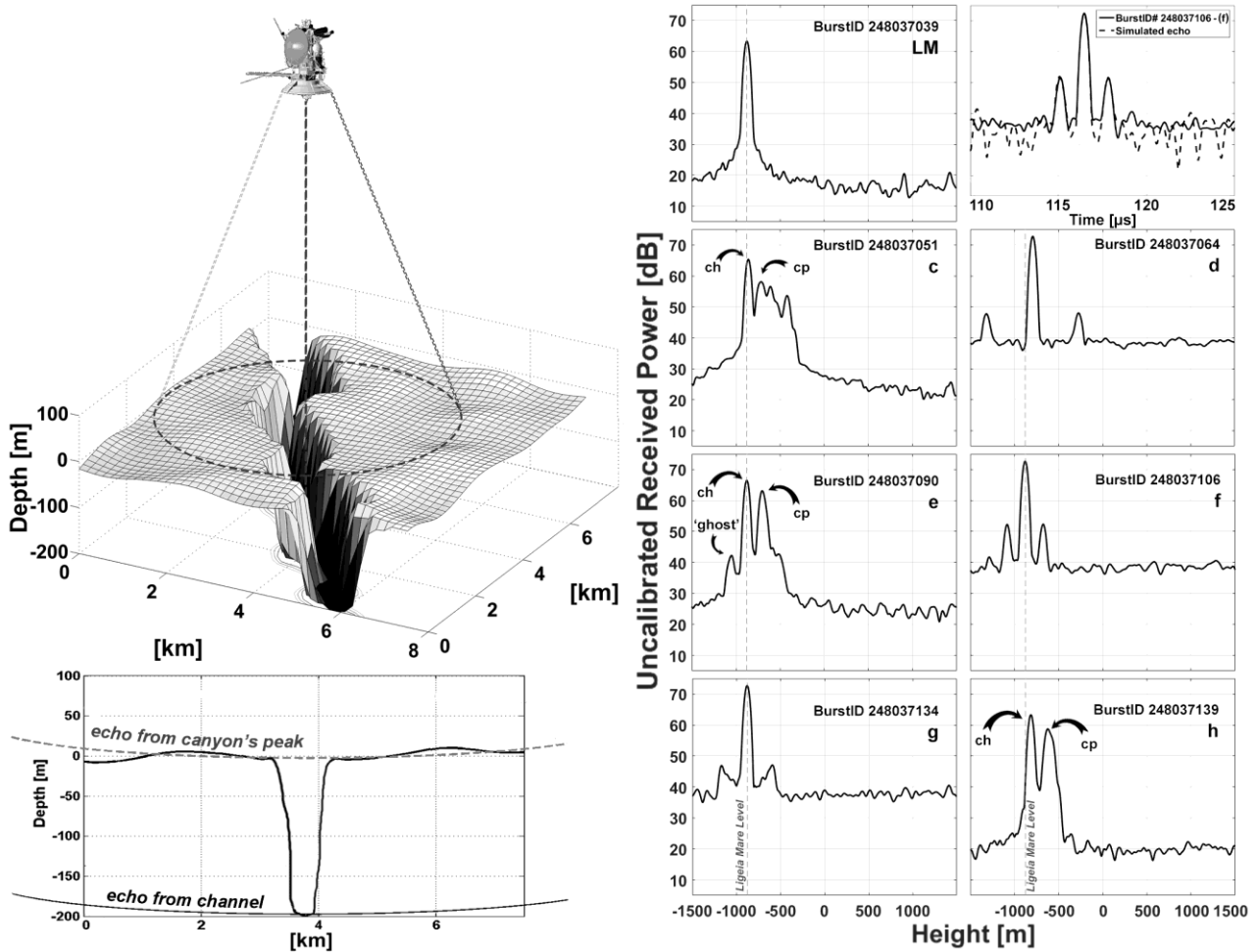

Figure 37: Acquisition scenario and echoes received from Vid Flumina canyons. *Left panels.* Simplified scheme of Cassini radar altimeter observing a canyon. The nadir looking antenna receives first the echo from the overlying surface, then it receives the strong reflection from the smooth liquid surface of the channel at the bottom of the canyon. *Right panels.* Cassini altimetric time series acquired during fly-by T91 over the Vid Flumina canyons. Blackman taper function and incoherent averaging were used to process the received echoes. The echo indicated as "LM" (*upper-left panel*) is one of those acquired on Ligeia Mare and it is used here as a reference to indicate the sea-level (see the dotted gray line). Received echoes (from "c" to "h") are characterized by a first echo from the canyon's peak (or "cp"), a second one from the liquid channel (or "ch") and a third (named "ghost"). The "ghost signal" is an artifact due to saturation occurring in the Cassini RADAR receiver. This post-cursor is located in a time-symmetric position respect to the echo associated to the reflection from the peak of the canyon. In the case of echo "c" the isolation of the specific peak relative to the canyon edge has been possible thanks to a range-Doppler analysis. In the *upper-right panel* a comparison between the echo received from the canyon located at feature "f" and a simulated echo. The simulator makes use of a SAR image of the area comprising the canyon of interest for generating the most likely scenario, that is therefore represented by means of the facet method [VII] as a Brownian surface of dimensions larger than the -3 dB footprint scale. Hagfors model is adopted in order to retrieve scattering from each facet relative to surroundings and walls of the canyon [XII]. Finally, we modelled the flat liquid surface of channel as a single scatterer located at nadir characterized by radar cross-section described by Picardi et al. [XXXVII]. In order to obtain the simulated echo shown in figure we set depth of the canyon according to the depth measured for feature "f" (243 m) and a RMS height of macroscale surface roughness of 18 m for the area surrounding the canyon. As a result it is possible to appreciate the simulation ability to reproduce signal post-cursors due to the strong saturation of channels altimetric observations.

Because of the uncertainty in spacecraft orbit tracking, the absolute elevations determined in different Cassini flybys may have relative errors of about 100-200 m [XLII]. However, for the purposes of this study we exclusively consider the T91 flyby; uncertainties along a single track are much smaller. We find that, to within a ~0.7 m precision (2σ, see Appendix of this chapter), all the echoes received from Vid Flumina's main trunk and tributary branches (in particular "e", "f" and "g") are found to be at the same level as the sea surface, even though they are located in a wide range of horizontal distances from Ligeia Mare (Figure 36, Lower Panels). For all the echoes relative to channels, the centroid has been computed only on that portion of the signal reflected from the liquid. Since the scattering is almost fully coherent, the obtained waveform resembles the radar impulse response and we are able to apply a time window, which selects that interval included between the -10 dB points with respect to the peak.

The measurement of the time interval between the first two echoes is a direct measure of the depth of the canyons. In particular, we measure the time delay from the leading edge of the first echo (-6 dB from the peak) to the peak of the second echo associated to the liquid. In this way, we obtain an estimate of the mean level of the area illuminated by the altimetric footprint. The precision of the depth measurements of these canyons is mainly dependent on the signal to noise ratio (SNR) of the signal reflected from the surface at the cliff's edge and on the large-scale vertical roughness of this surface itself. Thus, it can be inferred to be in the same order of the radar range resolution (35 m, see the Appendix of this chapter). See Table 1 for the reported measurements of all canyon depths.

Using T28 flyby SAR images, and following the method described in detail in the Appendix of this chapter, we have been able to measure the width of the two sections of Vid Flumina comprising features "f" (a first order tributary) and "g" (main trunk). In these two sections, respectively centered around footprints "f" and "g", the width that we measure for both ranges roughly from 0 to 1 km, with a mean value of 0.7 km. The abrupt changes in backscattering (up to 10 dB) between the dark spots pertaining to the channel course and the surrounding terrains testifies the great steepness characterizing the Vid Flumina canyons walls. Given the measured canyon's depths respectively of about 240 and 330 m for features "f" and "g" we can infer mean slopes >40 deg for their walls.

In an attempt to confirm canyon widths obtained by means of the SAR images analysis, we applied the advanced altimetry data processing technique described in detail by *Michalides et al.* [XXX],

who used it to enhance along-track resolution for May 2007 (T30) altimetry observations and measure the profile of empty lake basins on Titan. Iso-Doppler regions, extending within the area illuminated by the altimetric pulse, are limited across track by the antenna beamwidth (~8.5 km) but span along-track for only ~1 km. However, due to the narrow nature of these canyon mouths and/or their non-optimal orientation relative to the ground track direction (indicated with a dotted red line in Fig. 34, Right Panel), the improved along track resolution was not enough to confirm the measured widths of Vid Flumina canyons by means of the radar altimeter.

Concerning echoes 'c' and 'd', these are isolated reflections from regions with no clear fluvial features present or resolved in any of the SAR images (whose resolution in general varies from 350 m to over 1 km). However, the basin-shaped topographic profile, so similar to the other fluvial features here analyzed, and the strong backscattering enhancement recorded with respect to the surrounding terrains (especially in 'd', where saturation occurred) lead us to conclude that there are fluids and sub-SAR resolution hydrologic features in these locations. Furthermore, from the topographic profile, feature 'd' is incised about 570 meters, representing the deepest canyon observed along the T91 altimetry track. For observations "c", "d" and "h" the levels of liquid are higher in elevation with respect to the sea. They stand 16.1 m ("c"), 85.5 m ("d") and 61.7 m ("h") above it. In particular, the footprint "h" illuminates an area that is surrounded Vid's main trunk (~10 km away) and a secondary branch of the river (~7.4 km away). Also, in this case SAR images show that the presence of a single liquid body with dimensions of several hundreds of meters is not likely, but the presence of higher order tributaries occurring several tens of meters above the level of Ligeia Mare could be consistent with drainage feeding into the Vid main channel system.

Finally, observations "a" and "b" pertain to Xanthus Flumen, flowing into Puget Sinus, an arm of the northern part of Ligeia Mare. They are located where the last meander of the channel goes around an 80 m elevated area (with respect to the sea level) and then opens to the sea (see lower-left panel of Figure 34). Combining SAR images with altimeter echoes, and adopting the same method used for determining channels width at features "f" and "g", it is possible to measure width also at these locations. We have a mean width of 2.8 km at feature "a" and 7.3 km at feature "b". A deeper analysis did not reveal the presence of any additional topographic feature, such as raised riverbanks, and the liquid level of both channels was indistinguishable from the elevation of the nearby sea surface.

d. Discussion

This paper reports the detection of liquid-floored canyons in the northern polar area of Titan, with the dataset acquired by the Cassini RADAR altimeter during the T91 fly-by of Titan. The altimeter footprint illuminated two systems of channels connected to Ligeia Mare: we have two observations of Xanthus Flumen close to its mouth and three of the Vid Flumina in the middle of its course. The level of the liquid filling their main trunk and tributary branches stands at the sea level regardless to their distance from the shoreline (hundreds of kilometers). Three more isolated observations attest to the presence of surface liquids standing at higher elevations (tens of meters) and feeding into Vid's drainage basin. From the shape of the received echoes we determined the difference in height between the level of the liquid filling the channels and the surrounding terrains (hundreds of meters). Finally, by considering the width of the channels as shown by the available SAR images (less than a kilometer) we concluded that these features can be recognized as canyons characterized by steep wall slopes (greater than 40°).

While topographic profiles of the observed fluvial valleys are comparable to glacially eroded fjords on Earth, we rule out any glacial formation mechanisms. This is because the presence of any large-scale ices, such are alpine glaciers, on the surface are thermodynamically improbable on Titan [XXIII].

The presence of deeply entrenched channels indicates periods of prolonged incision into an erosionally-weak material. The degree of erosional incision suggests a protracted period of erosion, although erosion rates and hence duration remain to be constrained. In order to drive the incision vertically into the terrain, liquid elevations of the seas must have been lower in the geologic past to drive the potential for flow and transport of sediment. Alternatively, if sea level remained constant, tectonic uplift of the surrounding terrains would cause the river to incise vertically (e.g. *Kirkby* [XIX]; *Willgoose et al.* [XLVIII]), forming a morphologically similar terrain. If formed primarily by sea level variations, then there must have still been sufficient precipitation and channelized flow throughout the periods of lower baselevels in order to drive landscape evolution and canyon formation.

Subsequent baselevel rise within the north polar regions (e.g. *Hayes et al.* [XVI]; *Hayes et al.* [XIII]) would then result in a backwater effect of the main branches of the Vid Flumina drainage network, and result in liquid elevations equivalent to those of Ligeia Mare. The surrounding tributaries

84

would not be affected by the backwater, resulting in them having the higher liquid elevations that we observe. If they are hydraulically connected, then this would be direct evidence of active flow in Titan rivers.

While a contribution from tectonic uplift cannot be neglected on Titan, we favor a model where the variation in the surface elevation of liquids has driven the formation of the canyons. This is supported by previous observations of drowned river valleys at channel termini in the north (*Stofan et al.* [XLIII]; *Hayes et al*. [XVI]; *Hayes et al.* [XIII]). Likely, however, both tectonics and sea level variations contribute to the formation of the topographic features that we observe, though to what degree remains unconstrained.

The case of variable sea elevations driving canyon formation, followed by a resurgent, or rising, sea level has numerous counterparts on Earth. Examples include Lake Powell, a reservoir on the Colorado river that was created by the Glen Canyon Dam (see Figure 38); the Georges River in New South Wales, Australia; and the Nile River gorge, which formed as the Mediterranean Sea dried up during the late Miocene (*Ryan* [XXXIX]). Rising liquid levels in the geologically recent past led to the flooding of these valleys, with morphologies similar to those observed at Vid Flumina.

Our study reports the first direct detection and characterization of liquid-filled canyons on Titan. Understanding the processes that led to the formation of such hydrological features will be crucial in understanding the evolution and the present state of Titan's geomorphology. Regardless, any model of polar landscape evolution on Titan needs to explain the generation of such greatly incised, hundred-meter deep canyons that drain into the Mare.

Future work will extend our methodologies to all the other channels observed by the Cassini radar altimeter on Titan. Furthermore, modeling the altimeter waveforms [XXIX] can make use of a random-walk Monte Carlo approach able to retrieve the best-fit model parameters describing geometrical properties of Titan's canyons [XXVII].
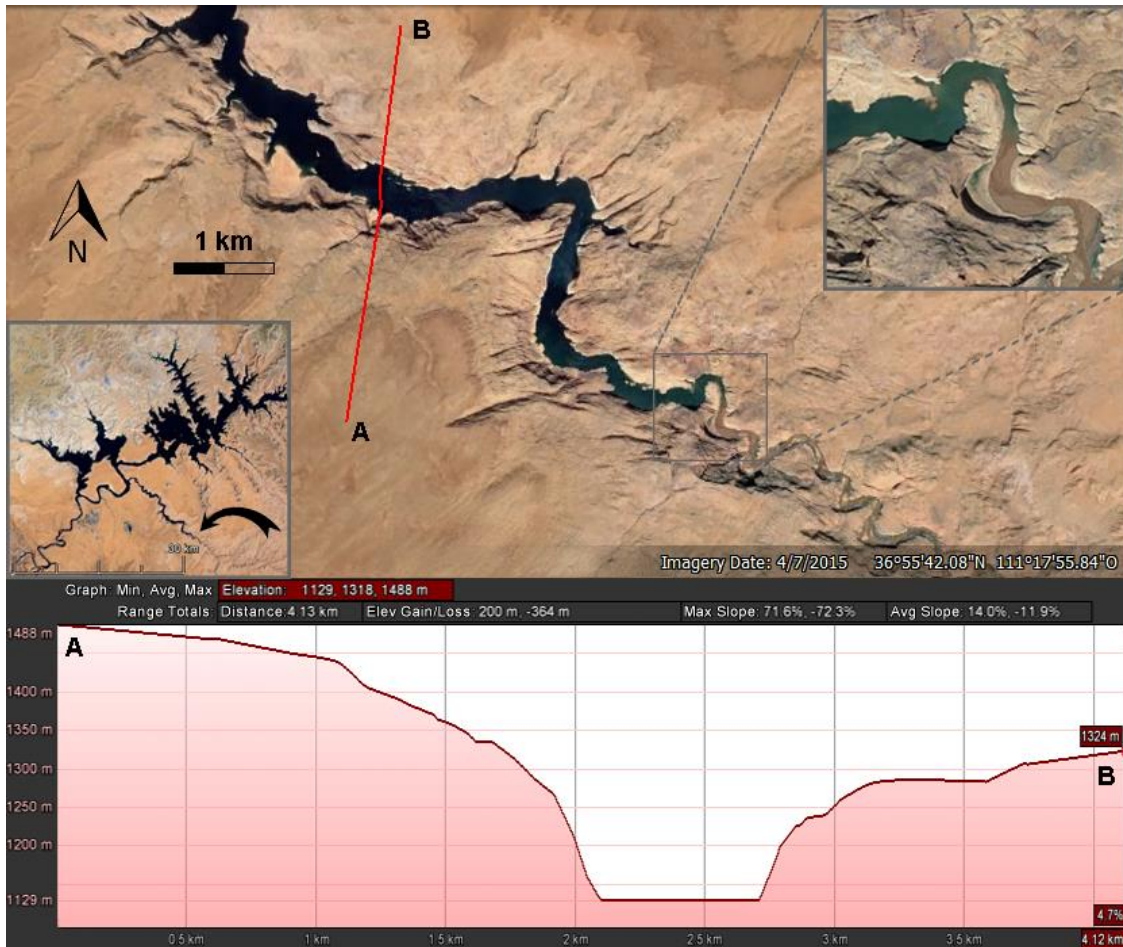
Figure 38: The Lake Powell in Utah (AZ), a terrestrial example. The flooded Navajo Canyon in Lake Powell. This 4 km long altimetric profile shows the width at the base of the canyon is 600 m, the difference between the highest and lowest point is about 360 m, the difference between the mean and lowest point is about 200 m, the maximum slope is about 36°. In the upper-right panel is shown the clear boundary between solid surface and the water.

Feature	Fly-by	BurstID	Lat [deg]	Lon [deg]	Altitude [km]	Off-nadir [deg]	Saturation [%]	SNR [dB]	σ_0 [dB]	Sea distance [km]	Canyon depth [m]	Liquid level [m]
a	T91	248036839	83,32	117,18	1793,01	0,0259	61	35,12	27,94	27	-	-876.5
b	T91	248036845	83,08	117,30	1780,55	0,0239	59	35,38	27,50	16		-877.2
c	T91	248037051	75,76	240,98	1458,22	0,0349	0	43,11	19,13	28	171	-860.4
d	T91	248037064	75,17	240,92	1437,09	0,0338	60	35,23	28,89	55	572	-791.0
e	T91	248037090	73,99	240,80	1395,97	0,0431	0	40,83	22,29	108	221	-876.8
f	T91	248037106	73,24	240,74	1371,44	0,0353	56	35,34	30,05	141	243	-879.3
g	T91	248037134	71,92	240,63	1330,03	0,0426	54	36,11	29,47	201	330	-878.3
h	T91	248037139	71,68	240,62	1322,80	0,0421	0	44,70	22,22	211	263	-814.8
LIGEIA MARE	T91	248036949/ 37039	80	248	1546	0.0316	0	48,81	39,67	-	-	-876.5

Table 9: Saturation has been evaluated by taking into account the number of clipped amplitude samples of the returning chirped signal respect to its whole length. The SNR has been recorded at the peak of the reflection from the liquid, relatively to the noise level. The distance from the sea is intended along the sub-satellite track. Liquid levels are given with a 2σ precision of about 0.7 m. Canyons depths are given by measuring the time delay from the leading edge of the echo reflected from the top of the canyon (-6 dB from the peak) to the peak of the echo associated to the liquid level and, thus, with a precision of the same order of magnitude of the Cassini RADAR range resolution (35 m). For Ligeia Mare averaged values acquired on the southern part of the sea are presented. For the two returns ("a" and "b") associated to the Xanthus Flumen, range-Doppler analysis showed that a canyon scenario for these riverbanks is not applicable.

86

e. Appendix

e.1   Precision of Retrieved Level of Liquids

The theoretical precision of retrieved elevations can be expressed using the Cramer-Rao limit, and is mainly dependent on the signal to noise ratio (SNR) of the received signal and radar bandwidth: $\Delta r = c/(2\beta\sqrt{2SNR})$, where c is the speed of light and β the 4.25 MHz bandwidth of the transmitted chirped signals. This formula clearly indicates potential sub-meter precisions for high values of SNR obtained during rivers and seas observations (i. e., ~38 dB on average for channels, see Table 1). Concerning the southern Ligeia Mare altimetric observations, we obtained the values of the sea-level by tracking the peak of the interpolated echoes, that have been realigned by means of the centroid estimator. Assuming a flat sea by referring to the geoid model of Titan [XVIII], the standard deviation of the retrieved sea levels is about 0.37 m. This value is very near the Cramer-Rao bound of the altimeter and we will use it as our 1σ precision in the estimation of the level of the liquid filling the channels. Nevertheless, in this paper we preferred to indicate our measurements with a 2σ of precision (about ±0.7 m, 95% confidence interval), allowing clear distinction between normal random error in the measurements from causal variation (see Figure 39 and Table 9). It should be clear that such reported precision is related to the standard processing algorithm used for realigning the echoes. This processing is based on the use of the centroid estimator, very sensitive to slight echo broadenings caused by off-nadir antenna pointing angles (Zebker et al. [LII]; Mastrogiuseppe [XXIX]). However, the average value of antenna pointing deviation from nadir over the sea is of the same order of the ones reported for channels observations (see Table 9). Thus, in both cases the centroid of the echo is tracked with about the same slight delay (corresponding to only about 0.3 m at the spacecraft altitude of 1400 km over Vid channels). These considerations show that the off-nadir angles reported for the T91 flyby, anyway very small, do not worsen appreciably the level of precision in the determination of liquid levels. Thus, the precision in the retrieved level of liquids should not be higher than the previously indicated value of about 0.7 m.
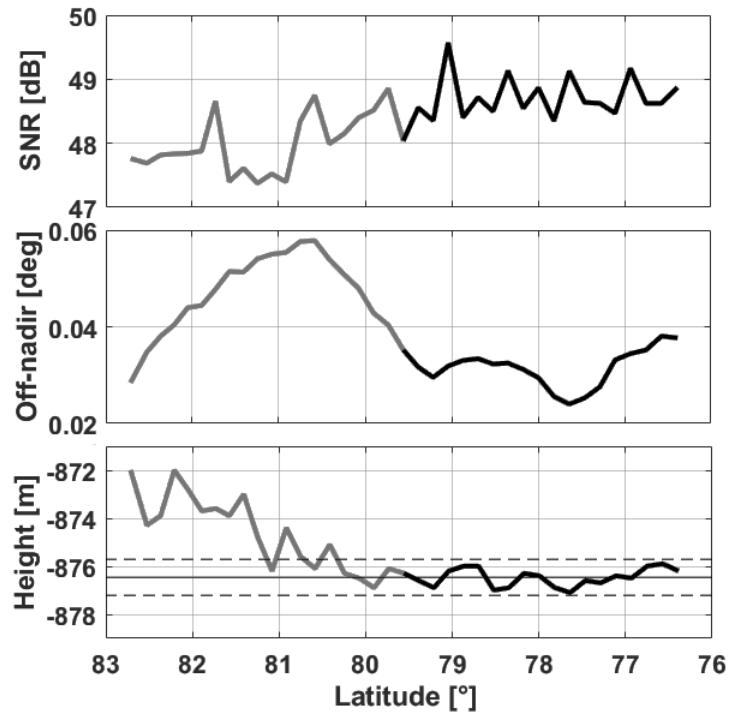
Figure 39: Signal to noise ratio, off-nadir and I moment altimetry recorded on the Ligeia Mare sea surface during fly-by T91. *Upper panel*. Signal-to-noise ratio (SNR) characterizing the altimetric echoes received from the surface of Ligeia Mare; *Middle panel*. Antenna mispointing angles reported for the central antenna beam during the T91 Ligeia Mare observation; *Lower panel*. Ligeia Mare sea-levels obtained by means of the altimeter data standard processing, which makes use of the centroid tracker for realigning the received echoes. Black line indicates the southern part of the Ligeia Mare that we selected in order to determine the mean sea-level (-876.5 ± 0.7 m). This area is in fact characterized by the smallest off-nadir angles (< 0.04 deg) and the higher SNRs.

e.2   *Precision of Retrieved Depths of Canyons*

Cassini RADAR altimeter precision in spacecraft altitude determination over solid terrain is mainly dependent on the signal to noise ratio (SNR), but different height estimation methods are characterized by different sensibilities to the observed solid surface's roughness. Exploiting the Cassini radar altimeter signal simulator developed for Titan's dunes height retrieval described in Mastrogiuseppe et al. [XXIX], where the surface is computed by means of a facet method, we are currently carrying out a campaign of simulations whose preliminary results show that the most precise height estimation method is the one adopted by the Threshold tracker. This method guarantees precisions ranging from ±20 to ±47 m (1σ) over synthetic surfaces with varying height standard deviation from 10 to 40 m at the typically high values of SNR recorded by the radar altimeter (~30 dB). On the other hand, simulations are showing also how the Maximum Likelihood

Estimator (MLE) results to be the more accurate estimator for rough surfaces, giving accuracies in spacecraft altitude determination ranging from +9 to +21 m over the same range of RMS heights previously described. Thus, absolute precision in the canyons depths measurements can be reasonably inferred to be in the same order of magnitude of the Cassini RADAR range resolution (35 m).

e.3 *On the Liquid nature of channels*

During flybys T49 (December 2008) and T91 (May 2013) the Cassini RADAR altimeter received strong reflections from the smooth liquid surfaces of Ontario Lacus, Ligeia Mare, Xanthus Flumen and Vid Flumina. The unexpected high power of the reflection combined with the consequent inadequate choice of the attenuator level during observations of Ontario and the two channels, caused saturation at the receiver and introduction of a time varying DC off-set on the received signal, that is function of amplitude level input to Analog to Digital Converter (Wye et al. [LI]; Mastrogiuseppe et al. [XXVII]). The most evident effect of saturation can be observed in upper right panel of Figure 2S, where some chirped signals clipped at ±148.5 dn received from Ontario and Vid Flumina are shown. Fortunately, this is not the case of Ligeia Mare, for which we are able to retrieve the actual power of the received signal and thus the mean backscatter associated to the liquid surface of this liquid body (~40 dB). This represents an important term of comparison since the values of backscatter associated to the saturated observations of channels are of ~30 dB (see middle panel of Fig. 35) like in the saturated observations of Ontario Lacus surface. Analyzing the whole Cassini radar altimeter dataset from Ta (Oct 2004) to T98 (Feb 2014) flybys it is possible to note that there is no solid surface on Titan that can show backscatter values as high as ~30 dB (see lower panel of Figure 35). If we moreover consider that due to saturation the backscatter value of ~30 dB is very likely underestimated, we can conclude that reflections received from channels result specular and characterized by a level of backscatter denoting their liquid nature.

e.4   *Measuring canyon's width by means of SAR images*

Exploiting the SAR images pertaining to the fly-by T28 we measured the width of channels on two sections of Vid Flumina: the first one relative to a first order tributary (feature "f") and a second one covering the main trunk of Vid Flumina (feature "g"). Referring to Figure 40, it is possible to note the parallelism between the direction of look of the T28 SAR image and the axis of the channel on the feature "f" area that should reduce eventual shadowing effects. On the other hand for feature "g" zone we have an about perpendicular acquisition that makes it possible errors of identification between pixels relative to the liquid surface of the channel and the shadows of the canyon itself.

In order to carry out the measurement of the channels width we had to constrain the range of variation of Normalized Radar Cross Section (NRCS) over their liquid surface. As a reference we considered an area of the Ligeia Mare of several hundred square kilometers in the Nicoya Sinus (the gulf into which the Vid Flumina drains) achieving a useful backscattering statistic for a liquid surface. Using the T28 SAR image, the mean value acquired is therefore of -16.5 dB, with standard deviation of about 2 dB.

RADAR images show the course of the channel as displaying a wide range of backscatter values. Some sections indeed, are characterized by SAR pixels exhibiting the negative clipping value of -20 dB, while others display very low contrast respect to the surrounding terrains. Furthermore, measuring channels width requires choosing a threshold backscatter, that is necessary for distinguish between pixels relative to the channel course and the surrounding solid terrains. We found that the best compromise is represented by a range of values of 3σ around to the average value of backscatter recorded on the sea (in practice $\sigma_0 \leq -10.6$ dB). As a matter of fact this range resulted the minimum exploitable in order to preserve the channels visibility.

The lower-left panel of Figure 40 shows results obtained from channel width measurements over the zone pertaining to the feature "f". Along this ~12 km long stretch, width ranges roughly from 0.1 to 1 km, with a mean value of 0.7 km. The other measurements that have been carried out on the feature "g" area have given, on the ~20 km long section of the channel under analysis, a mean width and a range of values of the same order of those found for the feature "f" channel section

(except for a short enlargement in the middle of the selected track, during which the width arrives to ~4 km).

For what concerns the canyon's walls slope determination, it is worth noting that SAR images show very often backscattering variations higher than 10 dB between adjacent groups of pixels pertaining to the channels dark spots and surrounding terrains. This is consistent with very steep slopes charactering these canyons walls. Considering that for features "f" and "g" respectively we measured a canyon's depths of about 240 and 330 m we can infer for their walls a mean slope >40 and >55 deg.
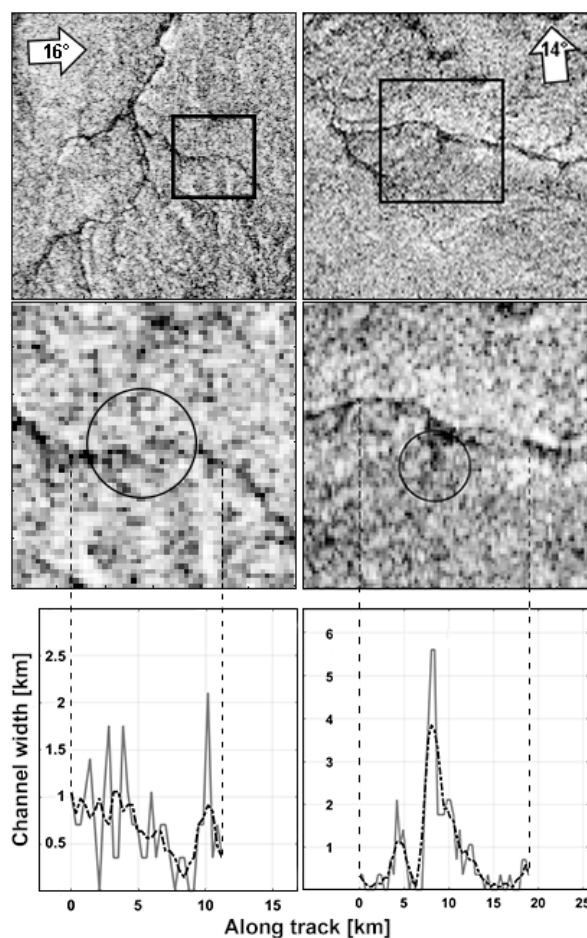

Figure 40: Width of channels for features "f" (left column) and "g" (right column). *Higher panels*. **Broad views of two mid-course areas of the Vid Flumina extracted from the T28 SAR image, the black squares show the regions pertaining to features "f" (left column) and "g" (right column). The white arrow indicates angle and look direction of the SAR image acquisition;** *Middle panels*. **Detail of the two sections of channels covered by the -3dB altimetric footprints (black circle) relative to the burstID 248037106 and 248037134. The two sections are respectively about 12 and 20 km long;** *Lower panels*. **The gray lines shown in this graphs indicate the width of the channel along its course as measured in each column of the upper SAR image. Each pixel is a square of side 0.351 km. It is worth noting that no despeckle algorithm has been applied on the radar image, this could results in somewhat larger fluctuations of the channel width around its actual values. For overcoming this problem we indicated with a black dashed line the moving average filtered measurements of the channels width.**

91

CHAPTER VII
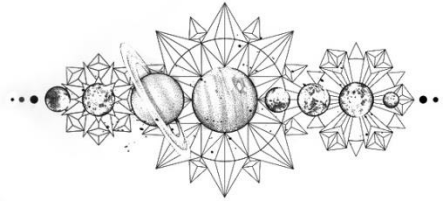
References

I. Alberti G., Catallo C., Festa L., Flamini E., Orosei R., Papa C., Picardi G., Seu R., Spataro F., Vingione G., "The Processing of Altimetric Data (PAD) System for Cassini RADAR", Memorie della Societa Astronomica Italiana, vol. 11, 2007. [Available at sait.oat.ts.astro.it/MSAIS/11/PDF/68.pdf.]

II. Alberti, G., L. Festa, C. Papa, and G. Vingione (2009), "A waveform model for near-nadir radar altimetry applied to the Cassini mission to Titan", Ieee Trans. Geosci. Rem. Sens., 47(7), 2252–2261, doi:10.1109/TGRS.2009.2012718.

III. Brown et al. (2008), "The identification of liquid ethane in Titan's Ontario Lacus", Nature, 454, 607-610.

IV. Bucciarelli, T., Cacopardi, S., Picardi, G., Seu, R., Levrini, G., Perfetti, R. , "Tracking Algorithms In Radar Altimetry", International Geoscience and Remote Sensing Symposium, 1988 (IGARSS'88), vol. 2, Florence, Italy, pp. 973-976, 12/09/1988;

V. Bucciarelli, T., Picardi, G., Seu, R., Levrini, G., Perfetti, R., "Spaceborne altimeter design for ocean and land missions", Alta Frequenza (English Edition) (ISSN 0002-6557), vol. 58, Mar.-Apr. 1989, p. 125-135.

VI. Burr, D. M., S. A. Drummond, R. Cartwright, B. A. Black, and J. Taylor Perron (2013), Morphology of fluvial networks on Titan: Evidence for structural control, Icarus, 226(1), 742–759.

VII. Cascioli G. and R. Seu (Jun. 1996), "Surface backscattering evaluation by means of the facet model for remote sensing applications," Acta Astronautica, vol. 40, no. 11, pp. 849–857.

VIII. Cheung H. and D. I.-J.Wang, "Solubility of volatile gases in hydrocarbon solvents at cryogenic temperatures," Ind. Eng. Chem. Fundam., vol. 3, no. 4, pp. 355–361, Nov. 1964, doi: 10.1021/i160012a014.

IX. Elachi, C., Allison, M.D., Borgarelli, L., Encrenaz, P., Im, E., Janssen, M.A., Johnson, W.T.K., Kirk, R.L., Lorenz, R.D., Lunine, J.I. and others, "RADAR: The Cassini Titan Radar Mapper," Space Sci. Rev. 115(1), 71–110 (2004).

X. Griffith, C., Lora, J., Turner, J., Penteado, P., Brown, R., Tomasko, M., Doose, L. and C. See (2012/06/14), "Possible tropical lakes on Titan from observations of dark terrain", Nature, 486, 237-239, 10.1038/nature11165L3.

XI. Grima, C., W. Kofman, A. Herique, R. Orosei, and R. Seu (2012), Quantitative analysis of Mars surface radar reflectivity at 20 MHz, Icarus, 220(1), 84–99, doi:10.1016/j.icarus.2012.04.017.

XII. Hagfors, T. (1964), Backscattering from undulating surface with application to Radar returns from the moon, J. Geophys. Res., 69, 3779–3784, doi:10.1029/JZ069i018p03779.

XIII. Hayes, A. G. (2016), The lakes and seas of Titan, Annu. Rev. Earth Space Sci., 44, 57–83.

XIV. Hayes, A. G., et al. (2008), Hydrocarbon lakes on Titan: Distribution and interaction with a porous regolith, Geophys. Res. Lett., 35, L09204, doi:10.1029/2008GL033409.

XV. Hayes, A. G., et al. (2010), Bathymetry and absorptivity of Titan's Ontario Lacus, J. Geophys. Res., 115, E09009, doi:10.1029/2009JE003557.

XVI. Hayes, A. G., et al. (2011), Transient surface liquid in Titan's polar regions from cassini, Icarus, 211(1), 655–671.

XVII. Hofgartner, J. D. et al., "Specular Reflections from Titan's Equatorial Region: Solving the Decade Old Mystery", American Geophysical Union, Fall Meeting 2014, abstract #P42B-06, 12/2014.

XVIII. Iess, L., N. J. Rappaport, R. A. Jacobson, P. Racioppa, D. J. Stevenson, P. Tortora, J. W. Armstrong, and S. W. Asmar (2010), Gravity field, shape, and moment of inertia of Titan, Science, 327(5971), 1367–1369, doi:10.1126/science.1182583.

XIX. Kirkby, M. J. (1980), The stream head as a significant geomorphic threshold, in Thresholds in Geomorphology, edited by D. R. Coates and J. D. Vited, pp. 53–73, Allen and Unvin, Winchester, Mass.

XX. Kwok R., Johnson W.T.K., (1989, Jul.). Block Adaptive Quantization of Magellan SAR Data. IEEE Trans. on Geoscience and Remote Sensing. [Online]. pp. 375-383. Available: http://ieeexplore.ieee.org/stamp/stamp.jsp?arnumber=29557

XXI. Le Gall, A., M. A. Janssen, L. C. Wye, J. Radebaugh, R. D. Lorenz, Cassini RADAR Team (2010), Regional variations among Titan's dunes: Belet versus Fensal dune fields. European Planetary Science Congress 2010 Vol. 1.

XXII.   Lorenz, R. D. (1993), The surface of Titan in the context of the Huygens Probe, ESA J., 17, 275–292.

XXIII.   Lorenz, R. D., and J. I. Lunine (1996), Erosion on Titan: Past and present, ICARUS, 122, 79–91.

XXIV.   Lorenz, R. D., et al. (2001), Cassini RADAR-Earth and Venus observations, J. Geophys. Res., 106(A12), 30,271–30, 280, doi:10.1029/ 2001JA900035.

XXV.   Lorenz, R. D., et al. (2008), Fluvial channels on Titan: Initial Cassini RADAR observations, Planet. Space Sci., 56(8), 1132–1144.

XXVI.   Lunine, J., and S. K. Atreya (2008), The methane cycle on Titan, Nat. Geosci., 1, 159–164, doi:10.1038/ngeo125.

XXVII.   Mastrogiuseppe, M., A. Hayes, V. Poggiali, R. Seu, J. I. Lunine, and J. D. Hofgartner (2016), Radar sounding using the Cassini altimeter: Waveform modeling and Monte Carlo approach for data inversion of observations of Titan's Seas, IEEE Trans. Geosci. Remote Sens, PP(99), 1–11, doi:10.1109/TGRS.2016.2563426.

XXVIII. Mastrogiuseppe, M., et al. (2014b), The bathymetry of a Titan sea, Geophys. Res. Lett., 41, 1432–1437, doi:10.1002/2013GL058618.

XXIX.   Mastrogiuseppe, M., V. Poggiali, R. Seu, R. Martufi, and C. Notarnicola (2014a), Titan dune heights retrieval by using Cassini radar altimeter, Icarus, 230, 336–354.

XXX.   Michaelides, R. J., A. G. Hayes, M. Mastrogiuseppe, H. A. Zebker, T. G. Farr, M. J. Malaska, V. Poggiali, and J. P. Mullen (2016), Constraining the physical properties of Titan's empty lake basins using nadir and off-nadir Cassini RADAR backscatter, Icarus, 270, 57–66, doi:10.1016/ j.icarus.2015.09.043.

XXXI.   Mitchell, K. L., Barmatz, M. B., Jamieson, C. S., Lorenz, R. D. and Lunine, J. I. (2015), Laboratory measurements of cryogenic liquid alkane microwave absorptivity and implications for the composition of Ligeia Mare, Titan. Geophys. Res. Lett., 42: 1340–1345. doi: 10.1002/2014GL059475.

XXXII.   Montefredini E., Morelli F., Picardi G., Seu R., "A non-coherent surface backscattering model for radar observation of planetary bodies and its application to Cassini radar altimeter", Planet.Space Sci., Vol.43, No.12, pp.1567-1577, 1995.

XXXIII. Ori, G. G., L. Marinangeli, A. Baliva, M. Bressan, and R. G. Strom (1998), Fluid dynamics of liquid on Titan's surface, Icarus, 46(9–10), 1417–1421, doi:10.1016/S0032-0633(97)00125-6.

XXXIV.   Picardi G. et al., "Marsis Data Inversion approach", IEEE 2007, DOI: 10.1109/AGPR.2007.386563.

XXXV.   Picardi G., "Radar for measuring interplanetary bodies", Sect. 14.5 of "Ground Penetrating Radar", 2nd Edition, edited by David .J. Daniels, 2004.

XXXVI.   Picardi, G., "Elaborazione del segnale radar. Metodologie ed applicazioni" (in italian), Franco Angeli, Nov. 2005.

XXXVII.   Picardi, G., Seu, R., Coradini, A. et al., "The radar system for the exploration of Titan", Nuovo Cimento C, Serie 1 (ISSN 0390-5551), vol. 15 C, no. 6, p. 1149-1161, 14 July 1992. doi:10.1007/BF02506709

XXXVIII. Poggiali V. et al., "Synergy of Cassini SAR and altimeter acquisitions for the retrieval of dune field characteristics on Titan", Proc. SPIE 8536, SAR Image Analysis, Modeling, and Techniques XII, 853608 (21 November 2012); doi: 10.1117/12.978185

XXXIX.   Ryan, W. B. F. (2009), Decoding the Mediterranean salinity crisis, Sedimentology, 56, 95–136.

XL.   Skolnik, M. (2008), Radar Handbook, 3rd ed., McGraw-Hill Education, Columbus, Ohio, isbn:9780071485470.

XLI.   Solonen, A., "Master's thesis: Monte Carlo Methods in Parameter Estimation of Nonlinear Models", Department of Information Technology, Laboratory of Applied Mathematics, Lappeenranta University Of Technology, 2006.

XLII.   Stiles, B., "Cassini Radar Basic image Data Records SIS", Ver. 2.0, JPL D-27889, April 22, 2008.

XLIII.   Stofan, E. R., et al. (2007), The lakes of Titan, Nature, 445, 61–64. [Available at http://www.nature.com/nature/journal/v445/n7123/abs/nature05438.html.]

XLIV.   Stofan, E.R., Wall, S.D., Stiles, B.W., Kirk, R.L., West, R.D., Callahan, P.S., "Cassini RADAR Users Guide", <http://pds-imaging.jpl.nasa.gov/documentation/Cassini_RADAR_Users_Guide.pdf >

XLV.   Strahler, A. N. (1957), Quantitative analysis of watershed geomorphology, Eos Trans. AGU, 38(6), 913–920, doi:10.1029/TR038i006p00913.

XLVI.   Summers Jason E., Soukup Raymond J., Gragg Robert F., "Characterization and Fabrication of Synthetic Rough Surfaces for Acoustical Scale-Model Experiments", 5 August 2005.

XLVII.   Ulaby, Moore, Fung, "Microwave remote sensing, vol. I", Artec House, 1982.

XLVIII.   Willgoose, G., R. L. Bras, and I. Rodriguez-Iturbe (1991), A physical explanation of an observed link area-slope relationship, Water Resour. Res., 27, 1697–1702, doi:10.1029/91WR00937.

XLIX.   Wingham, D. J., and C. G. Rapley (1987), "Saturation effects in the Seasat altimeter receiver", Int. J. Remote Sens., 8(8), 1163–1173, doi:10.1080/01431168708954762R.

L.   Wingham, DJ, CG Rapley e H Griffiths. "New techniques in satellite altimeter tracking systems". ESA Proceedings of the 1986 International Geoscience e Remote Sensing Symposium(IGARSS'86) on Remote Sensing: Today's Solutions for Tomorrow's Information Needs, 1986.

LI.   Wye, L. C., H. A. Zebker, and R. D. Lorenz (2009), Smoothness of Titan's Ontario Lacus: Constraints from Cassini RADAR specular reflection data, Geophys. Res. Lett., 36, L16201, doi:10.1029/2009GL039588.

LII.   Zebker, H. A., Y. Gim, P. Callahan, S. Hensley, R. Lorenz, and the Cassini RADAR Science Team, "Analysis and interpretation of Cassini Titan radar altimeter echoes", Icarus,Volume 200, Issue 1, Pages 240–255, March 2009, doi:10.1016/j.icarus.2008.10.023.

LIII.   Zebker, H., A. Hayes, M. Janssen, A. Le Gall, R. Lorenz, and L. Wye (2014), "Surface of Ligeia Mare, Titan, from Cassini altimeter and radiometer analysis", Geophys. Res. Lett., 41, 308–313, doi:10.1002/2013GL058877.

Special

thanks

to

my wife

for her support and loving me unconditionally,

my parents

for always believing in me and always encouraging me,

Marco Mastrogiuseppe, Ph.D., and Roberto Seu, Ph.D.

whose vision help me in understanding a bit more about radars,

Prof. Giovanni Picardi

who will always be with us,

All the Cassini RADAR science team

that promptly rescheduled Cassini radar science observations plans in order to better exploit the altimeter capabilities and do not miss the opportunity of dong some good science.

Roma,

October 27, 2016.